Aramco

Journal of Technology

FALL 2021

Aramco
Journal
of Technology

The *Aramco Journal of Technology* is published quarterly by the Saudi Arabian Oil Company, Dhahran, Saudi Arabia, to provide the company's scientific and engineering communities a forum for the exchange of ideas through the presentation of technical information aimed at advancing knowledge in the hydrocarbon industry.

The *Aramco Journal of Technology* gratefully acknowledges the assistance, contribution and cooperation of numerous operating organizations throughout the company.

ISSN 1319-2388

Contents

The Effect of High Power Laser on Organic-Rich Shales

Dr. Damian P. San-Roman-Alerigi, Dr. Sameeh I. Batarseh and Wisam J. Assiri

Abstract /

The objective of this work is to characterize the effect of a high power laser (HPL) on organic-rich shales (ORS). The analysis combines machine learning with advanced characterizations to reveal the geochemical and mechanical transformations induced by a HPL in source rocks. Lab results showed that HPL improves permeability, increases porosity, modifies the mechanical structure of the rock, and may positively affect the maturity of source rocks.

A HPL was used in the lab to perforate and heat different types of source rocks with varying organic content. The process was characterized in real time using near infrared (IR) spectroscopy and mid-IR thermography. The pre- and post-characterization process draws on different tools to evaluate the chemical and structural transformations induced by the HPL processes. This step included several spectroscopy techniques, e.g., Fourier transform IR (FTIR) spectroscopy and UV/VIS/near IR, rock-eval pyrolysis, and differential thermal analysis (DTA). The analysis leverages on clustering techniques to reveal the distinct effects of HPL on source rocks.

The spectroscopy and geochemical analyses revealed that that the HPL modifies the molecular structure of the rock. Yet, the fundamental structure of the rock remains intact. The changes are revealed by clustering analysis of the FTIR data before and after laser heating. The analysis show the formation of clusters after the process, which correspond to the maturation of the organic content.

The success of the lab work proved that the HPL could enhance the properties of source rocks. The effects include permeability improvement, enhanced porosity, and changes in the molecular distribution of the organic content. The results of the analyses suggest that the laser can drive forward the maturity of the source rock. This work also illustrates how machine learning and multiphysics characterization can reveal the dynamics of the HPL processes and their effects. Ultimately, the outcome of this study will contribute to the development of novel HPL applications.

Introduction

Organic-rich shales (ORS) are sedimentary rocks with low permeability, abundant kerogen, and occasionally contain bitumen and oil. This organic content may vary between 5 wt% to 65 wt%, distributed among reduced carbon, hydrogen, oxygen, nitrogen, and sulfur[1]. Under high-pressure, high temperature, the kerogen pyrolyzes into hydrocarbons and traces of residual carbon. The pyrolysis can also be accelerated artificially by heating the kerogen to around 400 °C[2].

Electromagnetic (EM) heating is of interest in subsurface applications because it is waterless, compact, controllable, and efficient[3]. These methods rely on radiative, conductive, and dielectric heating to warm up the rocks. The efficiency varies between 1.2 to two times the total energy input. Of great interest has been dielectric methods since microfrequency and radio frequency radiation can penetrate deeper into diverse rock formations[4, 5].

The electromagnetically driven pyrolytic process is environmentally friendly; yet, the overall method may produce significant amounts of greenhouse gases depending on the nature of the energy source employed to power the EM heaters, and the type of heaters employed. For example, conductive radiative heating using Joule heaters may require up to 2 years of continuous operation, whereas microwave heating can attain similar results in half the time[1, 5].

Several studies have demonstrated that dielectric heating using microfrequency and radio frequency waves could improve efficiency and lessen the environmental impact. Yu et al. (2020)[6] examined the organic matter evolution as a function of temperature in oil shale retorting. Below 300 °C, the main products are water and gas, and the organic matter maturity ranges from immature to low mature. Between 300 °C and 475 °C, the process generates mainly oil and gas, with an optimal oil generation window spanning 400 °C to 440 °C. The rock's maturity evolved to the mature stage with high hydrocarbon generation potential in this temperature range. Above 475 °C and up to 520 °C, the rock yields a low amount of gas, and the rock's maturity advances to high mature or overmature.

A higher temperature will result in mineral dissociation and spallation[7]. Fianu and Hassan (2020)[8] developed a model to guide gas shale retorting using microwave heating; they found the process could improve cumulative production by 25% through adsorbed gas release. Zhu et al. (2021)[9] created a comprehensive model to study the retorting of oil shale through different microwave heating schemes at atmospheric pressure. The results evinced that stepwise heating improves production and reduces energy consumption.

The process also modifies the rock's structure. Kobchenko et al. (2011)[10] captured a 3D computed tomography (CT) scan time-lapse of ORS retorting between 60 °C and 400 °C. The analysis revealed that cracks initiated in regions with a higher amount of organic matter at or above 350 °C. The kerogen decomposition into hydrocarbons increases the volume of fluids in the rock, which raises the internal pressure, and eventually leads to fracturing. The observations suggested that low permeability pathways formed earlier than macroscopic fractures. The results were later confirmed by various experiments and the numerical models previously cited. Pervukhina et al. (2015)[11] observed fast-growing microfracture and macrofracture networks in carboniferous ORS during retorting.

Egboga et al. (2017)[12] found that the decomposition of kerogen to hydrocarbons leads to a twofold increase in permeability. Zhu et al. (2018)[13] noted that microwave heating induces the formation of micropores and fractures, and the process changed the shape of the pores to mesopores with a small diameter. In a subsequent study, they corroborated that the structural changes depend on radiation power and exposure time. As the rock heats up, the thermal energy can be sufficient to dissociate minerals and cause various changes to the rock's structure. They observed that the pore size and distribution tended to homogenize in samples exposed to a higher radiation power[14].

Gabova et al. (2020)[15] studied the thermal expansion of ORS between 25 °C and 300 °C. The experiment revealed the thermal expansion in these rocks is nonlinear, non-monotonous, and anisotropic. Thermal expansion was larger in the direction that connected most of the organic matter, thereby revealing anisotropies in the process. The expansion was also non-monotonous due to exudation of bitumen and the ejection of volatiles. These changes modified the mechanical, EM, and thermal properties of the rock permanently.

The various physical and chemical changes observed during retorting modify the coupling between the EM wave and the rock. The interaction can be further complicated by the presence of water, brine, and other fluids or solids, porosity, environmental humidity, pressure, and temperature[16, 17]. The net effect is that efficiency EM coupling will vary during the process. Organic compounds have low EM absorption in the microfrequency and radio frequency range[18], which poses a challenge to heat formations with low water or clay content. A possible solution is to inject nanoparticles or active fluids that absorb the EM energy and convert it to heat within the rock[19].

An alternative to dielectric heating with microwaves or radio waves is to use EM radiation in the infrared (IR) and visible range of the spectrum. ORS and most formation rocks exhibit large absorption in the IR range, thereby enabling IR high power lasers (HPL) to heat targets well above the sublimation temperature[20]. At this wavelength, the penetration depth is smaller ($< 10^{-2}$ cm); however, the HPL beam can be controlled to create on-demand perforations, fractures, or heat the rocks. This work summarizes key results of the HPL heating of the ORS.

Experimental Setup

A HPL (IPG Photonics YLS 10000, λ = 1,064 nm + 10 nm, $P_{out} \leq 10$ kW) illuminated ORS rocks for different time durations. High-speed thermograms were acquired from three faces of the sample using a high-speed middle wavelength IR thermographic camera (FLIR X6900sc, τ = 1 ms). Near IR reflectance spectra was recorded from the face exposed to the HPL beam using a high-speed near IR spectrometer (Ocean Optics NIRQUEST2500, 900 nm $\leq \lambda \leq$ 2,500 nm, τ = 1 ms). The HPL power and exposure time were controlled to keep the samples' temperature below 500 °C during the experiment. The heating rate of a sample exposed to the HPL depends on the power density of the laser, (P_d), and the target's properties.

The samples included over 500 ORS carboniferous rocks with low clay content (< 5 wt%). The samples are from an undetermined origin.

Pre- and post-exposure characterization included differential thermal analysis (DTA), (Netzsch STA 449 F5 Jupiter, $T \leq$ 2,000 °C), IR diffusive reflectance (PerkinElmer Lambda 1050+ UV/VIS/NIR, 900 nm $\leq \lambda \leq$ 2,500 nm, τ = 1 ms), mid-IR Fourier transform diffusive reflectance (Bruker Alpha II, 400 cm$^{-1} \leq \lambda \leq$ 4,500 cm^{-1}), and rock-eval pyrolysis. Table 1 describes the use of each device.

Results and Discussion

Figure 1 displays the total reflectance of a random subset of the ORS samples used in the experiment.

The spectra shows how the ORS absorb near IR radiation. Lower reflectance implies the rocks absorbs more EM energy. The absorbed near IR radiation convers to thermal energy and warms up the rock. There are two regimes of absorption during HPL rock interaction[20]:

1. Linear: The energy coupling is a function only of the EM frequency.

2. Nonlinear: The energy coupling is a function of the EM power and frequency.

The second regime can lead to a phenomenon known as absorption saturation. The absorption dynamics of materials depend on its physical and chemical properties; e.g., porosity, organic content, fluid saturation, roughness, mineral distribution, ionization, among others to reshape the EM absorption. Therefore, similar

Table 1 *A summary of the characterization devices and their uses.*

Device	Description
Thermal analyzer (TGA/DTA/DSC)	A thermal-gravimetric analyzer (TGA) is an analytical technique used to determine the weight change as a function of temperature. This technique provides information about the physical and chemical changes of the sample as a function of temperature change.
	Differential thermal analysis (DTA) and differential scanning calorimeters (DSC) are thermoanalytical techniques that compare an inert reference against the test sample. The study provides information about the transformations that occur as the heat flows into a sample.
UV/VIS/NIR reflectance spectroscopy	Reflectance spectrometry is a technique that measures the diffusive and specular reflectance of light as a function of wavelength. The device uses an integrating sphere to collect light diffusively scattered. The spectra is acquired by illuminating the samples with light of narrow spectral width (~0.1 to 0.5 nm), ranging from UV (250 nm) to near IR (2,500 nm). The measurement provides information about the absorption of the sample and its surface chemical composition.
FTIR reflectance spectroscopy	This device captures a set of interferograms resulting from the simultaneous illumination of a sample with light covering overlapping wide spectral range. A Fourier transform converts the interferogram into a spectrum. The technique provides higher resolution, quality, and accuracy over dispersive spectroscopy. The spectra provides information about the molecular arrangement of the sample.
Rock-eval pyrolysis	A technique that uses a flame ionization detector to sense the organic compounds generated during pyrolysis. It provides information about the quantity organic matter present in a sample. The output is a pyrogram with peaks labeled $Sn(T_n)1$, n = 1,2,3 and $T_n < T_{n+1}$. S1 represents the amount of carbon compounds thermally distilled from one gram of rock. S2 is the amount of carbon compounds pyrolyzed from the kerogen content in one gram of rock. S3 is the amount of carbon dioxide generated during the measurement[21].

Fig. 1 *The total reflectance of a random subset of the ORS samples used in the experiment[20].*

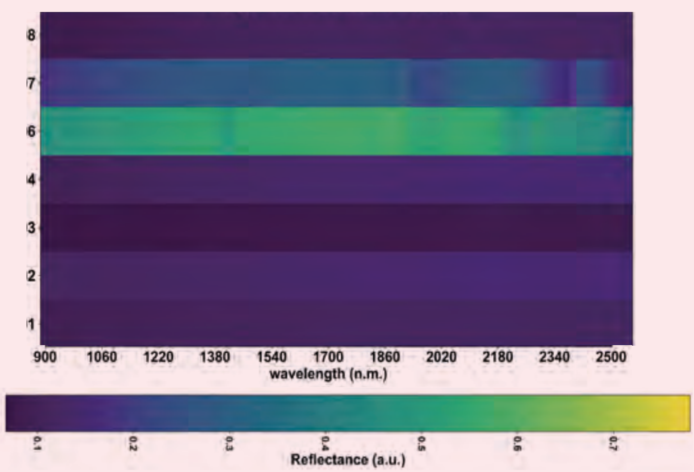

rock types may exhibit different absorption profiles.

For example, Fig. 2 depicts the Kubelka-Munk spectra and the total organic content (TOC) measured for 15 shale samples before HPL exposure. A qualitative view of the graphs suggests that the TOC and reflectance spectra could be correlated. This concept has been employed to fingerprint kerogen and determine thermal maturity on ORS using Fourier transform spectroscopy[22].

Effect of Laser Heating

Figure 3 depicts the experimental arrangement. A reference sample (S1) is taken from each rock before the exposure. The test sample is exposed to a HPL beam for up to five minutes at $P_d \approx 600$ W/cm^2. The laser beam can be turn on continuously, or pulsed with a repetition rate between 10 Hz to 1 kHz. A pulsed operation can be employed to control heating and cooling rates, as well as to maintain a constant temperature.

A rock-eval pyrolysis was conducted in 20 representative samples. Figure 4 plots the *Tmax* and normalized TOC for an ORS at each measurement region. The higher *Tmax* and lower TOC indicates area S2 has been fully matured, with mostly remaining carbons are present in the regions. The other regions exhibit no apparent change.

Figure 5 plots the normalized parameters determined by rock-eval pyrolysis before (S1) and after HPL heating (S2 to S4).

The results demonstrate that the sample has matured at different rates. The face exposed to the laser has fully matured. In this region, most volatiles and bitumen have been expelled, while kerogen has been fully matured and converted into hydrocarbons. The remaining regions show a higher content of volatiles, bitumen, and kerogen. These areas have also matured; yet, their potential remains high. The largest amount of carbon dioxide is evolved by the outer region not exposed to the laser. This could be explained by either migration of the hydrocarbons or molecular changes in the fabric of the rock.

Fig. 2 *The Kubelka-Munk spectra and TOC measured for 15 various shale samples.*

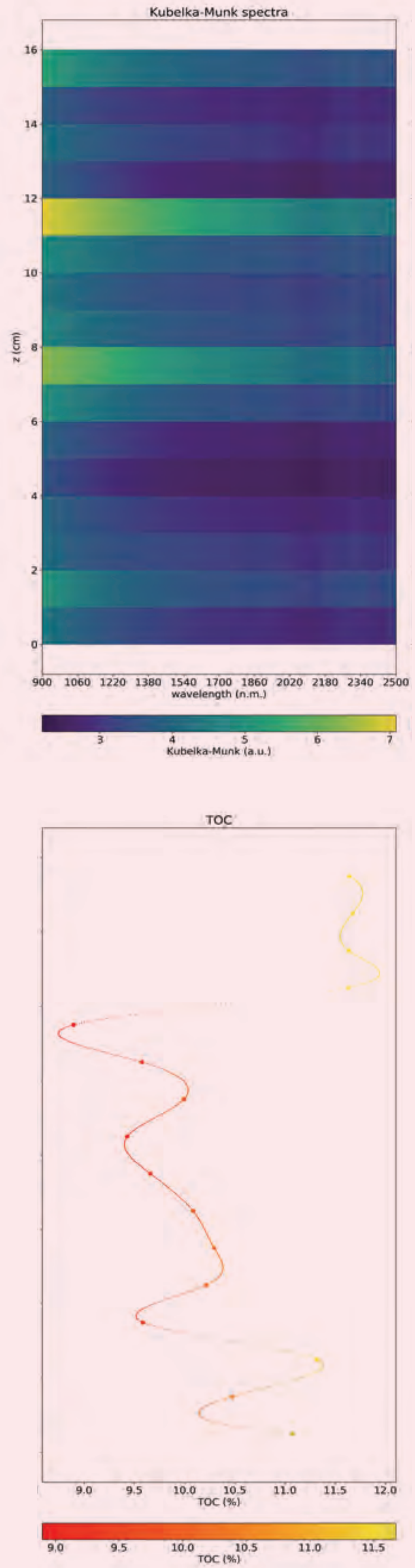

Fig. 3 *Experimental arrangement samples in relation to the HPL beam. The labels denote the sampling regions for rock-eval pyrolysis. S1 is the reference sample, S2 is the area illuminated by the HPL, S3 is at the center of the sample, and S4 is opposite to S2.*

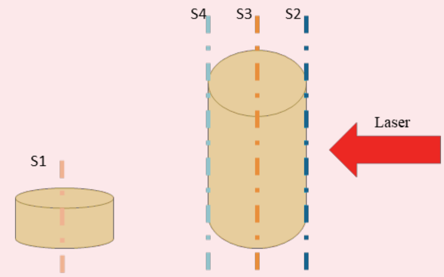

Fig. 4 *The relative* Tmax *and TOC before and after HPL exposure*[23].

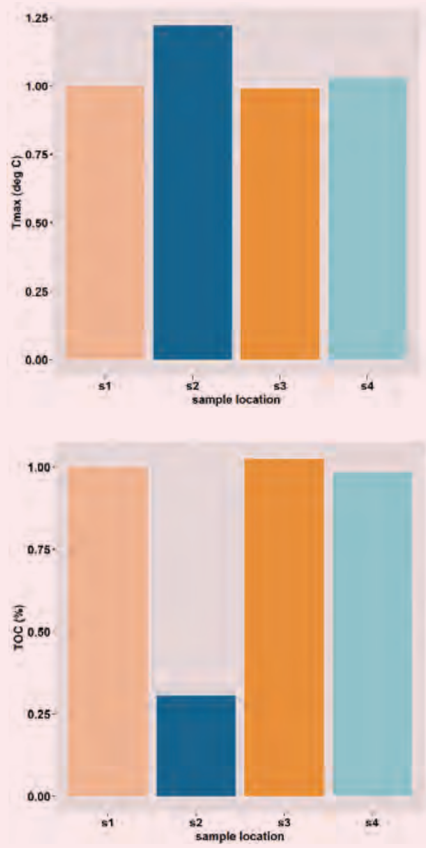

Fourier transform IR (FTIR) reflectance spectra was measured in all samples before and after the HPL exposure. The spectra encompasses 1,752 features corresponding to the reflectance at narrow wavelength ranges. Therefore, KMeans and t-distributed stochastic neighbor embedded (tSNE) clustering techniques were used to study the molecular changes in the rocks.

The qualitative analysis of the data indicated there are 10 potential clusters for the peaks observed in the FTIR

Fig. 5 *The parameters S1 (top), S2 (center), and S3 (bottom) before and after HPL heating*[23].

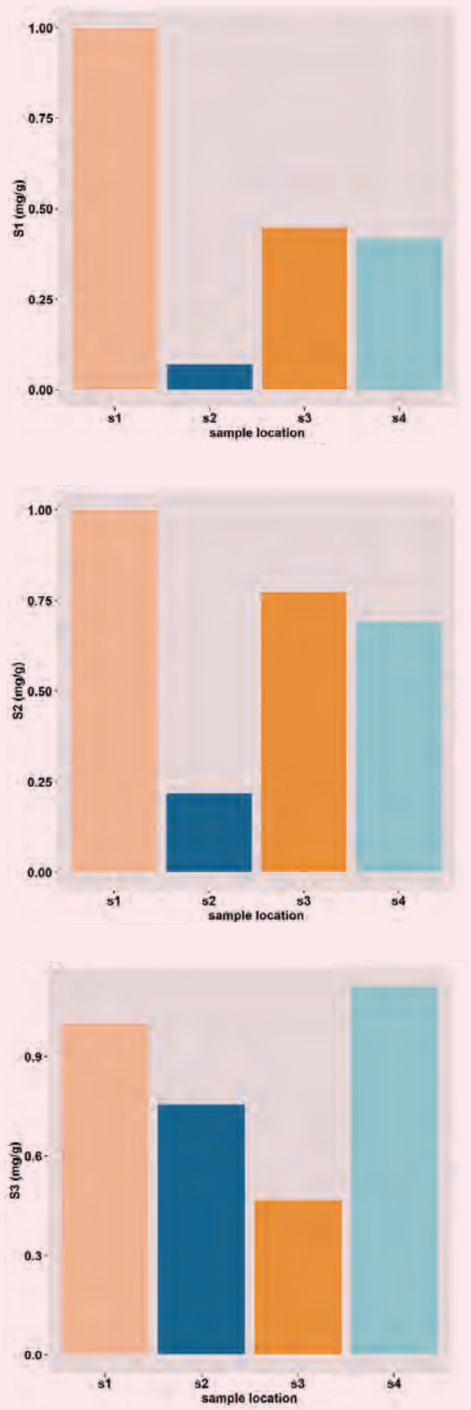

Fig. 6 *The point plot of KMeans groups population before and after HPL exposure. The data included 10 distinct clusters given by the location of peaks in the FTIR spectra.*

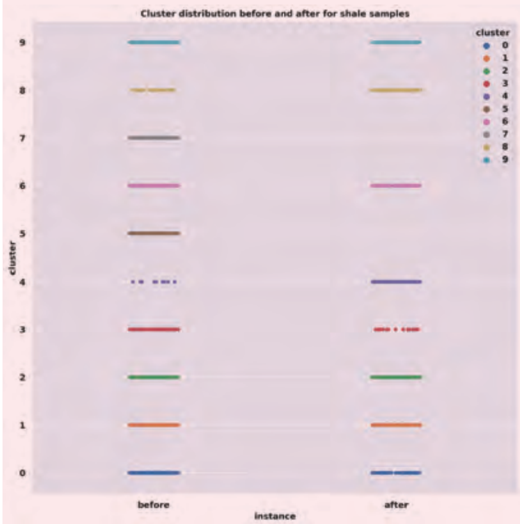

spectra. Figure 6 plots the population for each group before and after HPL exposure. The plot shows that after exposure some groups vanished, which indicates a change in the molecular arrangement of the samples after laser exposure. This change could be explained by the maturation of the kerogen in the rocks or the release of volatiles and bitumen. The effects of mineral dissociation or spallation are not considered because these occur at higher temperature for carboniferous ORS ($T \geq 700$ °C)[23].

Figure 7 plots the tSNE 2D plot for the spectral data; each point is colored with its corresponding KMeans group (refer to Fig. 6). The graphs demonstrate that there is a molecular change in the rock constituents after HPL exposure, which is evidenced by the "migration" of points to clusters 4 and 7. The presence of some groups before and after exposure reveals that the fundamental structure of the rock remains intact. This is expected, as the laser-driven pyrolysis remains at a temperature below calcination and spallation. These results combined with observations from the rock-eval pyrolysis demonstrate that HPL can be used to change the organic content of the rock.

Conclusions

A HPL presents unique advantages for subsurface applications. Numerous lab experiments have demonstrated it enhances permeability and porosity. The HPL can also modify the molecular structure of the rocks by dehydrating clays, dissociating minerals, or breaking cementations. This work demonstrates the use of HPLs for retorting of the ORS.

Clustering analysis of spectral data demonstrated that a HPL could change the molecular distribution of the organic content in the rock. The results suggest that the laser can drive forward the maturity of the ORS. This work also illustrates how advanced clustering techniques combined with multiphysics characterization can assist in the analysis of HPL processes and their

Fig. 7 *The tSNE distribution before (left) and after (right) HPL exposure. The points take the color of their corresponding KMeans group, which was derived using the raw data.*

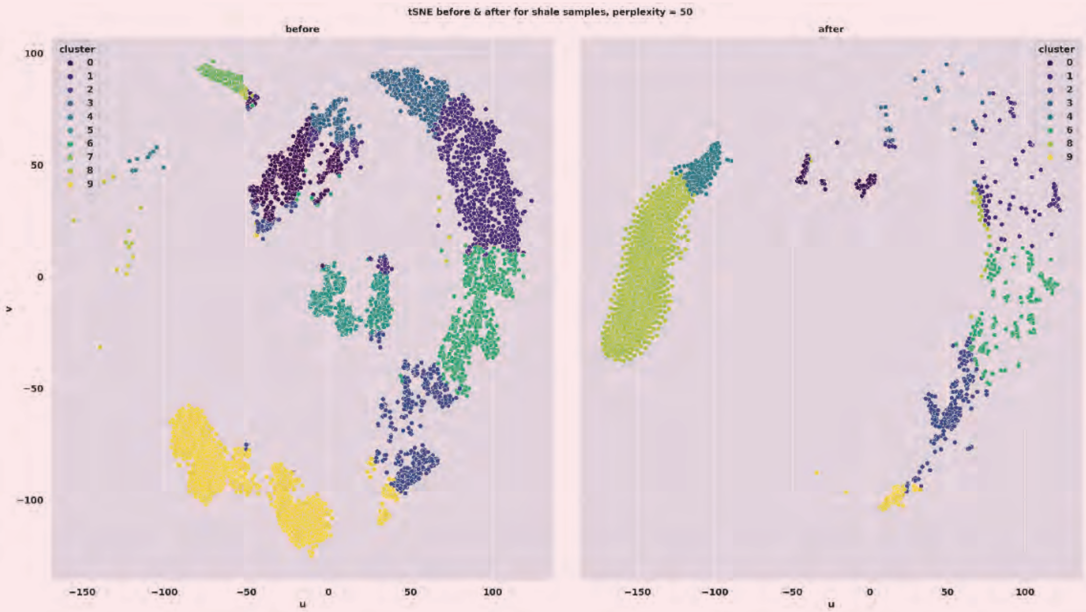

effects. Ultimately, the outcome of this study contributes to the development of future HPL applications.

Acknowledgments

This article was prepared for presentation at the 2021 SPE Middle East Oil & Gas Show, Manama, Kingdom of Bahrain, November 28 – December 1, 2021.

References

1. Brandt, A.R.: "Converting Oil Shale to Liquid Fuels: Energy Inputs and Greenhouse Gas Emissions of the Shell in Situ Conversion Process," *Environmental Science and Technology*, Vol. 42, Issue 19, August 2008, pp. 7489-7495.

2. Kang, Z., Zhao, Y. and Yang, D.: "Review of Oil Shale in Situ Conversion Technology," *Applied Energy*, Vol. 269, July 2020.

3. Bera, A. and Babadagli, T.: "Status of Electromagnetic Heating for Enhanced Heavy Oil/Bitumen Recovery and Future Prospects: A Review," *Applied Energy*, Vol. 151, August 2105, pp. 206-226.

4. Hascakir, B., Babadagli, T. and Akin, S.: "Experimental and Numerical Simulation of Oil Recovery from Oil Shales by Electrical Heating," *Energy & Fuels*, Vol. 22, Issue 6, September 2008, pp. 3976-3985.

5. Song, X., Zhang, C., Shi, Y. and Li, G.: "Production Performance of Oil Shale in Situ Conversion with Multilateral Wells," *Energy*, Vol. 189, December 2019.

6. Yu, F., Sun, P., Zhao, K., Ma, L. et al.: "Experimental Constraints on the Evolution of Organic Matter in Oil Shales during Heating: Implications for Enhanced in Situ Oil Recovery from Oil Shales," *Fuel*, Vol. 261, February 2020.

7. Gahan, B.C., Parker, R.A., Graves, R., Batarseh, S.I., et al.: "Laser Drilling: Drilling with the Power of Light Phase 1: Feasibility Study," U.S. Department of Energy Report, OSTI, September 2001, 107 p.

8. Fianu, J., Gholinezhad, J. and Hassan, M.: "Thermal Simulation of Shale Gas Recovery Involving the Use of Microwave Heating," *Journal of Petroleum Science and Engineering*, Vol. 186, March 2020.

9. Zhu, J., Yi, L., Yang, Z. and Li, X.: "Numerical Simulation on the in Situ Upgrading of Oil Shale Reservoir under Microwave Heating," *Fuel*, Vol. 287, March 2021.

10. Kobchenko, M., Panahi, H., Renard, F., Dysthe, D.K., et al.: "4D Imaging of Fracturing in Organic-Rich Shales during Heating," *Journal of Geophysical Research: Solid Earth*, Vol. 116, Issue B12, December 2011.

11. Pervukhina, M., Uvarova, Y., Yurikov, A., Patrusheva, N., et al.: "Changes in Microstructure and Mineralogy of Organic-Rich Shales Caused by Heating," *ASEG Extended Abstracts*, Vol. 2015, Issue 1, pp. 1-4.

12. Egboga, N.U., Mohanty, K.K. and Balhoff, M.T.: "A Feasibility Study of Thermal Stimulation in Unconventional Shale Reservoirs," *Journal of Petroleum Science and Engineering*, Vol. 154, June 2017, pp. 576-588.

13. Zhu, J., Yang, Z., Li, X., Wang, N., et al.: "Evaluation of Different Microwave Heating Parameters on the Pore Structure of Oil Shale Samples," *Energy Science & Engineering*, Vol. 6, Issue 6, December 2018, pp. 797-809.

14. Zhu, J., Yang, Z., Li, X., Qi, S., et al.: "The Experimental Study of Microwave Heating on the Microstructure of Oil Shale Samples." *Energy Science & Engineering*, Vol. 7, Issue 3, June 2019, pp. 809-820.

15. Gabova, A., Chekhonin, E., Popov, Y., Savelev, E., et al.: "Experimental Investigation of Thermal Expansion of Organic-Rich Shales," *International Journal of Rock Mechanics and Mining Sciences*, Vol. 132, August 2020.

16. Hakala, J.A., Stanchina, W., Soong, Y. and Hedges, S.:

"Influence of Frequency, Grade, Moisture and Temperature on Green River Oil Shale Dielectric Properties and Electromagnetic Heating Processes," *Fuel Processing Technology*, Vol. 92, Issue 1, January 2011, pp. 1-12.

17. Han, T., Beloborodov, R., Pervukhina, M., Josh, M., et al.: "Theoretical Modeling of Dielectric Properties of Artificial Shales," *Geofluids*, Vol. 2018, Issue 108, January 2018, pp. 1-12.

18. Alvarez, J.O. and Penaranda-Foix, F.: "Multi-Frequency Microwave Resonance Cavity for Nondestructive Core Plug Measurements," paper presented at the IEEE International Geoscience and Remote Sensing Symposium, Valencia, Spain, July 22-27, 2018.

19. Batarseh, S.I., Othman, H.A., San-Roman-Alerigi, D. and Kumaoka, S.: "Microwave with Assisted Ceramic Materials to Maximize Heat Penetration and Improve Recovery Efficiency of Heavy Oil Reservoirs," SPE paper 183773, presented at the SPE Middle East Oil and Gas Show and Conference, Manama, Kingdom of Bahrain, March 6-9, 2017.

20. Batarseh, S.I., San-Roman-Alerigi, D., Al Obaid, O. and Othman. H.A.: "Laser Gun: The Next Perforation Technology," SPE paper 194775, presented at the SPE Middle East Oil and Gas Show and Conference, Manama, Kingdom of Bahrain, March 18-21, 2019.

21. Peters, K.E.: "Guidelines for Evaluating Petroleum Source Rock Using Programmed Pyrolysis," *AAPG Bulletin*, Vol. 70, Issue 3, March 1986, pp. 318-329.

22. Chen, Y., Zou, C., Mastalerz, M., Hu, S., et al.: "Applications of Micro-Fourier Transform Infrared Spectroscopy (FTIR) in the Geological Science — A Review," *International Journal of Molecular Sciences*, Vol. 16, Issue 12, December 2015, pp. 30223-30250.

23. Othman, H.A., San-Roman-Alerigi, D., Batarseh, S.I. and Al Obaid, O.: "Efficiency of High Power Laser in Carbonate Formations," SPE paper 197480, presented at the Abu Dhabi International Petroleum Exhibition and Conference, Abu Dhabi, UAE, November 11-14, 2019.

About the Authors

Dr. Damian P. San-Roman-Alerigi

Ph.D. in Electrical Engineering, King Abdullah University of Science and Technology

Dr. Damian P. San-Roman-Alerigi is a Petroleum Scientist working with the Production Technology Team of Saudi Aramco's Exploration and Petroleum Engineering Center – Advanced Research Center (EXPEC ARC). His focus is on developing the next generation of subsurface photonic and electromagnetic tools.

Damian's previous research focused on the interaction of waves with complex media and its application to subsurface technologies. His work encompasses different areas of science and engineering, from oil and gas to applied mathematics. He has published papers in various international journals and conferences around the world.

Damian received his B.S. degree in Physics from the National Autonomous University of Mexico, Mexico City, Mexico. In 2008, he enrolled in King Abdullah University of Science and Technology (KAUST) as a founding class student where he completed his M.S. degree in 2010, and his Ph.D. degree in 2014, both in Electrical Engineering.

Dr. Sameeh I. Batarseh

Ph.D. in Petroleum Engineering, Colorado School of Mines

Dr. Sameeh I. Batarseh is a Petroleum Engineering Consultant working with the Production Technology Team of Saudi Aramco's Exploration and Petroleum Engineering Center – Advanced Research Center (EXPEC ARC). Currently, he is the Focus Area Champion of the Unconventional Resources leading the High-Power Laser Program. Sameeh's area of interest is to develop an in situ laser application in drilling, perforation and fracturing, among many other applications with a focus on unconventional reservoirs.

He is an active member of the Society of Petroleum Engineers (SPE), serving the society for several years while holding different positions, including sitting on the SPE Executive Advisory Committee, chairing the Program Committee and serving as session chairman. He was also the board and vice chair for the Western Region USA San Joaquin Valley. Sameeh's service is recognized worldwide as he received the SPE President Section Award of Excellence, Regional Service Award, and is a SPE Distinguished Lecturer. He has organized over 54 SPE technical workshops.

Sameeh has authored or coauthored more than 74 articles with high-impact publications, and has an H-Index of 36. He holds 48 patents (16 granted patents and has 32 patents in progress).

Sameeh received his Ph.D. degree in Petroleum Engineering from the Colorado School of Mines, Golden, CO.

Wisam J. Assiri

B.S. in Chemical Engineering, King Fahd University of Petroleum and Minerals

Wisam J. Assiri is a Petroleum Engineer working with the Production Technology Team of Saudi Aramco's Exploration and Petroleum Engineering Center – Advanced Research Center (EXPEC ARC). He is working on researching new technologies in stimulation gas wells and productivity enhancement.

Wisam is currently on assignment with the Southern Area Production Engineering Department/Haradh & Harmaliyah Production Engineering Unit.

In 2006, he received his B.S. degree in Chemical Engineering from King Fahd University of Petroleum and Minerals (KFUPM), Dhahran, Saudi Arabia.

A Nano Method for a Big Challenge: Nanosilica-Based Sealing System for Water Shutoff

Dr. Ayman M. Al-Moshin, Dr. Jin Huang, Mohammed I. Alabdrabalnabi and Mohamed H. Sherief

Abstract /

Minimizing unwanted water production from oil wells is a significant requirement in the petroleum industry. This would lead to improved economic life of mature wells that involve new and innovative technologies. Nanosilica-based sealing fluid has been developed to address problems associated with unwanted water production. The objective of this work is to evaluate a newly developed novel water shutoff system based on nanosilica over a wide range of parameters.

This modified nanosilica has a smooth, spherical shape, and are present in a narrow particle size distribution. Therefore, it can be used for water management in different water production mechanisms, including high permeability streak, wormhole, and fractured reservoirs. A systematic evaluation of novel nanosilica/activator for water shutoff purposes requires the examination of the chemical properties before, during, and after gelation at given reservoir conditions. These properties are initial solution viscosity, gelation time, injectivity, and strength of the formed gel against applied external forces in different flooding systems.

This article details a promising method to control undesired water production using eco-friendly, cost-effective nanosilica. Experimental results revealed that nanosilica initially exhibited a low viscosity, and therefore, provided a significant advantage in terms of mixing and pumping requirements. Nanosilica gelation time, which is a critical factor in placement of injected chemical treatment, can be tailored by adjusting the activator concentration to match field requirements at the desired temperature. In addition, coreflood tests were conducted in carbonate core plugs, Berea sandstone rock, and an artificially fractured (metal tube) to investigate the performance of the chemical treatment.

Flow tests clearly indicated that the water production significantly dropped in all tested types of rocks. The environmental scanning electron microscope (SEM) results showed the presence of silicon dioxide (SiO)-rich compounds suggesting that the tested nanosilica product filled the porous media, therefore, it blocked the whole core plug.

A novel cost-effective sealant that uses nanotechnology to block the near wellbore region has been developed. The performance and methods controlling its propagation rate into a porous medium will be presented. Based on the outcomes, it must be emphasized that these trivial particles have a promising application in the oil reservoir for water shutoff purposes.

Introduction

Controlling undesired water production from oil and gas wells is one of the main goals in the petroleum industry. It should deserve high attention as it could minimize the total reserves' recovery across the globe. For instance, it causes liquid loading, sand production, fines migration, scale formation, and tubular corrosion. Additionally, the natural drive mechanism to produce oil is no longer sufficient, due to the massive water production that prematurely depletes the reservoir and eventually results in well abandonment[1, 2].

Nanotechnology has been utilized extensively in the upstream sector. Since the properties of nanomaterials are eminent, this unleashes the potential to explore and develop several sedimentary basins[3-5]. Based on earlier research, nanomaterials prevailed in plugging pore throats by drastically minimizing the shale permeability. Furthermore, researchers have emphasized on the physical properties of silica nanoparticles that have morphological characteristics and a high surface area enabling superb plugging of pore throats[5-9].

Nanosilica nanoparticles have received extensive attention recently, based on minimum cost and distinctive physical properties such as having a simple surface to be modified and a large surface area[10-12]. Nanosilica has a significant impact in enhancing the oil recovery. To illustrate, according to the work reported by Aqcheli et al. (2020)[12], we can optimize conventional waterflooding and highly improve oil recovery by injecting performed particle gel solutions that contains nanosilica gel. Also from the works of Mo et al. (2012)[13], Yu et al. (2012)[14], and San et al. (2017)[15], nanosilica stabilizes the generation of carbon dioxide foam for enhanced oil recovery (EOR).

Almohsin et al. (2018)[16] showed promising results using silicon dioxide (SiO) nanoparticles along with aluminum dioxide nanoparticles on emulsion stability utilized in EOR applications. Another major application of nanosilica is to improve the gas production of gas wells suffering from condensate banking in retrograde gas condensate reservoirs. For instance, a modified nanosilica by flurosurfactant is utilized to alter the wettability of the rock from liquid-wetting to gas-wetting[17]. As for water-based drilling fluids, nanosilica plays a major role in stabilizing such fluids at high temperatures, enhancing their rheological properties and increasing viscosity[18-20].

To mitigate water production from oil and gas wells, we have an extensive range of approaches for reservoir conformance control. As for chemical approaches, we normally utilize cement and gel squeezes. Consequently, the most commonly used chemicals are gellant materials such as sodium silicate gels. After placing these gellants deeply into the reservoir pores, they construct a 3D gel system. Moreover, for a selective placement and blockage of water, we use relative permeability modifiers and selective permeability blockers. Although there are numerous types of chemicals utilized for reservoir conformance control, several chemicals are not preferred due to environmental regulations[21].

Furthermore, Shamlooh et al. (2020)[22] studied and confirmed the effect of nanosilica at 130 °C on physically reinforcing two water shutoff systems — polyacrylamide tert-butyle acrylate (PAtBA)-chromium acetate ($CrAc_3$) and PAtBA-polyethyleneimine (PEI). In addition, nanosilica particles enhance the gel strength and thermal stability of the dispersed particle gels[23]. According to the experimental work of Shamlooh et al. (2019)[24], the developed system is utilizing reinforcement of polyacrylamide and PEI gels using nanosilica. This fluid system experienced high gel strength that makes it a potential to block fractured reservoirs. A nanosilica-based fluid system has revealed encouraging outcomes, such as optimum and controllable gelation time, low initial viscosity, and thereby deep penetration into the reservoir[1, 25, 26].

This article presents a novel water shutoff based on nanotechnology. This work provides new results on controlling the setting time under a variety of reservoir conditions. The effect of temperature and activator concentrations are investigated. Two sets of core flow tests are implemented using a core plug and fracture model. Microscopy and the scanning electron microscope (SEM) provide solid evidence that this technology can easily penetrate through porous media. The fracture model proved that the proposed technology can completely seal the fracture with excellent performance. The scope of this effort is to determine different operating conditions to deploy the new system in the field.

Materials

Aqueous dispersion of nanosilica contains approximately 40 wt% solids. The nanosilica dispersion is sterically stabilized and the amorphous silica nanoparticles carry a negative surface charge. Those silica nanoparticles are discrete, and have a smooth, spherical shape. The Sysmex FPIA-3000 (Malvern) particle size analyzer was used to determine the particle size distribution of nanosilica, Fig. 1. The water shutoff system based on the new composition incorporates two main components: nanosilica and a temperature activated activator.

Essential Experimental Tests

General lab tests for gel water shutoff application are as follows.

Gelation Time Study

Here we define "gelation time" as the initial gelation time in which the viscosity of the gel fluid system turns from initial "zero" growth into an accelerated rapid growth. In a field application, reasonable "gelation time" must be realized to allow safe pumping operation of the fluid through the tubular and into the target zone. The lab test used for this was the high-pressure, high temperature viscometer method by observing the drastic change in fluid viscosity during measurement.

Figure 2 shows a typical viscosity time curve used to determine the "gelation time" of the fluid and the picture of a completely gelled nanosilica-based ANS-HT 200 fluid system. The sample viscosity changes were monitored as a function of time at a given constant shear rate.

Core Flow Test in Porous Media and Fracture

Afterward, evaluating the nanosilica gel and stability

Fig. 1 *Nanoparticle characterization using the Sysmex FPIA-3000 (Malvern) nanoparticle distribution analyzer.*

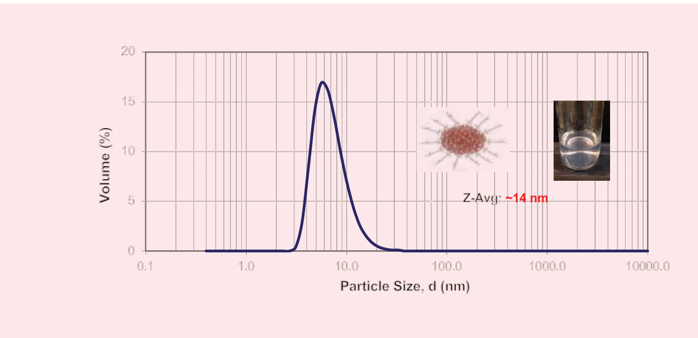

Fig. 2 *A schematic representation of "gelation time" determination by viscosity measurement.*

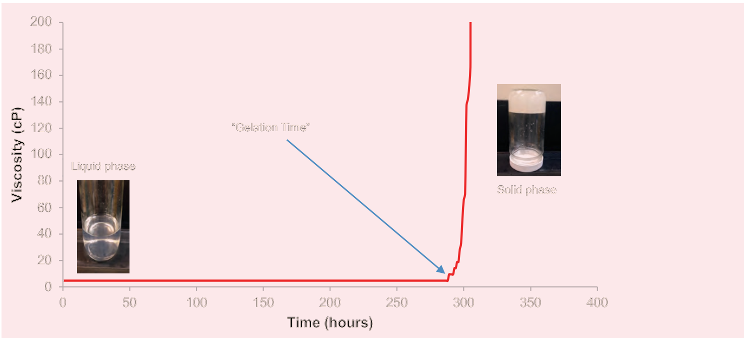

at reservoir conditions, the coreflooding test must be carried out to assess the performance of water shutoff technology, including injectivity in porous media and plugging efficiency. Knowing the injectivity of nanosilica at the initial phase (liquid), i.e., the pressure gradient required a given pumping rate/volume, permits the engineers to design the rate and volume schedule of a water shutoff chemical treatment. After certain curing time, the plugging performance of the water shutoff material must be quantified.

Figures 3a and 3b are process illustrations of the flow test apparatus used in this work. As can be seen, this machine has a Quizix pump, two accumulators, pressure transmitters, core holder, tube, high-pressure steel tubes, and high-pressure valves and a graduated cylinder to measure the volume of effluent.

In this article, the absolute permeability, injectivity, and plugging efficiency were determined by using these test apparatus.

Test Results and Discussions

Gelation Time Study

One of the key parameters that must be determined in lab is the gelation time of the nanosilica water shutoff fluid. The gelation time depends on many factors, including temperature and activator. The gelation time may vary from several minutes to several hours, or even days.

Figure 4 exhibits the changes in the gelation time of different fluid samples for temperatures at 170 °F, 180 °F, 190 °F, and 200 °F, respectively. As can be seen, the gelation time for a definite system, i.e., a system with a concentration of 25% activator, decreases with increasing temperature. The higher the temperature, the lower the zeta potential of the system. Consequently, the colloidal system becomes less stable and the gelation process is activated.

In addition, Fig. 5 depicts the viscosity vs. time for different formulations at 210 °F. The change in the activator's concentration greatly affects the gelation

Fig. 4 Effect of temperature on the gelation time of nanosilica water shutoff technology.

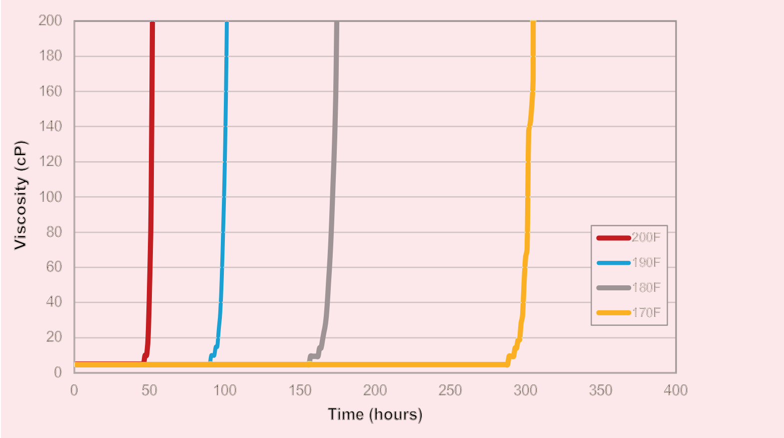

Fig. 5 The effect of the activator concentration on gelation time.

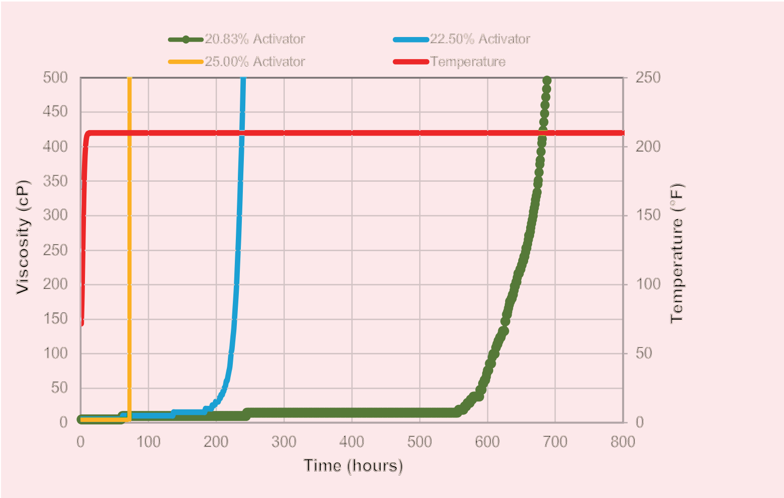

Fig. 3 A process illustration of the core flow test apparatus used in this work.

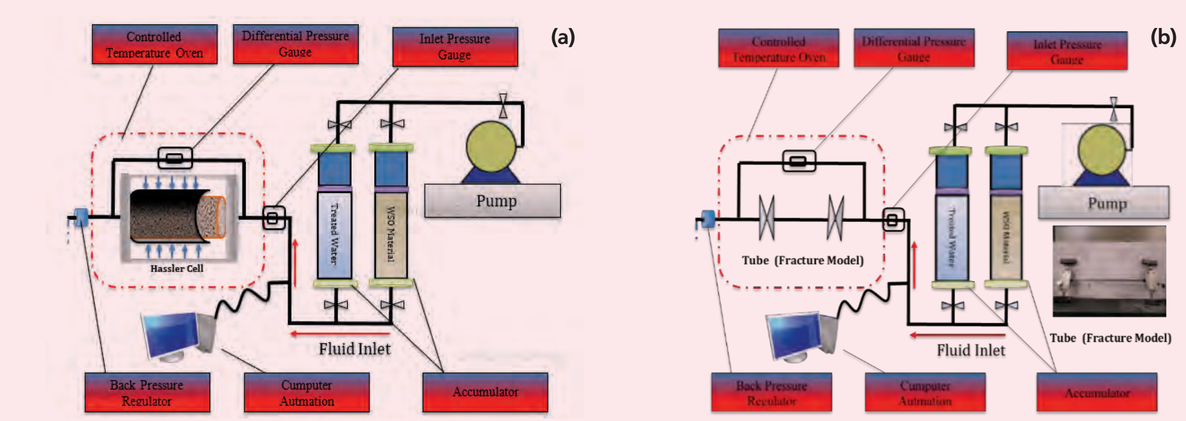

time. As can be seen, with the same nanosilica, as the activator concentration increased from 20.83% to 22.5% and 25%, the gelation time decreased from ~294 minutes to 211 minutes and 73 minutes, respectively.

Coreflooding Studies

Matrix Injectivity

Figure 6 shows the matrix injectivity outcome for a 1.5" diameter and a 3.7" length Brea sandstone outcrop core, with a 25 ml pore volume (PV) and 700 md absolute liquid permeability. Coreflooding experiments were conducted to assess the injectivity of the treatment into the formation, and the ability of a nanosilica-based fluid system for water shutoff application. It is very important to measure the injectivity of water shutoff material before field operation.

The nanosilica fluid system consists of 0.2 vol% surfactant, 0.2 vol% clay control agent, 78.5 wt% nanosilica, and 21.5 wt% activator, which was injected at a 1 ml/min rate at 200 °F. During this stage, 5 PV of chemical was injected in 2 hours. A clay stabilizer and surfactant were added as preflush to prevent clay swelling and improve injectivity of the water shutoff material. A total of 4 PV were injected with little increase in injection pressure, 0.35 psi.

Endurance Test (Long Constant Pressure Experiment)

To ensure the accomplishment of the water shutoff treatment, it is essential that the treatment resides in the targeted zone for a prolonged period of time. If this is not successful, unwanted water production can subsequently embark. Therefore, the durability of the chemical treatment should resist undesired water production for a prolonged period of time.

This was evaluated by carrying out a coreflooding test at 200 °F on the 1.5" diameter by 3.5" length Berea sandstone core. As previously mentioned, the initial permeability of the core with treated water was 700 md. After the curing time of 24 hours is completed, the treated water was injected (post-flush) to evaluate the plugging efficiency of the chemical treatment.

Figure 7 illustrates the pressure drop during all stages with respect to time. As can be seen, there is a sharp increase in injection pressure with a total differential pressure of 500 psi at the initial injectivity test after the treatment is cured. The measured differential pressure is equivalent to 1,621 psi/ft holding pressure for the treated matrix by this water shutoff material. After that endurance test was started and the differential pressure was detained, it was constant at 500 psi for 18 minutes. After running forward, the constant differential pressure increased at several points until it reached 4,000 psi, remaining there for some time. This was followed with an extended period of 317 hours at a differential pressure of 4,000 psi with minimal leakoff through the treated core plug. The averaged measured leakoff rate during this period was 0.0018 cm^3/min. The equivalent drawdown pressure that the core was able to withstand is 12,972 psi/ft — 4,000 psi for a 3.7" core plug.

Characterizing Nanosilica in Porous Media

To determine whether the nanosilica fluid system transported through the core sample, we made a few 1 cm cuts (eight slices) after the treatment and then benchmarked with a sample before the treatment, Fig. 8. Thee sliced samples (1, 5, and 8) were selected to be characterized after the treatment using two different methods: microscopy and SEM (described later).

Figure 9a shows the sliced dry plug before the treatment. As can be seen, the sample has an empty void space and sand grains. Figures 9b, 9c, and 9d are images of the samples — 1, 5, and 8, respectively — after completing the coreflooding test and curing time, which were evaluated to determine the propagation of nanosilica. It can be clearly seen that cured nanosilica fills the void space in the core plug for all samples, which indicates that the treatment can be easily transported all the way to the end. This is confirmed with the

Fig. 6 The results of the water shut off material injectivity test.

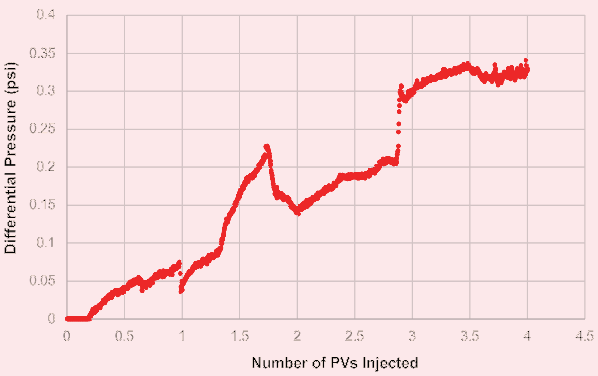

Fig. 7 The durability test to evaluate the stability of the water shutoff material.

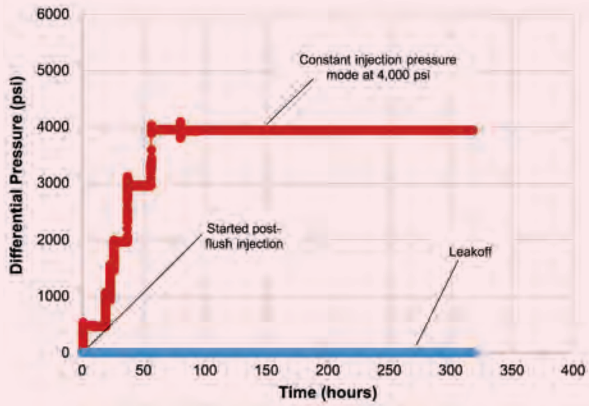

Fig. 8 *Sliced core plug samples after a flooding test.*

Fig. 9 *Microscopic photos of the sandstone core samples (1, 5, and 8) before treatment and after treatment.*

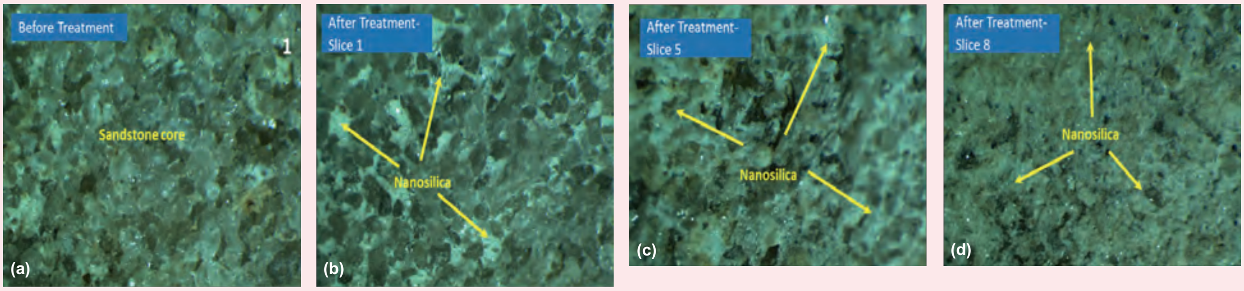

coreflooding test results, as the pressure reached 4,000 psi with no water flow (zero leakoff). This indicates that the nanosilica sufficiently plugged the porous media.

Once the sliced samples are analyzed with microscopy, the same samples (1, 5, and 8) are characterized once again, and the surface of the pore structure was imaged by using SEM. Figure 10 shows the SEM images of the sliced core surface at one resolution, 200 µm. The glass-like material prepared by batch mixing for the nanosilica fluid system is a similar material that was found inside the pore structure of the treated core plug. The untreated core was used from the same core sample and compared with the treated samples. Note that the untreated core surface appears smooth and shiny, while the treated core surface looks rough. This is an agreement with the previous method using the microscopy.

Fracture Model Test

To evaluate the effect of the performance of the nanosilica water shutoff material for a fractured reservoir's void spaces, a 0.25" diameter by 1 ft length tube was used to mimic the real-life voids found in the reservoir. Figure 11 shows the model used. This model consists of one tube and two valves for inlet and outlet, respectively.

Fig. 10 *A SEM photo of the sliced core surface at one resolution (200 µm). Note that the untreated core surface appears smooth and shiny, while the treated core surface looks rough.*

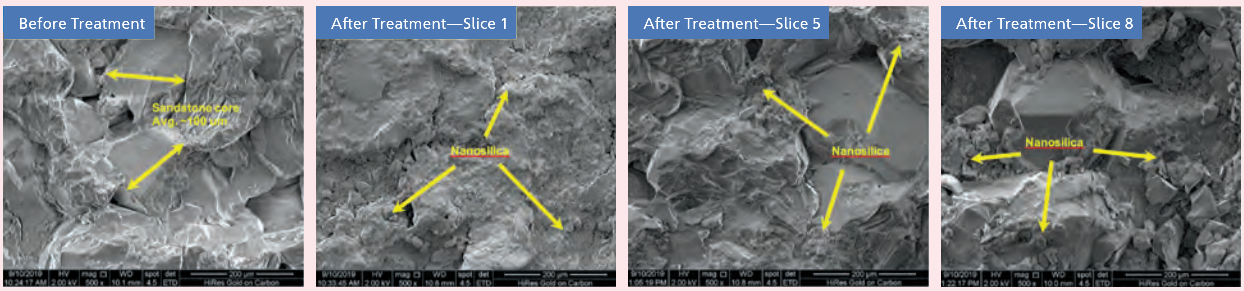

Fig. 11 Fracture model using ¼" tube before treatment.

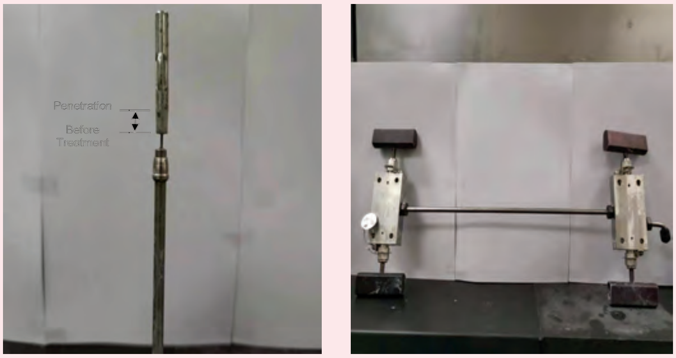

The tube was filled with the chemical shutoff material and placed in the flooding system. Initially, both valves were closed to ensure that the material stays in the tube during the curing time at 200 °F.

The formulation used in this work had a gelling time (25% activator) of 73 minutes. As can be seen, a small metal bar was inserted before the treatment to ensure that the tube is fully open. After the material was cured for 300 minutes, both valves were fully open, and the flow test started by injecting treated water from the inlet. Subsequently, the outlet valve was left open at atmospheric pressure to determine the plugging efficacy of the water shutoff material.

Figure 12 is a graphic diagram of the injection pressure with respect to time. A rapid increase in the injection pressure at 1 ml/min indicates that the tube has been fully blocked. After that, an endurance test was started and the injection pressure was held at 3,000 psi for 1.5 hours with no sign of pressure drop. Additionally, a high-pressure stability test was conducted to assess the holding pressure of the chemical plug. The pressure drop increased to more than 4,000 psi with no evidence of flow through the tube (fracture). The fracture models were then removed and de-assembled to view the existence of the chemical treatment.

Following this, the small metal bar was inserted yet again in the tube. The metal bar could not penetrate through the tube channel, Fig. 13, due to the cured nanosilica. This is in agreement with the core flow test pressure measurements, and proves that this technology could work in fractured reservoirs if the placement design is well engineered.

Conclusions

A novel nanosilica fluid system to use as water shutoff technology was developed and offers competitive advantages over the current technologies:

- The developed fluid water shutoff system is eco-friendly, and environmentally acceptable.
- A single-phase solution with initial low viscosity that can be injected deeply and easily in one step.
- The developed system showed significant pressure increase after treatment with excellent durability and effective water shutoff during the extended coreflooding experiment with great stability at 200 °F.
- Microscopy and SEM images of the sliced core samples showed the presence of nanosilica material inside the porous media.
- A tough gel formed after curing (tested on both matrix and tube up to 4,000 psi).

Acknowledgments

This article was prepared for presentation at the 2021 SPE Middle East Oil & Gas Show, Manama, Kingdom of Bahrain, November 28 – December 1, 2021.

Fig. 12 The flow test results in the ¼" tube (fracture).

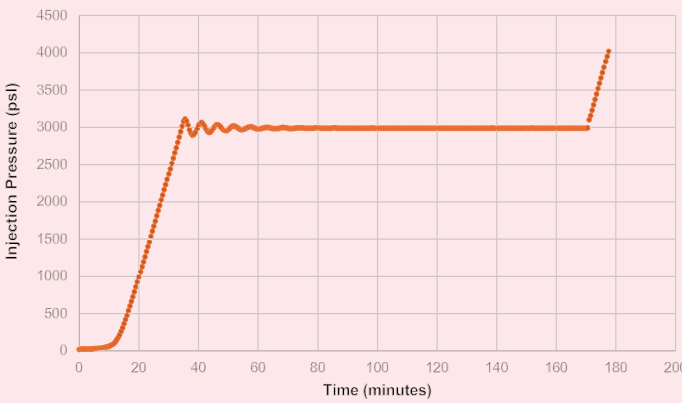

Fig. 13 The fracture model using the ¼" tube after treatment.

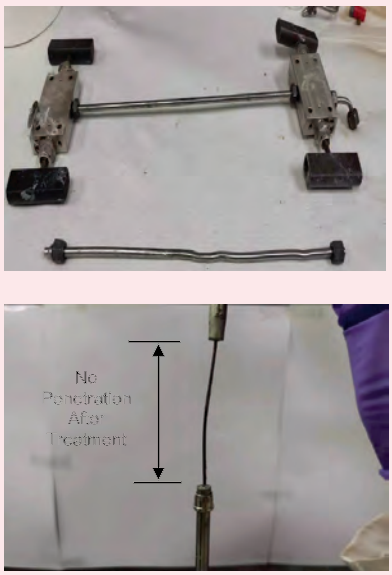

References

1. Almohsin, A.M., Alabdulmohsen, Z., Bai, B. and Neogi, P.: "Experimental Study of Crude Oil Emulsion Stability by Surfactant and Nanoparticles," SPE paper 190440, presented at the SPE EOR Conference at Oil and Gas West Asia, Muscat, Oman, March 26-28, 2018.

2. Salazar Aldana, S.F., Sánchez, R.H., Alviso Zertuche, X.O., Munoz Rivera, M., et al.: "Water Shutoff in Naturally Fractured, Low-Pressure Reservoirs: Case Studies," SPE paper 202422, presented at the SPE Asia Pacific Oil and Gas Conference and Exhibition, Virtual, November 17-19, 2020.

3. Behari, J.: "Principles of Nanoscience: An Overview," *Indian Journal of Experimental Biology*, Vol. 48, Issue 10, October 2010, pp. 1008-1019.

4. Jain, R., Mahto, V. and Sharma, V.P.: "Evaluation of Polyacrylamide-Grafted-Polyethylene Glycol/Silica Nanocomposite as Potential Additive in Water-Based Drilling Mud for Reactive Shale Formation," *Journal of Natural Gas Science and Engineering*, Vol. 26, September 2015, pp. 526-537.

5. Lyu, C., Hao, S. and Yang, L.: "Application of Nanosilica in Glycerol-Based Drilling Fluid for Shale Formations," *SPE Drilling & Completion*, November 2020.

6. Zou, H., Wu, S. and Shen, J.: "Polymer/Silica Nanocomposites: Preparation, Characterization, Properties, and Applications," *Chemical Reviews*, Vol. 108, Issue 9, August 2008, pp. 3893-3957.

7. Elkatatny, S.M., Mahmoud, M.A. and Nasr-El-Din, H.A.: "Characterization of Filter Cake Generated by Water-Based Drilling Fluids Using CT Scan," *SPE Drilling & Completion*, Vol. 27, Issue 2, June 2012, 282-293.

8. Elkatatny, S., Mahmoud, M. and Nasr-El-Din, H.A.: "Filter Cake Properties of Water-Based Drilling Fluids under Static and Dynamic Conditions Using Computed Tomography Scan," *Journal of Energy Resources Technology*, Vol. 135, Issue 4, December 2013, pp. 042201-042210.

9. Abdo, J. and Haneef, M.D.: "Clay Nanoparticles Modified Drilling Fluids for Drilling of Deep Hydrocarbon Wells," *Applied Clay Science*, Vol. 86, December 2013, pp. 76-82.

10. Corredor-Rojas, L.M., Hemmati-Sarapardeh, A., Husein, M.M., Dong, M., et al.: "Rheological Behavior of Surface Modified Silica Nanoparticles Dispersed in Partially Hydrolyzed Polyacrylamide and Xanthan Gum Solutions: Experimental Measurements, Mechanistic Understanding, and Model Development," *Energy and Fuels*, Vol. 32, Issue 10, September 2018, pp. 10628-10638.

11. Zareie, C., Bahramian, A.R., Sefti, M.V. and Salehi, M.B.: "Network Gel Strength Relationship and Performance Improvement of Polyacrylamide Hydrogel Using Nano-Silica; with Regards to Application in Oil Well Conditions," *Journal of Molecular Liquids*, Vol. 278, March 2019, pp. 512-520.

12. Aqcheli, F., Salehi, M.B., Pahlevani, H. and Taghikhani, V.: "Rheological Properties and the Micromodel Investigation of Nanosilica Gel Reinforced Preformed Particle Gels Developed for Improved Oil Recovery," *Journal of Petroleum Science and Engineering*, Vol. 192, September 2020.

13. Mo, D., Yu, J., Liu, N. and Lee, R.: "Study of the Effect of Different Factors on Nanoparticle Stabilized CO_2 Foam for Mobility Control," SPE paper 159282, presented at the SPE Annual Technical Conference and Exhibition, San Antonio, Texas, October 8-10, 2012.

14. Yu, J., An, C., Mo, D., Liu, N., et al.: "Foam Mobility Control for Nanoparticle Stabilized CO_2 Foam," SPE paper 153336, presented at the SPE Improved Oil Recovery Symposium, Tulsa, Oklahoma, April 14-18, 2012.

15. San, J., Wang, S., Yu, J., Liu, N., et al.: "Nanoparticle Stabilized CO_2 Foam Used in Enhanced Oil Recovery: Effect of Different Ions and Temperatures," *SPE Journal*, Vol. 22, Issue 5, October 2017, pp. 1416-1423.

16. Almohsin, A., Huang, J., Karadkar, P. and Bataweel, M.: "Nanosilica-Based Fluid System for Water Shut-Off," WPC paper 22-0468 presented at the 22nd World Petroleum Congress, Istanbul, Turkey, July 9-13, 2017.

17. Jin, J., Wang, Y., Wang, L., Zhang, X., et al.: "The Influence of Gas-Wetting Nanofluid on the Liquid-Blocking Effect of Condensate Reservoir," SPE paper 182350, presented at the SPE Asia Pacific Oil and Gas Conference and Exhibition, Perth, Australia, October 25-27, 2016.

18. Vipulanandan, C., Mohammed, A.S. and Samuel, R.: "Smart Bentonite Drilling Muds Modified with Iron Oxide Nanoparticles and Characterized Based on the Electrical Resistivity and Rheological Properties with Varying Magnetic Field Strengths and Temperatures," OTC paper 27626, presented at the Offshore Technology Conference, Houston, Texas, May 1-4, 2017.

19. Fakoya, M.F. and Shah, S.N.: "Effect of Silica Nanoparticles on the Rheological Properties and Filtration Performance of Surfactant-Based and Polymeric Fracturing Fluids and Their Blends," *SPE Drilling & Completion*, Vol. 33, Issue 2, pp. 100-114.

20. Mahmoud, O., Nasr-El-Din, H.A., Vryzas, Z. and Kelessidis, V.C.: "Using Ferric Oxide and Silica Nanoparticles to Develop Modified Calcium Bentonite Drilling Fluids," *SPE Drilling & Completion*, Vol. 33, Issue 1, March 2018, pp. 12-26.

21. Boul, P.J., Ye, A., Pang, X., Goel, V., et al.: "Nanosilica-Based Conformance Gels," SPE paper 174265, presented at the SPE European Formation Damage Conference and Exhibition, Budapest, Hungary, June 3-5, 2015.

22. Shamlooh, M., Hamza, A., Hussein, I.A., Nasser, M.S., et al.: "Reinforcement of Polyacrylamide-Co-Tert-Butyl Acrylate Base Gel Using Nanosilica for Conformance Control at Low and High Reservoir Temperatures," SPE paper 199324, presented at the SPE International Conference and Exhibition on Formation Damage Control, Lafayette, Louisiana, February 19-21, 2020.

23. Zhu, D., Bay, B. and Hou, J.: "Polymer Gel Systems for Water Management in High Temperature Petroleum Reservoirs: A Chemical Review," *Energy & Fuels*, Vol. 31, Issue 12, November 2017, pp. 13063-13087.

24. Shamlooh, M., Hamza, A., Hussein, I.A., Nasser, M.S., et al.: "Investigation of the Rheological Properties of Nanosilica-Reinforced Polyacrylamide/Polyethyleneimine Gels for Wellbore Strengthening at High Reservoir Temperatures," *Energy & Fuels*, Vol. 33, Issue 7, May 2019, pp. 6829-6836.

25. Huang, J., Al-Mohsin, A., Bataweel, M., Karadkar, P., et al.: "Systematic Approach to Develop a Colloidal Silica-Based Gel System for Water Shut-Off," SPE paper 183942, presented at the SPE Middle East Oil and Gas Show and Conference, Manama, Kingdom of Bahrain,

March 6-9, 2017.

26. Karadkar, P., Almohsin, A., Bataweel, M. and Huang, J.: "In Situ Pore Plugging Using Nanosilica-Based Fluid System for Gas Shutoff," SPE paper 197578, presented at the Abu Dhabi International Petroleum Exhibition and Conference, Abu Dhabi, UAE, November 11-14, 2019.

About the Authors

Dr. Ayman M. Al-Mohsin

Ph.D. in Petroleum Engineering, Missouri University of Science and Technology

Dr. Ayman M. Al-Mohsin joined Saudi Aramco in 2014 as a Research Engineer. He is currently a Petroleum Engineer working in Smart Fluid Focus Area in the Production Technology Division of Saudi Aramco's Exploration and Petroleum Engineering Center – Advanced Research Center (EXPEC ARC). Ayman's research interests include water and gas shutoff using chemical means.

He received his B.S. degree in Mechanical Engineering from the University of New Haven, West Haven, CT; his M.S. degree in Petroleum Engineering from New Mexico Tech, Socorro, NM; and his Ph.D. degree in Petroleum Engineering from Missouri University of Science and Technology, Rolla, MO.

Dr. Jin Huang

Ph.D. in Inorganic Chemistry, University of Houston

Dr. Jin Huang is a Petroleum Scientist working with the Production Technology Division of Saudi Aramco's Exploration and Petroleum Engineering Center – Advanced Research Center (EXPEC ARC). Her current research interests are water management related oil field chemistry.

Prior to joining Saudi Aramco in 2015, Jin worked as a Chemist for Weatherford Laboratories Inc. and Intertek Westport Technology Center in Houston, Texas. She was intensively involved in reservoir fluids analysis, drilling fluid analysis, and water chemistry. Jin also worked at GTC Technology Inc. in Houston as a Process Chemist, and worked as a postdoctoral researcher at Texas A&M University, College Station, Texas.

In 1994, Jin received her B.S. degree in Polymer Chemistry from Tianjin University, Tianjin, China; and in 2004, she received her Ph.D. degree in Inorganic Chemistry from the University of Houston, Houston, TX.

Mohammed I. Alabdrabalnabi

B.S. in Chemical Engineering, King Fahd University of Petroleum and Minerals

Mohammed I. Alabdrabalnabi joined Saudi Aramco in August 2015 as a Petroleum Engineer with the Production Technology Division of Saudi Aramco's Exploration and Petroleum Engineering Center – Advanced Research Center (EXPEC ARC).

His research interests include fracturing fluids, water shutoff fluid systems, sand control, and condensate banking.

Mohammed received his B.S. degree in Chemical Engineering from King Fahd University of Petroleum and Minerals (KFUPM), Dhahran, Saudi Arabia.

Mohamed H. Sherief

B.S. in Chemical Engineering, Cairo University

Mohamed H. Sherief is a Petroleum Engineering Specialist working in the Shaybah Unit of Saudi Aramco's Southern Area Reservoir Management Department. He has more than 22 years of experience in oil and gas exploration, field development planning, and production operations.

Prior to Saudi Aramco, Mohamed worked for major IOC/NOC players, including an international reservoir engineering studies consulting firm.

He is a member of the Saudi Council of Engineers and a member of the Society of Petroleum Engineers (SPE), and a Certified Petroleum Engineer.

Mohamed received his B.S. degree in Chemical Engineering from Cairo University, Giza, Egypt.

First Worldwide Slim Coiled Tubing Logging Tractor Deployment

Laurie S. Duthie, Hussain A. Al-Saiood, Abdulaziz A. Anizi and Dr. Norman B. Moore

Abstract /

Successful reservoir surveillance and production monitoring is a key component for effectively managing any field production strategy. For production logging in open hole horizontal extended reach wells (ERWs), the challenges are formidable and extensive; logging these extreme lengths in a cased hole would be difficult enough, but are considerably exaggerated in the open hole condition. A coiled tubing (CT) logging run in an open hole must also contend with increased frictional forces, high dogleg severity (DLS), a quicker onset of helical buckling and early lockup. The challenge to effectively log these ERWs is further complicated by constraints in the completion where electric submersible pumps (ESPs) are installed, including a 2.4" bypass section.

Although hydraulically powered CT tractors already exist, a slim CT tractor with real-time logging capabilities was not available in the market. In partnership with a specialist CT tractor manufacturer, a slim logging CT tractor was designed and built to meet the exceptional demands to pull the CT to target depth. The tractor is 100% hydraulically powered, with no electrical power, allowing for uninterrupted logging during tractoring. The tractor is powered by the differential pressure from the bore of the CT to the wellbore, and is operated by a preset pump rate from the surface.

Developed to improve the low coverage in open hole ERW logging jobs, the tractor underwent extensive factory testing before being deployed to the field. The tractor was rigged up on location with the production logging tool (PLT) and ran in the hole. Once the CT locked up, the tractor was activated and pulled the coil to cover over 90% of the open hole section, delivering a pulling force of up to 3,200 lb. Real-time production logging was conducted simultaneously with the tractor activated, and flowing and shut-in passes were completed to successfully capture the zonal inflow profile. Real-time logging with the tractor is logistically efficient and allows instantaneous decision making to repeat passes for improved data quality.

The new slim logging tractor (SLT) is the world's slimmest and most compact, and the first of its kind CT tractor that enables production logging operations in horizontal extended reach open hole wells. The ability to successfully log these ERWs cannot be understated; reservoir simulations and management decisions can only be as good as the quality of data available. Some of the advantages of drilling ERWs, i.e., increased reservoir contact, reduced footprint and a reduced number of wells drilled, will be lost if sufficient reservoir surveillance cannot be achieved. To maximize the benefits of ERWs, creative solutions and innovative designs must continually be developed to push the boundaries further.

Background

Challenges associated with coiled tubing (CT) reach in extended reach wells (ERWs) are well documented in the technical literature[1]. Frictional forces acting on the CT, weight stacking and helical buckling of the coil eventually lead to a lockup, and no further progression can be made. To delay the onset of lockup, several techniques are employed, these include pumping friction reducers, the use of tapered CT, organic solvents, and a hole clean out procedure. For the ERWs, even with all of the above implemented, reaching target depth was out of reach, and additional measures were required to convey the logging tools to target depth.

Introduction

Although a slim CT tractor already existed and has been extensively used for matrix acid stimulations in open hole ERWs, this CT tractor did not allow for real-time logging. The development of a real-time slim logging tractor (SLT) was seen as an essential and logical step in the evolution of these tractor designs. For effective reservoir monitoring and management, this project was seen as a high priority and company resources were deployed to design and produce a fit for purpose technology for these ERWs.

Although it may seem a simple task to modify the existing CT stimulation tractor into a logging tractor, this was not the case. The tractor required significant design changes to include a feedthrough for real-time

Fig. 1 Well completion schematic.

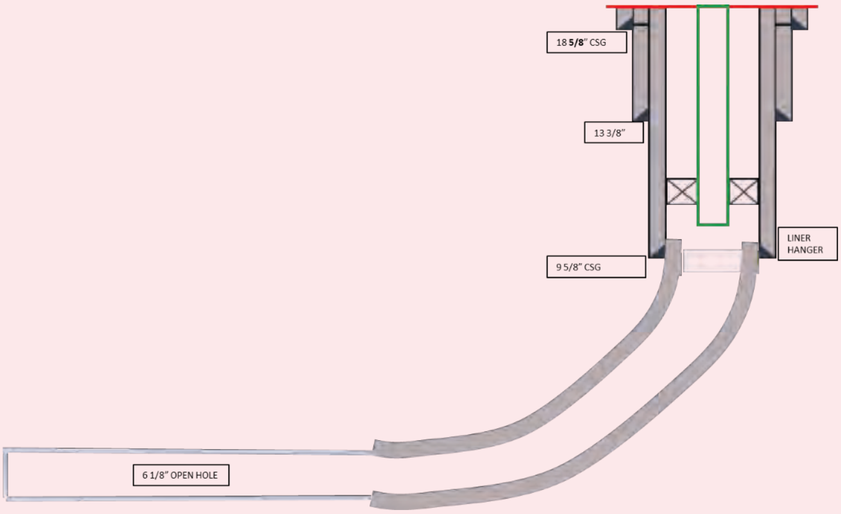

logging and at the same time cope with a variable open hole terrain and still maintain the same performance and deliver enough pulling force. The timeline for the project was fairly aggressive, from the initial go ahead for the design process to delivery of the final product within 2 years.

Well Information/Completion

The typical well completion consists of 9⅝" casing with 4½" tubing, an electric submersible pump (ESP) with a bypass section and a 7" liner set in the horizontal section. The laterals are drilled to a 6⅛" open hole size in a carbonate formation, where the lengths of the open hole lateral sections can be up to 10,000 ft with the longest well at over 30,000 ft in total measured depth (MD), Fig. 1.

Figure 2 illustrates a 3D deviation profile.

Fig. 2 A 3D well deviation profile.

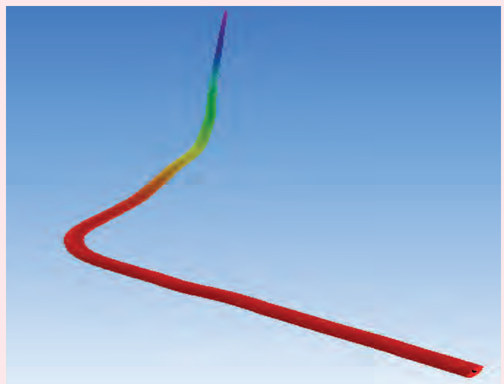

Challenges to Logging Open Hole ERWs

Challenges to logging open hole ERWs are extensive and formidable, and detailed planning and preparation is required to have the best chance of overcoming these challenges. To achieve the main objectives of the logging intervention, one of the key elements is to cover as much of the open hole section as possible. Some of the critical challenges are discussed here:

1. **Extended reach open hole sections:** The longer the open hole section, the tougher the climb. This is, of course, a generalization, and a number of other factors come into force to determine how far the CT will progress. Subsequently, from operational experience in hundreds of ERW CT interventions, most wells up to a 12,000 ft length, can be covered 100% without any additional pulling force. Even up to around 14,000 ft, there is an above 50% chance that target depth can be reached. Above around 14,000 ft, things start to get progressively more difficult, and by 16,000 ft, there are few ERWs that target depth can be reached without additional pulling force. These lengths are not rigid, and are just a rule of thumb, but the message is: the longer the lateral section, the more likely additional pulling force will be required.
2. **Undulating horizontal laterals:** The ERW laterals are rarely a straight 90° section. It is normal to see some deviation, and this can give rise to an undulating terrain. This increases frictional forces acting against the CT, resulting in an early lockup depth.
3. **CT stuck in hole:** Similar to the length of open hole sections, a similar rule applies to the risk of CT pipe becoming differentially stuck in the hole. At shorter intervention lengths — less than 14,000 ft — the risk of becoming stuck in the hole is very

low. The risk increases progressively the further the CT is run in hole (RIH), and also the severity. Differentially stuck situations at less than 16,000 ft are normally mild and can be resolved reasonably easily.

For lengths of over 20,000 ft, becoming differentially stuck can become a more serious situation. For mechanically stuck situations, several options are available to release the bottom-hole assembly (BHA).

4. **Completion size limitations:** The ERWs are oil producers with artificial lift in the form of ESPs installed. To access the laterals, a bypass section allows for entry into the lateral, where the ESP is installed in a parallel configuration. This section of the completion is installed in a 9⅝" casing, the limited size available for all components, including the ESP and bypass sections, introduces a restriction of 2.441" in the bypass section.

   The tractor must therefore be able to collapse to pass through the restriction, yet be able to expand enough to grip the open hole. This constraint has implications on the tractor design, since there is a direct relationship between the maximum pulling force and the size of the tool body. This relationship relies upon a sufficient cross-sectional area of the hydraulic piston within the tool body to produce the powerful pulling force.

5. **Oversized hole sections:** During the intervention, oversized sections may be encountered. This could be caused where the reservoir rock has been enlarged during drilling, or in unconsolidated formations or washouts during stimulation operations.

   This is an important point to consider, as the SLT is designed to work in 6⅛" hole sizes and can operate with a maximum opening of 7.4". Therefore, larger hole sizes than this can only be passed if they are short enough in length for the tractor to traverse across them. Although it would be ideal to have a tractor that has a wider operating range, this compromise would adversely affect the performance of the tractor.

6. **Dogleg severity (DLS):** The definition of DLS is the change in well trajectory, described in degrees per 100 ft of hole drilled. The difficulty in terms of well intervention with high DLS is the increased points of contact for the CT and corresponding frictional forces. Since the DLS cannot be changed, the effects of this in the well trajectory are modeled in the depth reach simulation, and the information used accordingly.

7. **Viscous fluids:** Highly viscous fluids are another challenge that may be encountered. These fluids can increase the overall drag forces and friction coefficient seen by the CT during the intervention. As a contingency, organic solvents can be pumped along the hole in the shut-in condition to reduce the viscosity and the resulting friction coefficient.

8. **Obstacles in the open hole section:** Obstacles in the form of solid organic deposits can be encountered during the pre-logging drift run and prevent further progress along the hole. As per the solution for viscous fluids, organic solvents can be applied and left to soak to dissolve these barriers.

9. **Harsh downhole environments:** A number of other harsh conditions can exist to add to the already complex objective of successfully logging an ERW. One of those present is high concentrations of hydrogen sulfide (H_2S), and is a concern where this corrosive gas may attack the CT, tractor components, and logging tools.

10. **Robustness of logging tools:** One of the frequent problems during the logging of open hole ERWs is the failure or damage of the logging tools sensors. The open hole environment can be unforgiving. Although the logging tools are built to handle downhole conditions, they are still susceptible to damage in these demanding conditions. For the array spinner tools, the small spinners can become stuck or broken, especially the ones that are located toward the lower side of the hole where any solids may be lying. The other sensors, such as water holdup, can also be damaged or fail to give correct readings when covered in thick organic materials. Continued development of new and more robust logging tools are a must to successfully log these ERWs[2].

Memory or Real-Time Production Logging

One early decision to make for the PLT selection is whether memory or real-time logging tools will be deployed. For standard production logging, the data quality in terms of tool performance should be identical whether memory or real-time tools are used. The advantage for memory logging tools is a simpler deployment with less equipment, no power or data communications required from the surface. This inevitably leads to a more cost-effective operation, but this has to be assessed on a case by case basis, and while this option may be suitable for shorter or cased hole horizontal wells, it would rarely be suitable for extended reach open hole wells.

For operations in extended reach open hole wells where the job duration may last several days, the risk with using memory tools is that the tools may become damaged at an early stage during the logging, and will not be discovered until the tools are recovered to the surface. In this case, where the data recovered is incomplete and the logging requires the action to be repeated, the economic advantage of running memory logging tools quickly turns into its Achilles heel.

In the real-time mode, apart from the advantage of knowing instantaneously when any tool malfunction has occurred, there are techniques to resolve some problems without pulling out of the hole. For example, a stuck spinner may be cleared by positioning the tool in a high flow rate area to remove any material plugging the spinner, or chemical solvents can be pumped from the surface to flush any sensors blocked by tar or asphaltenes[2].

Production Logging Applications

In addition to the primary use of production logs to determine the distribution of flow along the hole, listed here are several other important reasons for the production logs to be run:

- The diagnostic tool can determine problems with completions, such as casing leaks and behind casing flow.
- To identify acid stimulation candidates.
- To identify side track candidates.
- Pre-acid stimulation to identify noncontributing zones for a more targeted stimulation program.
- Post-acid stimulation to determine the effectiveness of the stimulation.
- Improved reservoir understanding, providing data to update and calibrate reservoir models.
- To investigate water production or unexpected increases in water cut and to improve the water management.
- Detection of thief zones and/or fractures.
- Detection of preferential flow of water through high permeability streaks in the formation[2].

Previous Logging Method

Prior to the introduction of the slim production logging tractor, logging of ERWs was mostly restricted at the shorter end of the ERW spectrum. A list of key wells are selected for logging, and from that list, depth reach simulations are run to find the estimated coverage of the open hole. Of course, it is always desirable to cover the entire open hole to obtain the full flow profile along the hole; however, this is not always possible with these ERWs.

Since 100% coverage is not always practical, a lower target could be set if the main objectives for that particular logging operation could still be achieved. Before the logging tractor was developed, simulations for the longer ERWs could have very low coverage, and for these types of wells, no logging at all was possible.

Tractor Design

The CT SLT was created to facilitate CT services to deliver live logging data from complex extended reach production wells containing a 2.4" installed ESP for surface evaluation. The SLT has a maximum outer diameter of 2.12" to allow passage through the restrictions of the ESP bypass. The SLT is powered by the differential pressure from the bore of the CT to the wellbore annulus of the intervention fluid, typically diesel or water. The fluid delivers power to hydraulic cylinders that activate grippers to provide the pulling force at the end of the CT behind the logging tools.

Figure 3 shows an overview of the SLT, which consists of a shaft assembly (SA) with an eccentric link gripper (ELG), a static gripper (SG), an isolation nozzle sub (INS), and a relief valve sub (RVS).

1. The SA with an ELG: The ELG expands to grip the 6⅛" open hole, and the SA provides tractor pulling force.
2. The SG maintains position during tractor reset stroke.
3. The INS filters the tractor's operational fluid, isolates the tractor from pressure below the desired threshold for activation, and is the anchor point for Inconel fiber carrier (IFC).
4. The RVS regulates the system pressure.

The SLT utilizes an ELG and an SG that are coordinated via a hydraulic circuit to produce a repeating motive force. The SA contains a hydraulic cylinder, and when powered uses the ELG to "pull" the tractor, logging tools, and CT downhole. Once the hydraulic cylinder achieves the end of its motive force producing stroke, the SG is energized as the ELG releases during reset, thereby preventing the CT and logging tools springing back up hole with CT string tension.

Once the hydraulic cylinder is fully reset, the SG releases as the ELG grips and begins another force producing cycle. This repeating cycle results in an "inch-worm" like motion when RIH operations. The tractor operation of the tool from the surface is activated by increasing the pump rate to a preset pump rate limit. The tractor can be turned off by reducing the pump rate to below the preset level.

Reactivation of the tractor simply requires the pump rate to be set to zero, and again increasing the pump rate to the preset level to restart the tractor. Other design features of the SLT include the following:

- Continuous traction to pull up to 3,500 lb.
- Compact 29 ft length.
- All hydraulic operation and controls (no electric power required).
- Debris tolerant.
- Grips without damaging the casing or formation.
- Compatible with almost all intervention fluids.
- Resistant to harsh environment environments.

Design Challenges

The design of the SLT had several technical challenges. The foremost challenge was the dual requirement for a slim outside diameter (2.13") of the tool in combination with the requirement for a pass-through live logging conduit. The minimum diameter of the SLT through bore is 0.367" and the live logging conduit diameter is 0.125". In addition, the through bore that is not filled with the logging conduit must supply adequate fluid to power the SLT and power any additional hydraulic tools, such as an anti-compression sub, which is used to prevent damage to the logging BHA, or hydraulic window finding tools.

Geometric restrictions on the SLT necessitated using a simplified hydraulic circuit and components to better utilize the energy with the tool's centerline fluid. The result was up to 30% faster speed (22 ft/min) than achieved with other designs.

A second challenge for the SLT were the fail-safe features to assure retrieval of the BHA in the event of downhole problems. The primary fail-safe mechanism is a coiled spring that forces the grippers to retract if there is no centerline pressure. In addition, a secondary fail-safe mechanism is included with shear pins located in both grippers that forces the arms closed by pulling out of the hole (POOH) with 7,000 lb pull.

A third challenge for the SLT was gripper design; the ELG is subjected to both high loads and abrasive downhole conditions. This challenge was met with improvements in stress distribution in the components of the gripper.

Manufacture

With the design completed, drawing released, and component materials specified, manufacturing began. Materials used in the SLT include Inconel (SA), steel (SA), copper beryllium (ELG and SG), tungsten carbide (valves), and elastomers (O-rings). When the components became available, subassemblies and major assemblies were assembled, and functionally tested. Upon assembly of two complete SLTs, the tool functional development began.

Tool Development Testing

The objective of tool development testing was to reduce risk of field problems. Shop testing included testing the tractor hydraulic circuit reliability, gripper endurance, gripper reliability when exiting casing into a washout, gripper fail-safe operation, fully loaded tractor endurance testing, and anti-compression sub functionality.

The SLT's hydraulic circuit was successfully functionally tested on a jack stand and verified its ability to continuously cycle between power and reset, Fig. 4.

The SLT's gripper was endurance tested using a built for purpose test apparatus consisting of a 7" casing hydraulic cylinder with frame, Fig. 5. The gripper was endurance tested to 3,200 lb for tractor force followed by a small compressive push, simulating the tractor reset process. The gripper successfully completed 6,000 cycles — equivalent to 18,000 ft of tractoring in casing. The gripper remained completely functional throughout; after the endurance test, the gripper elements were examined and showed only normal wear.

A test was conducted to verify the gripper's reliability when exiting casing into a washout. A gripper was strategically placed partially exited from the 7" casing to simulate exiting into an open hole washout. When the gripper partially exits the casing, the gripper sees a maximum stress condition. The test was performed for 20 cycles at 3,200 lb pull without damage to any of the major components, Fig. 6.

A fail-safe operation of the grippers produced a reliable and consistent activation after the evaluation of multiple redesigns. The SLT gripper was installed into a fixture, operated for 2,000 cycles at a maximum tractor load of 3,000 lb and left energized; fail-safe mechanisms were tested in over pull condition. The testing results showed that the activation load within 0.5% of the design load.

Figure 7 shows the SLT gripper fail-safe operation.

A comprehensive tractor endurance test verified the tool's ability to operate successfully under maximum load conditions. The SLT was loaded into a test section of a 7" L-80 casing for a resistive load test, where a resistive load fixture applies a resistive load (simulating CT drag) to the SLT. The load is delivered via a chain and chain tensioner assembly with a hydraulic braking system. The SLT is activated by delivering pressurized water to the centerline of the tractor via hoses, and when activated pulls against the resistive load. The SLT successfully "walked" 4,000 ft and maintained all critical functions, including on/off functionality, ELG and SG expansion and collapse, and fail-safe functionality.

An integral anti-compression sub test verified the ability to activate the SLT in the event that the logging BHA encountered any obstruction resulting in a 350 lb compressive force. The anti-compression sub successfully completed six consecutive functional tests demonstrating immediate deactivation of the tractor. The test verified damage would be avoided if the SLT and the logging BHA encountered any obstruction downhole.

A yard test verified the functionality of the SLT when connected to a wireline logging BHA via a feed-through cable. A function test with the SLT connected to the wireline BHA, pumped over a range of rates from 0.4 bbl/min to 0.9 bbl/min, and the tractor turned on and then cycled continuously until stopped.

Figure 8 shows the yard testing complete BHA, and Fig. 9 shows the SLT during yard testing.

Field Deployment #1

With the extensive shop and yard testing completed, field deployment planning began to meet the objective.

Fig. 3 The CT SLT components.

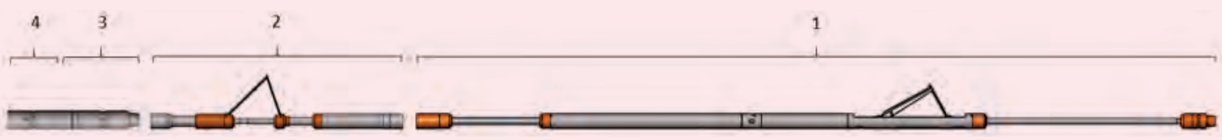

Fig. 4 The hydraulic circuit functional testing of the CT SLT.

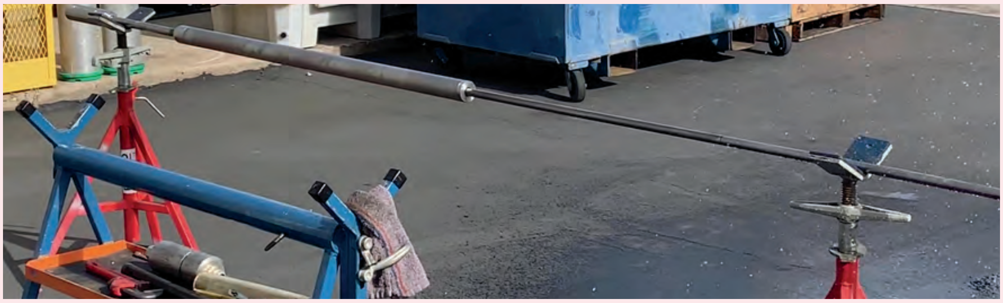

Fig. 5 The SLT endurance test fixture.

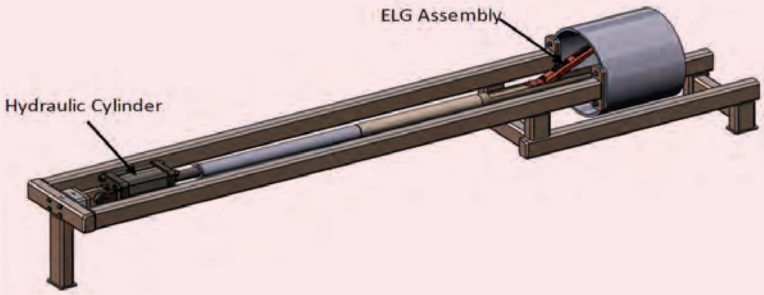

Fig. 6 The SLT gripper exiting a 7" casing survival test.

Fig. 7 The side view of the SLT fail-safe operation before and after activation.

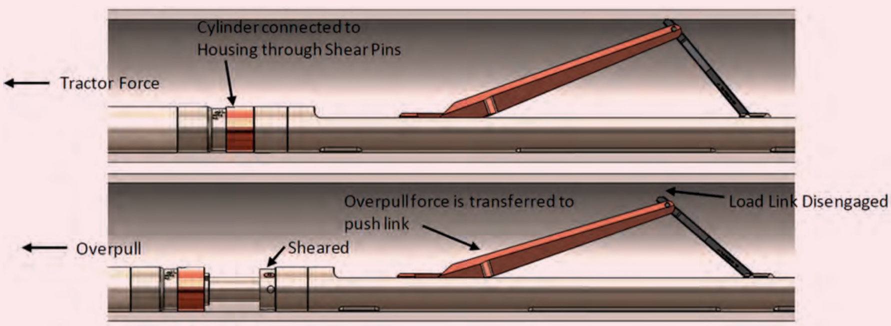

Fig. 8 *The BHA for yard testing of the SLT and wireline logging tools.*

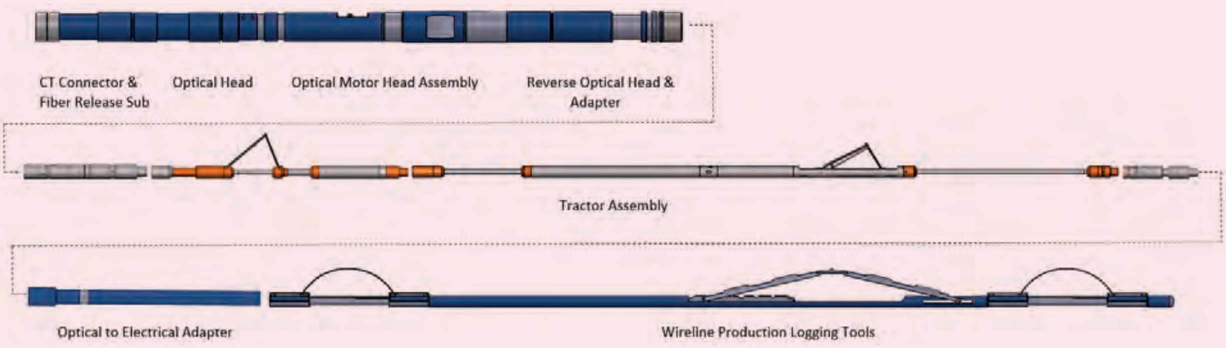

Fig. 9 *The CT SLT and wireline logging BHA function test.*

For the first field deployment, the job program required two runs: (1) The SLT with a dummy logging tool string, and (2) The SLT with a live logging tool string.

Before the deployment, the tubing force analysis estimated that for a 2" coil, the friction coefficient should range from 0.25 to 0.3. The simulation showed that without a tractor on the BHA, the target depth of 15,913 ft could not be achieved and the SLT was essential to meet the objective. Past experience has proven that the friction reducer is only effective during the shut-in condition, and

Fig. 10 *The CT depth reach simulation with a friction reducer.*

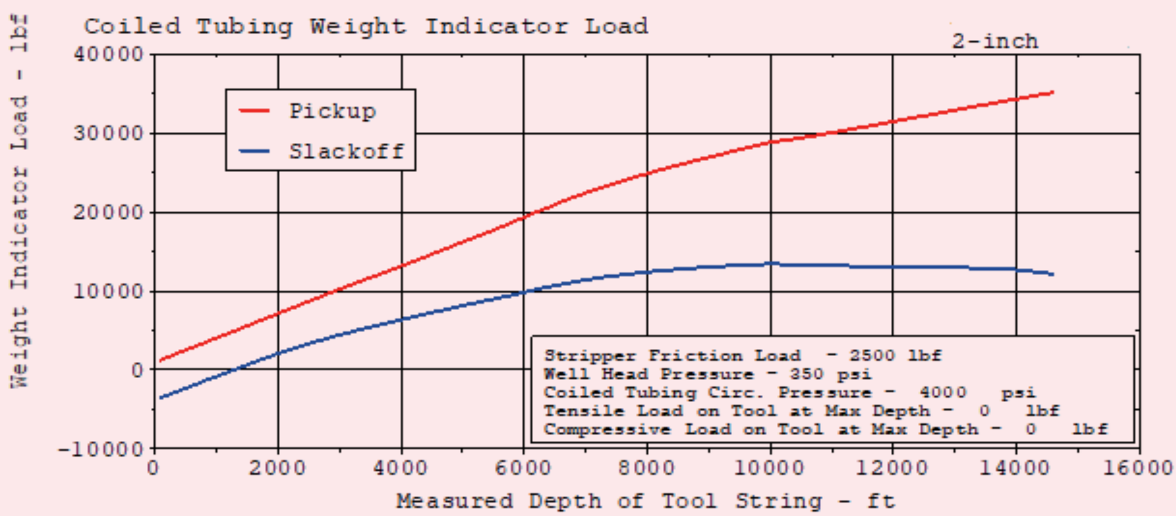

Fig. 11 The SLT in a function stand-alone test.

Fig. 12 The surface pressure control rig up.

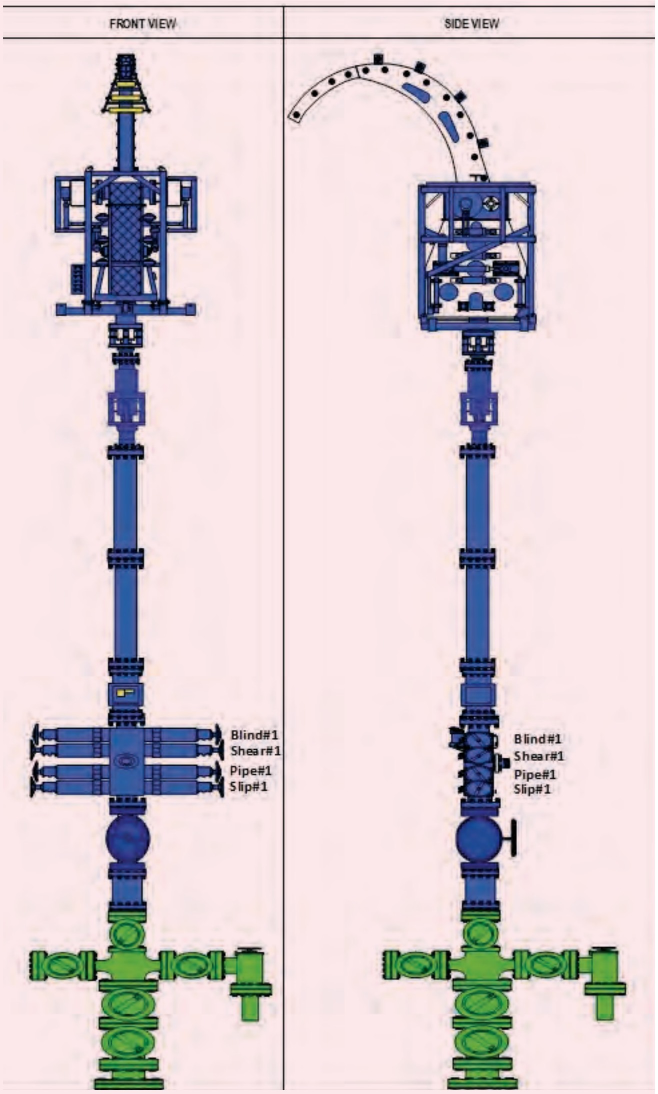

is pumped from the end of the tubing to the end of the liner section; no friction reducer is pumped in the open hole. A simulation was run to estimate the effect of the friction reducer without the tractor being activated. The cumulative benefit was an additional 400 ft, Fig, 10.

For each run, the SLT was function tested stand-alone prior to rigging up on CT, Fig. 11.

After a successful stand-alone test, the armored IFC was passed through the RVS/INS subs and SLT to the logging tools below. The compact design of the tractor and logging tools — a total length of 70 ft — allowed for a standard lubricator pressure control system to be rigged up, Fig. 12. The entire BHA was successfully function tested and the assembly RIH.

At 7,800 ft MD, a tractor subsurface test was performed. An increase in injector weight verified the tractor had activated and was pulling properly. The CT continued RIH until lockup, and at 13,490 ft the injector weight dropped, indicating CT lockup. The CT was POOH to 13,274 ft MD to remove CT buckling and the SLT was activated. The CT continued tractor assisted RIH until 13,605 ft MD when the injector weight dropped, indicating no further advancement.

Tractor operation was verified by surface weight observations; lack of progress indicated a washout greater than the extension capability of the tractor grippers. The BHA was POOH to 7,000 ft MD, pumping friction reducer and RIH to pass 13,605 ft MD before activating the tractor. After pumping friction reducer, the CT passed 13,605 ft reaching 14,500 ft MD. Note that the application of friction reducer added 900 ft, 500 ft more than the simulation had estimated. The SLT was then activated, successfully pulling the BHA to 15,475 ft when the weight dropped. Three efforts to pass 15,475 ft MD were unsuccessful; the SLT was POOH to the surface and inspected. The tractor suffered a load link failure, Fig. 13, in the SG assembly, and a sequencing failure due to a blocked bleed in the tractor's main valve.

For the second SLT run, Fig. 14, the pre-run tests were repeated, including stand-alone tests, function pressure tests rigged up to the live logging tools in

Fig. 13 An image of the SG's load link failure.

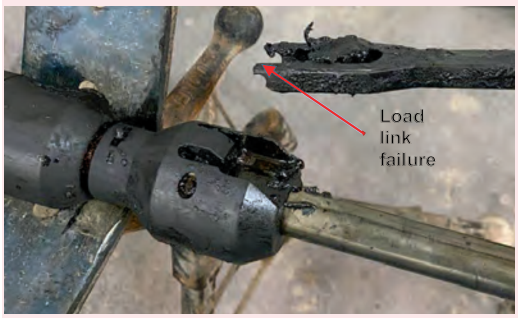

Fig. 14 *The first field deployment, second run, RIH with the SLT activated.*

the wellhead stack, and RIH. At 7,000 ft MD, RIH was stopped, the ESP turned on, waited until flow stabilized, and performed logging tool calibrations. At 7,800 ft MD, the tractor function test was successful.

Since the well had only been drifted to 15,315 ft, this depth was not to be exceeded to avoid the potential damage to the logging tools. The CT did reach 15,315 ft MD and the tractor was stopped, logging passes were conducted as per program and the job was completed.

Tractor Upgrades after First Trial

Control Valve Plugging: The pilot area of the hydraulic control valve that became plugged was redesigned to provide a significantly larger flow area for pilot fluid to exit when shifted.

SG Load Link: The probable cause of the SG load link failure is accumulated debris between the sleeve and link, preventing full collapse. When the partially expanded link encountered a restriction while POOH, there is a long lever arm generating high loads in the pinned connection where the link failed. The sleeve was redesigned by removing excess metal to prevent accumulation of debris and reoccurrence of this failure.

ELG Load Link: The ELG load link from both runs exhibited excessive wear to the gripping end, Fig. 15. The excessive wear of the link was attributed to slippage. The ELG load link was modified to reduce the surface pressure area to improve the open hole gripping performance, Fig. 16.

Field Deployment #2

For the second trial, a more challenging well was selected to test the effectiveness of the upgrades after the

Fig. 15 *Excessive wear on the ELG load link.*

first trial. The open hole coverage was increased from 15,074 ft (28% of open hole) all the way to target depth at 17,747 ft (100% coverage of the open hole), while the horizontal lateral section was extended to nearly 8,000 ft. As per the first trial, multiple runs were made with some problems encountered.

On the first run, several attempts were made to activate the tractor inside the casing, but no significant progress was made. At the surface, the ELG load link showed clear indication of wear from repeated cycling, Fig. 17. There were a number or modifications done to the gripping element in regards to both material properties and open hole/ casing interface geometries after the first trial.

Since the tractor demonstrated poor gripping inside

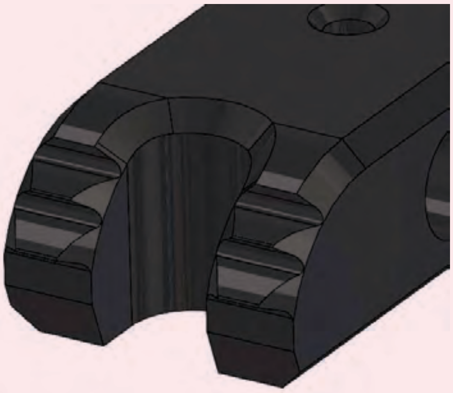

Fig. 16 *The improved SG.*

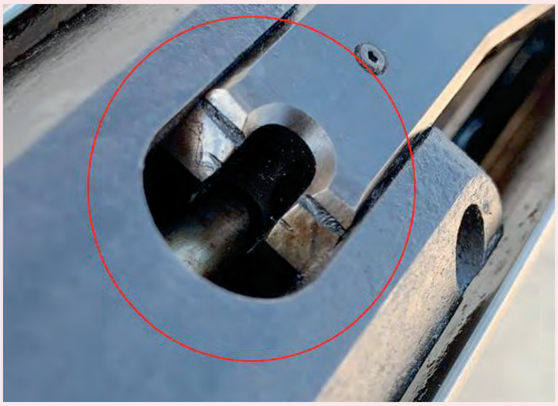

Fig. 17 *The ELG load link showed clear indication of wear from repeated cycling.*

the casing, steps were taken to ensure initial activation of the tractor occurred in the open hole section. During another run, the tractor did not sequence correctly and the tractor stopped working. After POOH and disassembly, the spring in the valve responsible for the tractor sequencing was found to be broken.

Tractor Upgrades after Second Trial

Main Valve Spring: A design modification was implemented to reduce stress in the main valve spring.

ELG Load Link: The variable performance of the gripper assembly during the first and second field trials is under review and ongoing development. The modifications to the material properties and interface geometry are being evaluated and until future improvements are implemented, use of the tractor in casing will be temporarily avoided.

Field Deployments 1 and 2: Logging Operation and Results

The main objective of the multiphase logging was to establish the flow profile and detect any water entry intervals across the 6⅛" open hole section. The horizontal section for the first deployment is nearly 7,000 ft, with 87% of the open hole covered during the logging.

To optimize the operation, logging passes are kept to the minimum with the survey consisting of one down and one up pass for both shut-in and flowing conditions, and eight station stops selected at critical points along the open hole. The upper three spinners performed well during the logging. The lower two spinners experienced a degree of sticking, all other sensors and calipers returned good data.

The downhole flow profile was successfully captured and classified as uniform since the majority of the open hole is contributing to the total oil flow. During the second deployment, the same procedure was followed as in the first, although 100% of the open hole was covered, it took several runs to capture the required data for the flow profile.

Major Design Modifications

After a third trial showed the SLT was not performing to expectations, a decision was taken to redesign several key components of the SLT to improve reliability and endurance. Multiple design improvements were implemented into the SLT, the major upgrades were:

1. **Piston Design:** The design of the piston was changed from a single valve to a three-valve hydraulic circuit. The single valve combined the function of three valves into a single valve. Excessive leakage in the single valve may lead to a valve sequencing problem. The three-valve piston splits the hydraulic circuit into a main valve and two pilot sequence valves. The three-valve piston hydraulic logic is currently used in the SLT and other tractor models. The three-valve piston has a larger through bore capable of passing a 6 mm cable.

2. **Exhaust Relief Valve:** An exhaust relief valve was added to the tractor exhaust. The purpose of the exhaust relief valve is to maintain a minimum of 300 psi in the hydraulic system while the tractor is operating. It was theorized, then empirically verified, that at slow speeds the pressure in the gripper drops below its operational range. Low gripper pressure degrades the gripper's radial force. Adding a 300 psi relief valve to the exhaust ensures there is sufficient pressure for the gripper regardless of tractor speed.

3. **Vent Port:** A vent port in the ELG pressure reducing valve connector was welded closed. Eliminating the vent ensures the ELG has sufficient supply pressure.

4. **Thrust Bearing:** A thrust bearing was added to the SG to allow the link assembly to rotate more freely. If the load link is oriented facing downwards upon activation, it can more easily rotate to its functional position and grip the wellbore.

Testing of the load link fixture proved that the ELG must have sufficient pressure to provide radial force for the load link to get an initial grip. Testing prior to adding the exhaust relief valve showed a condition when the ELG pressure could drop below its operating pressure, compromising the ELG radial force. Adding the exhaust relief valve solved this problem and ensures that there is always sufficient pressure for the ELG.

Analyzing the various pressure trace graphs shows that the three-valve piston and exhaust relief valve design modifications improved the function of the tractor. The SLT load link is capable of gripping formations with lower compressive strength and hardness than L80 casing, if the formation can maintain structural integrity. In softer formations, the SLT load link will also work at a range of angles lower than it was initially designed for. The improvements were systematically tested and modified to optimize the SLT's performance and reliability. Once a final configuration of the SLT was completed, the tractor was endurance tested in a flow loop for 3,000 ft at high loads of over 2,000 lb.

The most recent field deployment is in progress. The performance of the SLT has been excellent, pulling the CT to a target depth of nearly 21,000 ft, with a horizontal lateral section of over 10,000 ft, providing strong assurance that the latest upgrades have significantly enhanced the SLT's performance.

Conclusions

Logging in ERWs is a complex and expensive undertaking, however, given its relative importance to understanding reservoir behavior and corresponding reservoir management, it can be easily justified. To have the greatest chance of success in logging these ERWs requires a multifaceted approach to successfully meet all the objectives. One of the biggest remaining challenges has been to effectively get the CT to increase the reach or coverage using newly developed tractor technologies.

The SLT is a critical new technology that now allows a larger section of the open hole to be logged and introduces the possibility to log ever longer ERWs that were previously out of range. The field trials to date have proven the viability of the technology to significantly increase coverage of the open hole laterals during logging operations. Continued innovation and upgrades are critical to achieve more consistent reliable performances and also to continually push the boundaries in logging the toughest ERWs.

References

1. Beheiri, F.I., Al-Mubairik, A.J., Al-Mulhim, A.K. and Al-Meshal, F.M.: "Optimization of Coiled Tubing Interventions on Extended Reach Open Hole Completion in a Field in Saudi Arabia," SPE paper 116845, presented at the Russia Oil and Gas Technical Conference and Exhibition, Moscow, Russia, October 28-30, 2008.

2. Duthie, L.S., Saiood, H.A., Al-Anizi, A.A. and AlGhamdi, T.A.: "A Comparative Review of Production Logging Techniques in Open Hole Extended Reach Wells," SPE paper 202298, presented at the Asia Pacific Oil and Gas Conference and Exhibition, Virtual, November 17-19, 2020.

About the Authors

Laurie S. Duthie

M.S. in Petroleum Engineering, University of New South Wales

Laurie S. Duthie joined Saudi Aramco in 2011 as a Petroleum Engineer and works in the Manifa Production Engineering Unit of the Northern Area Production Engineering Department. His focus is on the development and production of a large offshore field in the Northern Area.

Laurie started his career in 1986 working on offshore installations in the U.K. North Sea as a Field Engineer in well testing and wireline operations. He has a strong background in reservoir surveillance, well intervention, acid stimulation, well testing, completions, and cased hole logging. Laurie has gained extensive operational experience in diverse remote onshore and offshore locations — across Africa, Central Asia, the former Soviet Union, Asia Pacific, and in the Middle East region — since 2009.

In 2005, Laurie received his M.S. degree in Petroleum Engineering from the University of New South Wales, Sydney, Australia.

Hussain A. Al-Saiood

B.S. in Petroleum Engineering, University of Oklahoma

Hussain A. Al-Saiood is a Production Engineer working in the Manifa Production Engineering Division of Saudi Aramco's Northern Area Production Engineering and Well Services Department. He joined Saudi Aramco as a Petroleum Engineer, but has also held several drilling and reservoir engineering positions, covering several onshore and offshore fields. Hussain's areas of interest include rigless intervention with coiled tubing (CT), wireline, and hydraulic workover operations.

Throughout his career, he has worked on multiple projects, including the change out of electric submersible pumps utilizing the hydraulic workover unit, and developing downhole equipment to enhance the CT reach, i.e., CT tractors and pulsation tools, in extended reach wells for stimulation and logging applications.

Hussain received his B.S. degree in Petroleum Engineering from the University of Oklahoma, Norman, OK.

Abdulaziz A. Anizi

B.S. in Petroleum Engineering, King Saud University

Abdulaziz A. Anizi joined Saudi Aramco as a Production Engineer in 2007 and currently works in the Manifa Production Engineering Unit of Saudi Aramco's Northern Area Production Engineering Department. He has been a Production Engineer unit head for the last six years, covering three different fields in the Northern Area. Abdulaziz has gained significant experience working in these large onshore and offshore fields by leading teams to optimize production and injection performance, and overcome complex challenges.

His area of interests include advancing new completion technologies to enhance matrix acid stimulation and logging operations in extended reach wells.

Abdulaziz has been active member of the Society of Petroleum Engineers (SPE) since 2010.

He received his B.S. degree in Petroleum Engineering from King Saud University, Riyadh, Saudi Arabia.

Dr. Norman B. Moore

Ph.D. in Mechanical Engineering, University of Utah

Dr. Norman B. Moore joined WWT International Engineering Services in 1995, becoming Vice President, and providing overall technical direction to drilling and completion equipment technologies. Earlier he was Vice President of Cameron Offshore Engineering with responsibilities for developing new technology for offshore structures and special aerospace-related projects.

Bruce has authored 21 technical publications, two books, and has 83 U.S. patents granted/pending. He has been a member of the Society of Petroleum Engineers (SPE) for 28 years.

Bruce received his B.S., M.S. and his Ph.D. degrees in Mechanical Engineering, all from the University of Utah, Salt Lake City, UT. Norman's graduate research included material science, fracture mechanics, and nonlinear continuum mechanics.

Unconventional Engineering toward Efficient Geosteering and Well Placement — Logging-while-Drilling in an Oil-Based Mud Environment

Salaheldeen S. Almasmoom, Gagok I. Santoso, Naif M. Al-Rubaie, Javier O. Lagraba, David B. Stonestreet, Omar A. Al-Faraj, Ali R.Al-Belowi and Jamal S. Alomoush

Abstract /

This article presents a success story of deploying new technology to improve geosteering operations in an unconventional horizontal well. A new generation logging-while-drilling (LWD) imaging tool, which provides high-resolution resistivity and ultrasonic images in an oil-based mud (OBM) environment, was tested while drilling a long lateral section of an unconventional horizontal well. In addition to improving the geosteering operations, this tool has proven the ability to eliminate the wireline image log requirements (resistivity and ultrasonic), thereby significantly reducing rig time. The LWD bottom-hole assembly (BHA) included the following components: gamma ray (GR), density, neutron, resistivity, sonic, density imager, and the newly deployed dual imager (resistivity and ultrasonic). The dual imager component adds an additional 15-ft sub to the drilling BHA, which includes four ultrasonic sensors orthogonal to each other, and two electromagnetic sensors diametrically opposite to each other.

This new technology was deployed in an unconventional horizontal well to help geosteer the well in the intended zone, which led to an improvement in well placement, enhanced the evaluation of the lateral facies distribution, and allowed better identification of natural fractures. The dual images provided the necessary information for interpreting geological features, drilling induced features, and other sedimentological features, thereby enhancing the multistage hydraulic fracturing stimulation design. In addition, an ultrasonic caliper was acquired while drilling the curve and lateral section, providing a full coverage image of the borehole walls and cross-sectional borehole size.

The unique BHA was designed to fulfill all the directional drilling, formation evaluation, and geosteering requirements. A dynamic simulation was done to confirm the required number of stabilizers, and their respective locations within the BHA, to reduce shock and vibration, borehole tortuosity and drilling-related issues, thereby improving overall performance. Real-time drilling monitoring included torque and drag trending, back reaming practices and buckling avoidance calculations, which were implemented to support geosteering, and for providing a smooth wellbore for subsequent wireline and completion operations run in this well.

A new generation dual image OBM environment LWD tool was successfully deployed to show the multifaceted benefits of enhanced geosteering/well placement, formation evaluation, and hydraulic fracturing design in an unconventional horizontal well. Complexities in the multifunctioning nature of the BHA were strategically optimized to support all requirements without introducing any significant risk in operation.

Introduction

Designing a horizontal well in unconventional plays always comes with a challenge to adequately balance the geosteering requirements with an optimized drilling engineering design that delivers the best drilling performance while acquiring all desired data. On this specific case, one of the requirements from the technical team was to have a high-resolution resistivity image to support geosteering operation, and to interpret fractures, geological features, and events in the formation. This request should be achieved while drilling with an oil-based mud (OBM) system as the drilling fluid to overcome drilling challenges.

The logging-while-drilling (LWD) density image has its limitations in terms of geosteering due to its poor vertical resolution. It was the best available option until the recent development of a new generation LWD tool. This recent LWD development was the answer to enable acquiring both high-resolution images and supporting geosteering in an OBM environment without jeopardizing the well and logging plans.

The collar mounted sensor LWD technology, able to deliver both ultrasonic and resistivity images in real-time

Fig. 1 The new generation LWD imaging tool with the sensors' distribution[1].

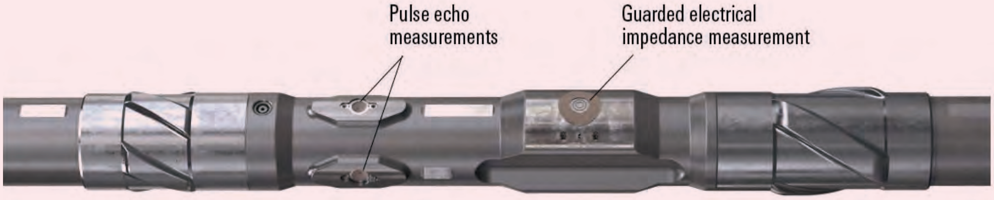

in an OBM environment, was utilized to achieve the well objectives, Fig. 1[1]. The sensors send the pulses through the drilling fluid by the electromagnetic subsystem. These pulses are sent into the formations at a wide range of frequencies to produce the resistivity images of the subsurface geological structures of the formations.

The next challenge was to acquire an acceptable image while drilling at a rate maintaining adequate drilling efficiency and hole cleaning. The functionality of the current LWD tools in the drilling bottom-hole assembly (BHA) are normally limited to certain ranges of surface collar rotation (revolutions per minute (rpm)) and rate of penetration (ROP). Because of that, the drilling performance is limited in some instances to preserve logging data quality.

The newly developed LWD dual imaging tool is designed to acquire the image logs at rates fast enough for achieving full borehole coverage at the sampling rate for both the ultrasonic and resistivity imaging sections. The tool makes both azimuthal and along the wellbore measurements. Therefore, the distance traveled along the wellbore for one full tool rotation defines the sampling rates for optimum resolution, i.e., ratio of the ROP vs. the rpm.

The optimum ROP/rpm ratio for both sensors are 2.5 ft/60 rotations and 1.5 ft/60 rotations for the resistivity and ultrasonic images, respectively. Anything at or below this ratio will provide a fully sampled image. Therefore, limitation in the drilling ROP is from the other LWD tools, not from the newly developed LWD dual imaging tool as it does not add any extra limitations to the drilling parameters.

Engineering Planning

Preparing the Wellbore

The newly developed LWD OBM dual imaging tool is designed and pilot tested prior to any field tests to acquire the ultrasonic and resistivity image log measurements for an 8½" wellbore size. This was not the typical wellbore section size used in the targeted unconventional field. Instead of testing the tool while drilling with the typical wellbore section size (8⅜"), the team elected to drill using the 8½", and overcome the challenges involved. Next, the two main challenges are discussed.

The first challenge was cleaning out the casing and related tubulars with the 8½" bit size. The well design in the targeted field has four casing strings, with the 9⅝" casing set into a low porosity limestone formation to cover loss of circulation and water-bearing zones. A 9⅝" T-95 diverter valve (DV) with a packer was installed as part of the 9⅝" casing string, and placed inside the previous 13⅜" casing. The DV is installed to be able to conduct a two-stage cement job, as the job is normally conducted with total losses of circulation.

A good cement column above the DV is critical to avoid any future pressure communication in the casing-casing annulus of the 9⅝" × 13⅜" casings from the water-bearing zone. Therefore, cleaning out the 9⅝" 53.5 lb/ft^3 DV with the 8½" size bit is not a common practice as the preference is to run a smaller size bit than the drift inside diameter (ID) of the tool. Figure 2 is a segment of the specification sheet for the 9⅝" 53.5 lb/ft^3 DV used from the service supplier indicates a recommended maximum drill out ID of 8.510". Using the 8½" bit was a unique operation because it is very close to the maximum drill out ID for the tool. The DV was drifted on the surface with an 8½" drift before making up in the casing string.

Another engineering challenge of utilizing the 8½" size bit arose, which is the internal diameter of the 9⅝" fluted mandrel hanger (FMH) of the wellhead. The ID of the 9⅝" FMH was 8.45", which will not allow the 8½" bit to pass through. The drilling engineering team considered two options, which were:

- Landing the 9⅝" casing utilizing 9⅝" manual casing slips instead of the FMH to allow a uniform profile for the bit to pass through. By switching to the manual casing slips, additional operations will be performed between the first and second stage

Fig. 2 A segment of the service provider's specification sheet of the 9⅝" DV specifying the maximum drill out ID.

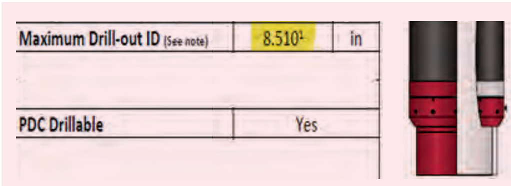

Maximum Drill-out ID (See note)	8.510[1]	in
PDC Drillable	Yes	

Fig. 3 The new generation LWD imaging tool with the sensors' distribution[1].

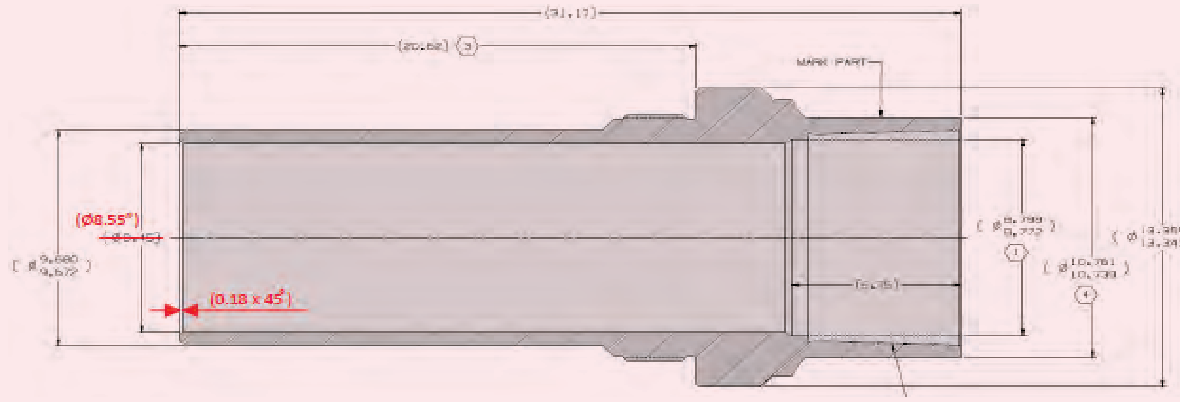

of cementing the 9⅝" casing, e.g., raising up the blowout preventer after the first stage to allow installing the manual slips, then setting it back again.

- Enlarging the ID of the 9⅝" FMH to 8.55" to allow for the bit to pass through. Figure 3 shows the modified body schematic of the FMH from the service provider. However, enlarging the FMH reduces the collapse pressure rating of the hanger body from 8,500 psi to 7,850 psi. The new collapse pressure rating of the FMH is still within the acceptable level.

Along with the service provider of the FMH, the engineering team created a scope of work to enlarge the ID of the 9⅝" FMH to 8.55". The ID of the hanger was enlarged to 8.55", then drifted with 8½" drift, and was tested to 7,850 psi successfully. Then, the 9⅝" FMH was installed in the wellhead.

BHA Design

Along with the modeling-based data correction done to the measured acquired logs, reducing the severe logging sensors' motion while drilling, by having the best drillstring stabilization, it is essential to mitigate the lateral motion effects in the logging measurements[2]. In addition, lowering the wellbore tortuosity in the wellbore will result in lower downhole dynamics, such as the stick-slip. Lowering the changes in dogleg severity (DLS) while drilling a directional wellbore will result in having a smoother lateral profile, and therefore, lower wellbore tortuosity[3].

The planned lateral drilling BHA includes a gamma ray (GR) tool, a density and neutron LWD tool, a resistivity and sonic LWD tool, a LWD neutron/density imager tool, and the new LWD OBM dual imager technology to measure ultrasonic and resistivity image logs. The addition of the newly developed tool adds three main challenges:

1. The tool's addition adds an approximately 15-ft sub to the normal LWD BHA run. The total length of the BHA becomes approximately 505 ft.
2. The tool's addition adds two more stabilizers to the planned drilling BHA. Therefore, the drilling BHA will have six stabilizers, compared to four stabilizers in the normal LWD BHA typically run in the field.
3. The placement of the tool in the planned drilling BHA is to preserve both the quality of the recorded logs, and the real-time transmission throughout the run.

The rotary steerable system (RSS) chosen to drill the lateral section is the push-the-bit steering system instead of the point-the-bit system. The push-the-bit mechanism works by applying force against the wall of the wellbore, where the bit is pushed to the other side to change the direction of the wellbore[1]. The goal of choosing the push-the-bit RSS mechanism is to enhance trajectory control, which in turn generates a smoother well profile. A smoother profile means lower downhole dynamics while drilling, as higher downhole dynamics while drilling jeopardize the functionality of the logging tools and/or the quality recorded logs. Another advantage is that the push-the-bit RSS is shorter when compared to point-the-bit system by approximately 5 ft to 7 ft, which brings the logging measurements closer to the bit.

The drilling engineering team ran several drilling BHA designs. These designs are simulated for mainly torque and drag, axial displacement, and stick-slip magnitude to select the best engineered drilling LWD BHA design. Figure 4 is the selected drilling LWD BHA design configuration.

Next, some the findings on why this configuration was selected is discussed.

Stabilization: The best stabilizer distribution in the drilling BHA is determined to be in the 10-30-35-95-115-130 order in "feet above bit" increments, having the lowest axial displacement, and smoother lateral profile. Figure 5 shows the results of the simulation of the expected hook loads and axial displacement of the BHA while drilling and tripping. The first three

Fig. 4 The LWD BHA configuration, including the new LWD OBM dual imager, while drilling with OBM in the wellbore.

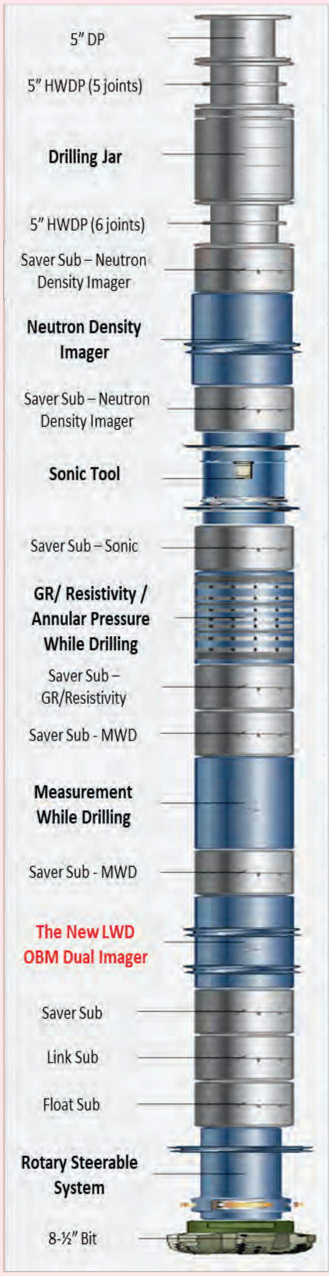

	Desc.	OD (in) / ID (in)	Max OD (in)	Bot Type / Top Type	Bot Gender / Top Gender	Length (ft)	Cum. Length (ft)
1	8 1/2" PDC Bit (6X15 nozzles)	5.750 / 2.250	8.500	/ 4-1/2 REG	/ Pin	0.8	0.8
2	**Rotaty Steerable System (RSS)**	6.750 / 5.160	**8.375**	4-1/2 REG / 4-1/2 IF	Box / Box	14.0	14.7
3	Float Sub	6.810 / 2.875	6.810	NC50 / NC50	Pin / Box	3.0	17.7
4	Link Sub for RSS	6.875 / 2.250	7.438	4-1/2 IF / 5-1/2 FH	Pin / Box	7.3	25.0
5	Saver Sub	6.750 / 3.250	6.750	5-1/2 FH / 5-1/2 FH	Pin / Pin	1.2	26.2
6	**New LWD Dual Imager Tool**	6.750 / 2.000	**8.375**	5-1/2 FH / 5-1/2 FH	Box / Box	15.1	41.3
7	Saver Sub for MWD Tool	6.890 / 3.250	6.890	5-1/2 FH / 5-1/2 FH	Pin / Pin	1.2	42.5
8	**Measurement While Drilling (MWD) Tool**	6.890 / 5.109	6.890	5-1/2 FH / 5-1/2 FH	Box / Box	24.9	67.5
9	Saver Sub for MWD Tool	6.770 / 3.875	6.770	5-1/2 FH / 5-1/2 FH	Pin / Box	1.5	68.9
10	Saver Sub for GR/Resistivity Tool	6.890 / 3.188	6.890	5-1/2 FH / 5-1/2 FH	Pin / Box	1.2	70.1
11	**Gamma Ray (GR)/Resistivity / Annular Pressure while Drilling**	6.750 / 2.810	7.500	5-1/2 FH / 5-1/2 FH	Pin / Box	17.9	88.1
12	Saver Sub for Sonic Tool	6.930 / 3.875	6.930	5-1/2 FH / 5-1/2 FH	Pin / Pin	1.2	89.3
13	**Sonic Tool**	6.960 / 5.157	**8.250**	5-1/2 FH / 5-1/2 FH	Box / Box	31.6	120.9
14	Saver Sub for Neutron Density Imager	6.900 / 3.875	6.900	5-1/2 FH / 5-1/2 FH	Pin / Pin	1.2	122.1
15	**Neutron Density Imager Tool**	6.900 / 2.250	**8.250**	5-1/2 FH / 5-1/2 FH	Box / Box	17.2	139.3
16	Saver Sub for Neutron Density Imager	6.790 / 3.250	6.790	5-1/2 FH / NC50	Pin / Box	2.1	141.4
17	6 x 5" HWDP (6 joints)	5.000 / 3.000	6.500	NC50 / NC50	Pin / Box	184.0	325.4
18	Hydraulic Jar	6.500 / 2.250	6.500	NC50 / NC50	Pin / Box	29.1	354.5
19	5 x 5" HWDP (5 joints)	5.000 / 3.000	6.500	NC50 / NC50	Pin / Box	150.9	505.4
20	5" DP	4.855 / 4.276	6.625	NC50 / NC50	Pin / Box	To surface	

stabilizers are ⅛" undergauged, while the remaining three are ¼" undergauged.

Table 1 shows the exact placement, and the exact outer diameter sizes of the stabilizers in the drilling BHA.

The New Developed Tool Placement: The typical LWD drilling BHA design run in the unconventional field has the sonic LWD tool placed directly above the RSS tool. In this BHA design, which includes the new LWD OBM dual image tool, the configuration is different. The newly developed tool is placed directly above the RSS instead, Fig. 4.

This modified arrangement places the measurement-while-drilling (MWD) and the rest of the LWD tools above the newly developed tool, which can be considered as a separate segment. By having this placement, the real-time transmissions of the MWD, and the density image logs to the surface will not be jeopardized in case of a failure in the new LWD OBM dual imager to transmit the data in real-time. Geosteering and properly placing the well can continue even if the new LWD OBM dual imager fails.

Drilling Parameters: The goal is to determine the

Fig. 5 Simulated tripping in and out of the wellbore hook loads of the BHA vs. measured depth for each estimated open hole and cased hole friction factors (left), and the simulated axial displacement of the BHA while drilling in vs. measured depth (right).

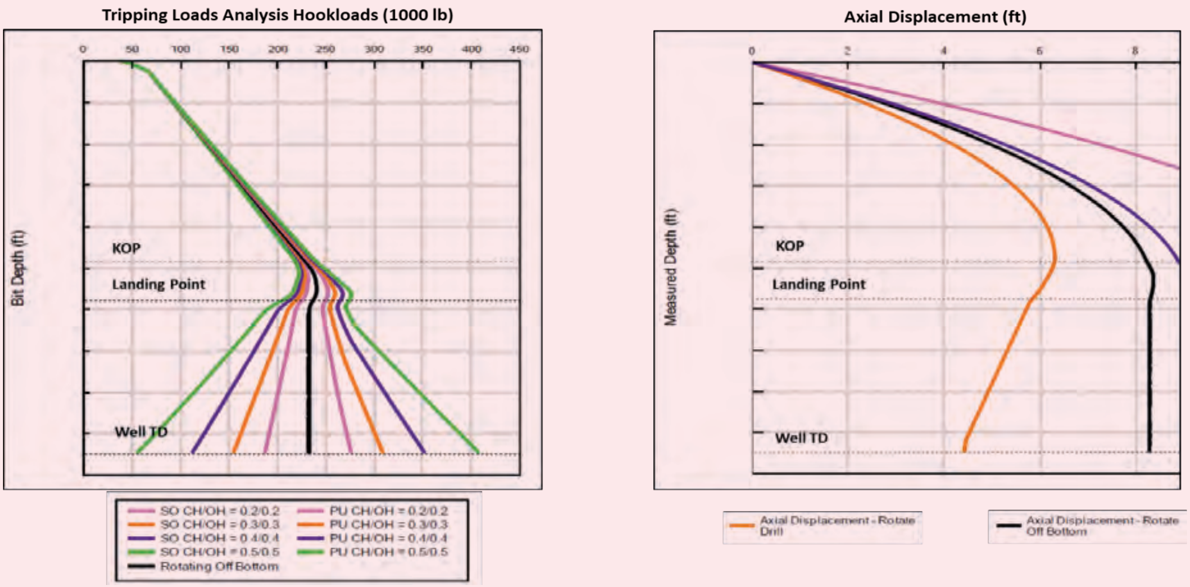

Table 1 Stabilizers, blades, ODs, length, and position in the wellbore, relative to the bit depth.

Stabilizer Summary		
Blade mid-point to Bit (ft)	Blade OD (in)	Blade Length (ft)
11.290	8.375	0.700
29.200	8.375	1.700
35.200	8.375	1.700
94.810	8.250	0.515
115.790	8.250	0.515
128.970	8.250	2.500

maximum weight on bit (WOB) and surface rotary rpm to be applied to avoid buckling the drillstring. The hydraulic jar in the BHA will be under compression while drilling the lateral section. Starting with WOB limitation, the transition zone between compression and tension while applying the maximum expected WOB is located in the drillpipe area, which is way above the jar depth. Having the jar in the transition zone causes fatigue to the tool.

Figure 6 shows the simulation of the buckling modes of the BHA while drilling the lateral section, in accordance with the WOB applied. From that, the BHA will be under sinusoidal buckling if the WOB of 35,300 lb is applied while drilling. Therefore, the WOB limitation is set at 35,000 lb.

Next, the surface rotary rpm depends on the maximum temperature generated at the RSS tool due to friction with the wellbore walls while drilling. The maximum surface rotary is set at 190 rpm — the maximum for the top drive system at the rig. While drilling through the lateral section, the RSS tool temperature will be monitored. When getting closer to the maximum temperature of the RSS tool, the temperature will be controlled by lowering the surface rotary by 10 rpm increments.

LWD OBM Dual Imaging Tool Planner

To ensure that all combined engineering design parameters fit the new LWD OBM dual imaging tool requirements, the tool planner is utilized. The general input parameters are borehole temperature, mud properties, formation resistivity, drilling ROP, surface rotary rpm, expected maximum inclination, expected azimuth, and estimated gas saturation. The more specific parameters that normally require adjustments to be entered in the tool planner are the real-time telemetry and MWD frame (which enables both resistivity and ultrasonic images to be transmitted in real-time), the ROP/rpm ratio, Fig. 7, and the estimated pumping hours during tool rotation. The results of the entered parameters will determine if both image sensors will provide the full coverage required or not. Based on this criteria, the parameters can be adjusted as required.

The output of the tool planner shows that the resistivity image sensor has a wide frequency range of measurement, which exceeds 1 MHz to 100 MHz. In this case, no adjustments to the entered parameters are required. On the other hand, the ultrasonic sensor is very sensitive to the wellbore shape and the ROP/rpm

Fig. 6 *Sinusoidal and helical buckling margins relative to the WOB applied. Sinusoidal buckling of the drillstring is expected to occur at 35.5 Klb, and helical buckling of the drillstring is expected to occur at 40 Klb.*

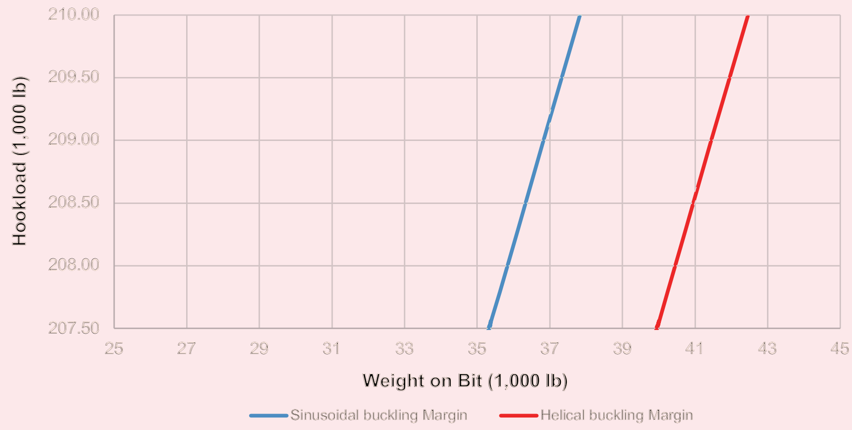

Fig. 7 *The tool planner input for the drilling parameter needs to be adjusted within the tool coverage area. The ROP/rpm ratio has to be less than 2.5 for resistivity images (left), and less than 1.5 for ultrasonic images (right), to ensure full functionality and coverage of both image sensors.*

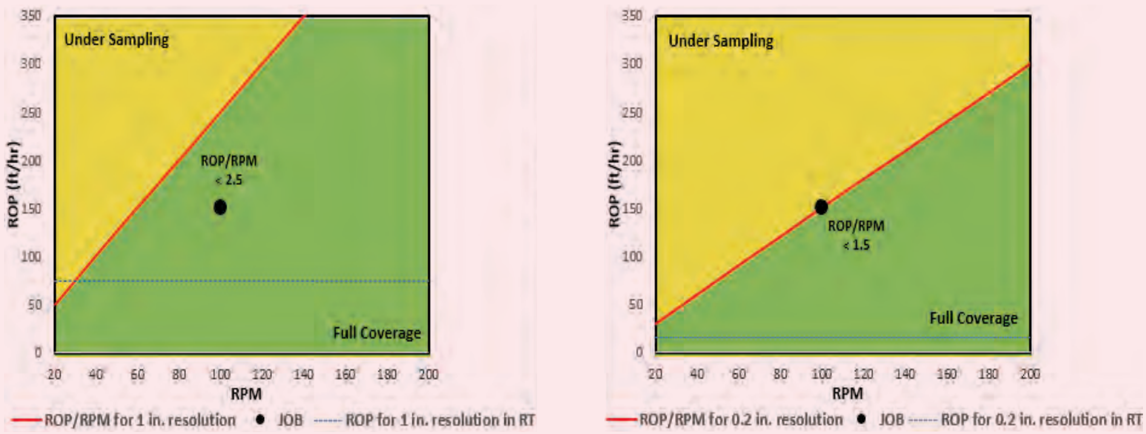

ratio. The expected size of the memory of the sensors to be set prior to drilling is also critical, compared to the recorded rate. It has to be correlated with the expected time spent to reach the total depth (TD) of the well.

Well Execution

The 8½" Hole Section Drilling Summary

The 9⅝" casing DV and shoetrack was cleaned out with the 8½" bit on clean out of the BHA with the water-based mud (WBM) used to drill the previous section (70 pcf sodium chloride polymer mud). The formation integrity below the 9⅝" casing shoe was tested with 115 pcf equivalent mud weight. The drilling fluid system in the well was converted to 84 pcf OBM. Then, both the 8½" vertical and curve sections were drilled with one directional drilling BHA containing the RSS, MWD, and GR source, starting with 84 pcf OBM. The well was landed with 96 pcf mud weight and 89.8° inclination. The highest DLS in the curve section was 5.96°/100 ft. Then, this BHA is tripped out of the hole to allow to make up and run the LWD BHA in Fig. 4 containing the new LWD dual OBM imager tool to drill, log, and geosteer through the lateral section of the well.

While running freely in the open hole with the LWD BHA, the drag on the BHA increased above 30,000 lb at the beginning of the curve section, not allowing the BHA to be freely run further. This was contributed to the high stiffness of the BHA, having an abnormally high number of six stabilizers. To be able to continue running in hole, the wellbore has to be reamed down. The speed of the reaming down was limited due to the limited surface rotary speed permitted to be used. The entire curve section was reamed down with the maximum service rotation allowed by the new LWD OBM dual imager, which is 50 rpm.

Drilling the 8½" lateral section of the well commenced with 96 lb/ft^3 OBM while limiting the drilling speed (instantaneous ROP) of a maximum of 150 ft/hr, which is the maximum recommended logging speed for the full coverage of the rest of the LWD tools in the BHA, not the newly developed tool. The hole was swept after drilling four connections with tandem pills — low viscosity pill followed by high weighted pill. Those tandem pills are pumped after making the connections. After drilling each ±92 ft stand down, the recommended followed practice was to wash up one ±30 ft joint, then ream down that same ±30 ft joint at 50 rpm.

Drilling continued through the lateral section with 96 lb/ft^3 to 98 lb/ft^3 OBM. The pickup hook load trend was increasing higher than the expected trend at the first section of the lateral with an estimated open hole friction factor of 0.5. The hole needed better connection practice to clean the hole better. Confirming this, two severe tight hole incidents occurred while drilling in the lateral section. The practice was then modified to ream up one ±30 ft joint with 100 rpm, and then ream down the same 30 ft with 50 rpm before making a connection.

The pickup hook load trend improved slightly, but was still higher than the expected trend. After that, the connection practice was modified further to ream up and down the full ±92 ft stand before making the next connection. The hole cleaning improved by showing an improved pickup hook load trend. Drilling continued to the well's TD without issues. Figure 8 shows the actual pickup weight trends while drilling.

To avoid excessive building of the filter cake on the walls of the lateral wellbore, the low gravity solids were monitored to be in the range of between 7% to 10% of the drilling fluid's volume in the wellbore. Table 2 lists a summary of the drilling parameters used while drilling.

After reaching the well's TD, the wellbore was conditioned with seven bottoms up at full drilling gallons per minute. The drillstring was reciprocated while circulating by reaming up with 100 rpm then reaming down with 50 rpm. To avoid washing out the walls of the lateral section excessively with the stiff BHA downhole by having it reaming across a constant interval, one stand is racked back at the end of each incremental bottoms up.

After that, the BHA was pulled out of the lateral section all the way to the base of the curve. Two tight spots were encountered in the lateral section that required soft backreaming to clear. The full curve section was reamed up with 100 rpm to clear any cuttings beds for the upcoming runs. Two spots in the curved section required slower speed to clear out. Even in the 8½" vertical section above the kickoff point, two tight spots were encountered and required backreaming to clear. The high stiffness of the BHA with the six stabilizers was the main reason, and will need to be reviewed and simulated further for future applications.

Fig. 8 The actual drilling hook load trends while picking up, slacking off, and rotating off the bottom during connections.

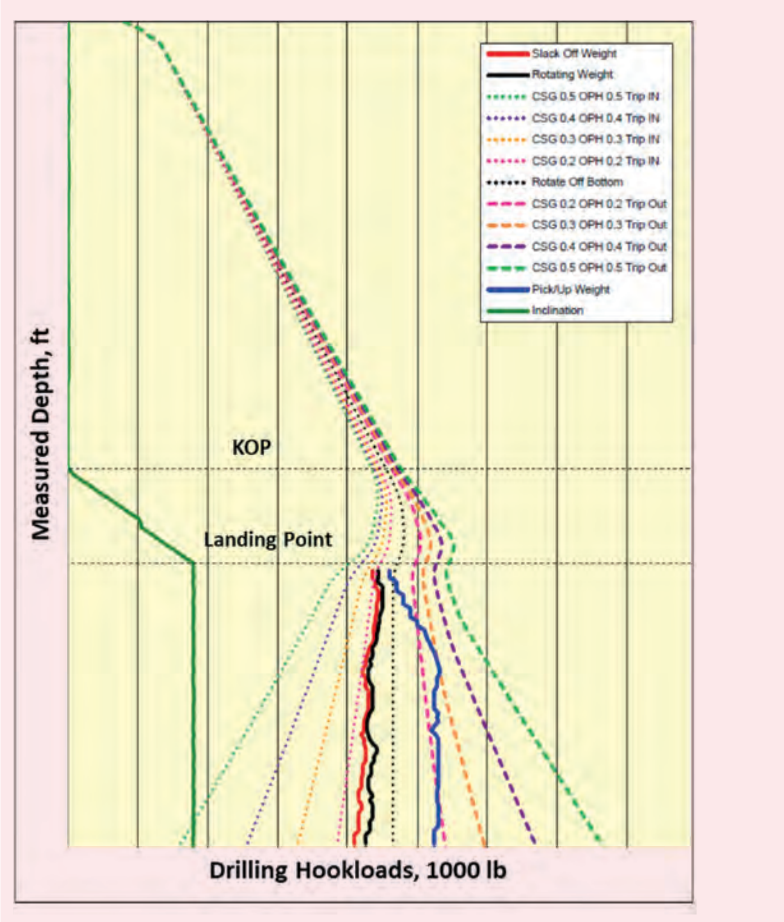

Well Placement and Geosteering

The real-time transmitted density image log is normally the tool used for well placement, along with the GR log if an OBM system is used to drill. The resistivity image log could not previously be provided due to drilling in an OBM environment. With OBM, the mud cake behaves similar to electrical insulators, which obstructs the current flow, so using the same LWD tools to acquire data in a WBM environment

Table 2 A summary of the drilling parameters.

Nozzle Size (in)	6 × 15/32
WOB (1,000 lb)	Maximum of 35 Klb to avoid sinusoidal buckling
Surface Rotary Speed (rpm)	150-90, depending on the maximum temperature on the RSS tool (302 °F)
Flow Rate (gal/min)	580-600

Fig. 9 All three image logs (the resistivity images on the left side in two different modes, the ultrasonic images in two different modes are the next two in the middle, and the density image is on the right side) were transmitted real-time together when drilling commenced. The gap in some logs are due to excessive ROP and some noise in MWD telemetry. This was done for the first time in the world.

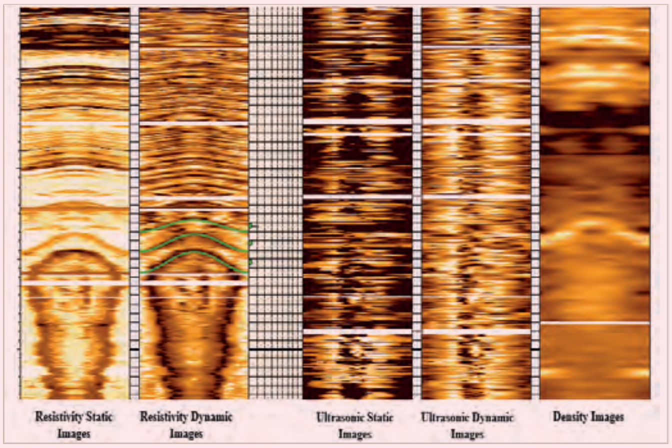

is not feasible to use in an OBM system[4]. Existing and drilling-induced fractures filled with OBM, and drilling-induced cracks filled with OBM, and mask misrepresentation of the image by scaling fewer sedimentary features[5].

The real-time density image log is a good tool to use for well placement through identifying the bedding planes while drilling through the lateral section. From the shape of the bedding layers recorded real-time, the well path can be guided to keep the bit inside the target zone. Despite that, the bedding planes shown in the resistivity image log recorded real-time from the new dual LWD imager tool shows higher resolution when compared to the density image.

Figure 9 clearly shows the better image resolution of the resistivity image compared to the density image log. For the first time ever, the real-time transmitted resistivity image was used for well placement along with the density image log.

Fig. 10 The actual well path relative to the zone of interest. The target formation is dipping down, then flattens out at end of the lateral.

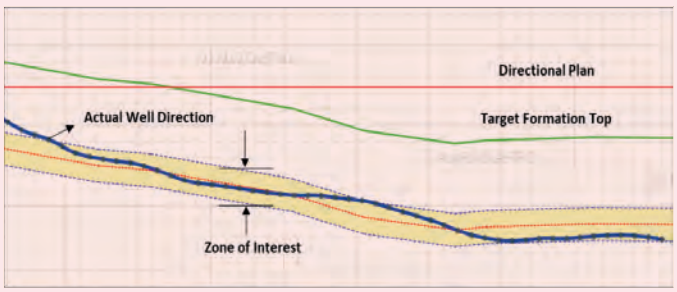

Prior to drilling the well, the expectation from the offset laterals drilled around in the offset wells was to have the target formation almost flat. Therefore, the planned directional plan was designed to maintain the well inclination after landing in the range of 89.7° to 90° while drilling through the lateral section. The resistivity image log transmitted real-time from the new dual LWD imager tool obtained while drilling through 96 lb/ft^3 to 98 lb/ft^3 OBM, combined with the density image log, helped to identify the dipping behavior of the target formation. The formation starts flat for a short interval, then it dips downward for most of the lateral section. Then, toward the end of the lateral section, the downward dripping trends are reduced until it almost flattened out, Fig. 10.

The resistivity image log helped to correct the well path back to the target zone. After drilling the first interval of the lateral section, the formation started to steeply dip down, however, formation dipping could not be easily identified from the density image log. The formation dipping plane was identified by the resistivity image log, and the well path was corrected back. Figure 10 shows that the actual well path was out of the target zone for a small portion of the lateral, then it was corrected to bring it back on target. The well path was maintained inside the target zone throughout most of the lateral section of the well by using the real-time resistivity image log.

Drilling Challenges

Tight Holes While Making Connections: Two severe tight holes were encountered while washing up a 30 ft joint after drilling stand down prior to making a connection. The drillstring could not be rotated or moved freely. Both situations were mitigated by jarring down with torque applied on the surface. The first tight hole occurred in the first few feet of the lateral. Figure 11 shows the real-time chart of the drilling parameters. The second one occurred around the middle of the lateral.

After the first incident, the practice was changed to reaming up a 30 ft joint after drilling stand down instead of washing up. After the second incident, the practice was modified again to reaming up the full drilled stand instead of a single joint. An increasing trend is shown on both incidents in the pickup weight compared to the simulated expected pickup weight. After changing the practice to reaming up the full drilled stand, the pickup weight trend stabilized around a 0.21 open hole friction factor.

Minimizing Well Tortuosity: The down dipping behavior of the target formation while drilling through the lateral section increases the steering difficulty. Despite this, the field managed to control the well inclination between 88.4° and 90.7°, and average DLS between connections to < 1.0°/100 ft for most of the lateral, Fig. 12.

Open hole Condition after Drilling the Lateral Section: There are two main activities performed after the drilling completion in this well:

Fig. 11 The real-time chart of the drilling parameters, e.g., hook load, flow rate, surface rotary, etc., of the first severe tight hole incident. The highlighted part is where the drillstring became stalled.

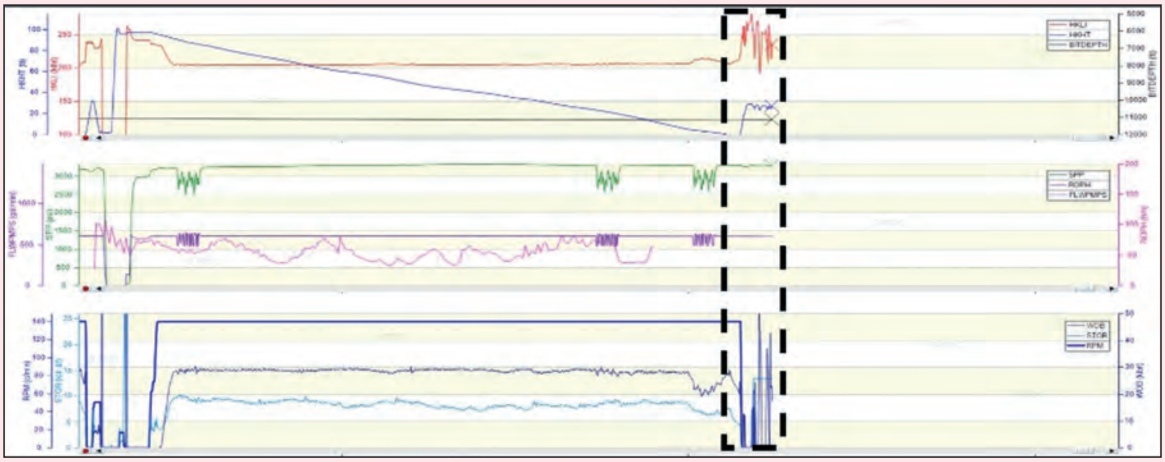

Fig. 12 The wellbore inclination (left) and average DLS (right) over the entire lateral section vs. the measured depth.

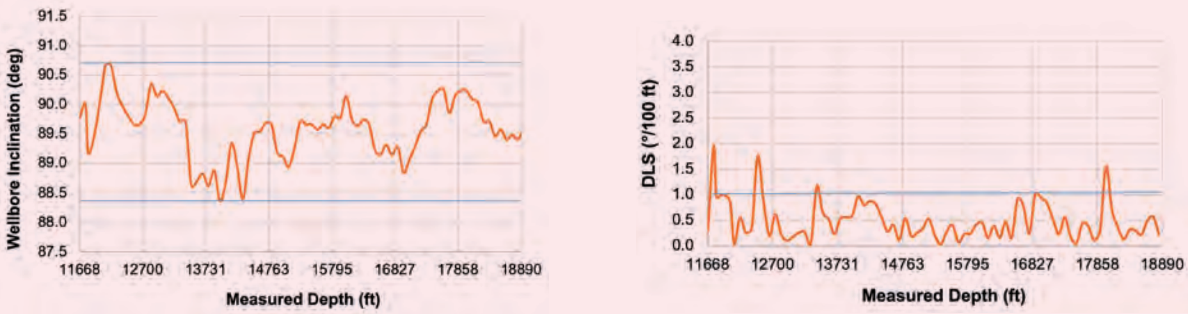

- Open hole Logging Run: The wireline equivalent tools of the ultrasonic image and resistivity image logs were run in hole on the drillpipe. The biggest OD in the logging BHA was 6½". The total length of the logging tools were around 103 ft. The tools were run to the well's TD, then pulled out in a single latch while around the middle of the curve section without any tight spots, or major excessive weight recorded on the tools.
- Running 5½" Long String Completion: To complete the well, a 5½" long string completion was run from the surface to the well's TD. The torque and drag simulations for the 5½" long string to be run through vertical, curved, then lateral section indicated that helical buckling of the long string is very likely to occur if the friction factor of the open hole is 0.2 or higher. The casing cannot be run freely anymore when it buckles, unless it is washed and/or reamed down the target depth, which adds extra time.
- Figure 13 shows the simulated tripping in hook loads with different friction factors. The simulations are done for the open hole friction factors from 0.2 to 0.4. As can be seen, the lower the open hole friction factor, the deeper the helical buckling estimated depth.

The actual tripping in hook loads of the 5½" long string completion run in this well are recorded and plotted on Fig. 13 to check the trend and estimate the buckling point. As the casing is tripped in through the curved and lateral sections, the trend of the actual hook loads showed an estimated open hole friction factor of < 0.2. The casing was run from the surface to the bottom of the well without any tight spots.

Tool Capabilities and Post-Drilling Memory Images Interpretation

Real-time Images Real-Time Transmission Capability

Since it had never been done in the world before, the technical team wanted to test the applicability of transmitting the two image logs from the new dual LWD imager tool (resistivity and ultrasonic images logs)

Fig. 13 Actual hook loads of the 5½" long string completion vs. the simulated hook loads with different open hole friction factors.

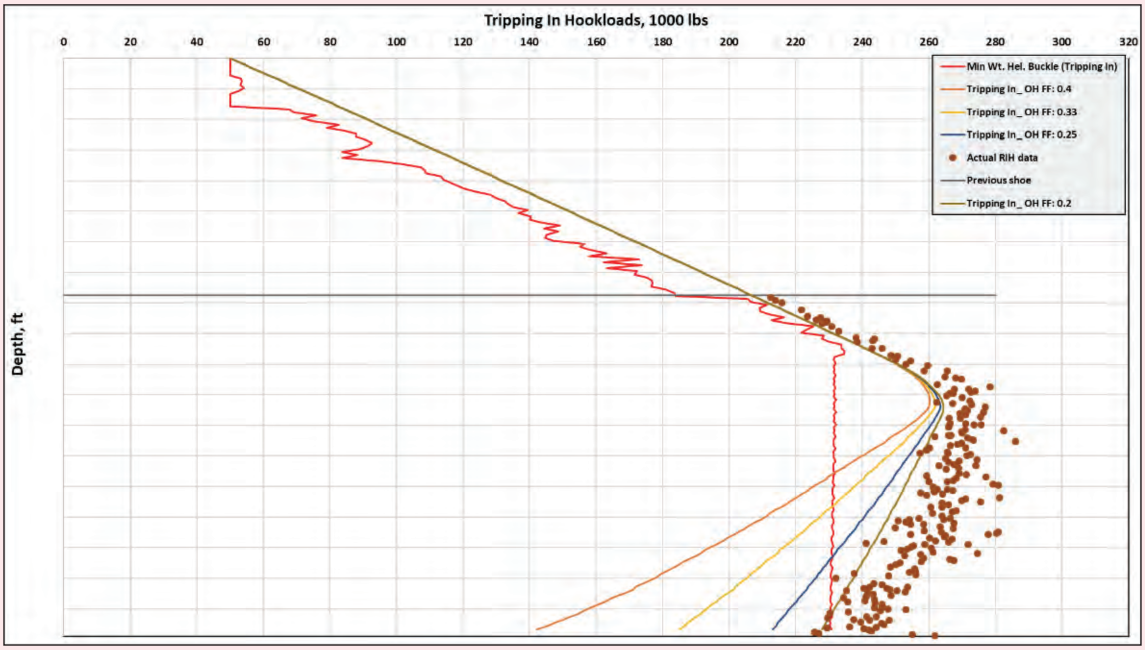

Fig. 14 The ultrasonic calipers in 2D and 3D recorded by the new LWD OBM dual imager are shown on the first logs from the left side. The logs are very comparable to the caliper logs recorded by the wireline tools (shown ion the third and fourth tracks).

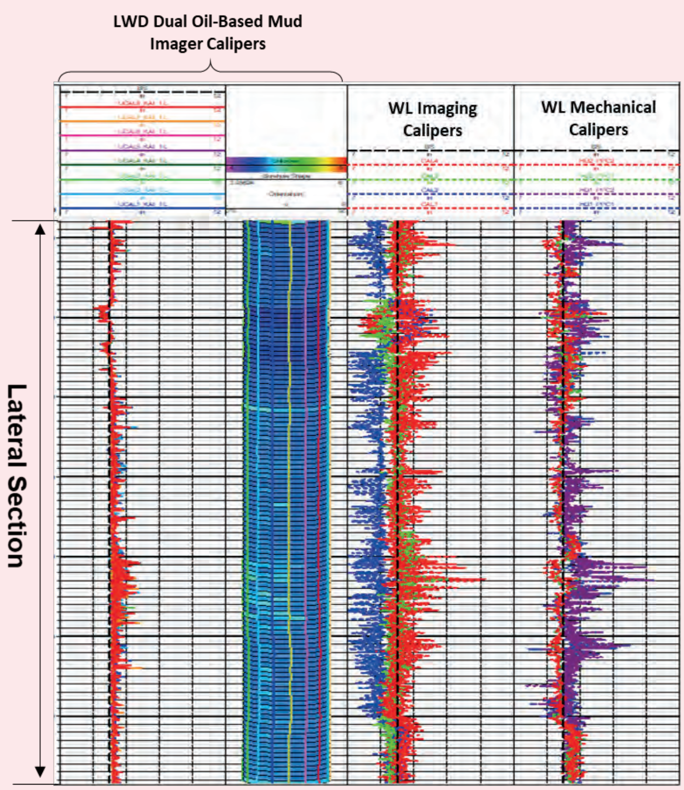

along with the density image log in real-time. For the first section of the lateral section, all the three image logs were successfully transmitted to the surface while drilling in real-time using 10 bit per second resolution.

As previously seen in Fig. 9, one can see the three image logs that were transmitted in real-time. After drilling the first few hundred feet, the quality of the real-time transmitted images degraded. The reason attributed to that was the huge amount of the transmitted data points. Therefore, to remediate the situation, the real-time transmission of the ultrasonic image log was switched off, and the image log was recorded in memory mode instead. Only the resistivity and density images were transmitted in real-time for proper well placement to maintain the well path in the target zone. The transmission of the two image logs was successful throughout the lateral section. The complete ultrasonic images log was recovered successfully at the surface.

Future studies will ensure continuous real-time transmission of the three images logs.

Ultrasonic Caliper Log Capability

In addition to the resistivity and ultrasonic images capability, the new LWD OBM dual imager is also capable of recording the ultrasonic caliper log of the drilled section. The ultrasonic caliper log was recorded while drilling the lateral section with the new LWD OBM dual imager in memory mode. It was recorded on both 2D and 3D modes. Figure 14 shows both logs. The first log plot from the left side is the ultrasonic caliper in 2D mode, and the next log is the ultrasonic caliper in 3D mode. Recording the ultrasonic caliper log while drilling was never done before. In addition, the ultrasonic caliper was recorded separately in the curve section. It was done while backreaming through the curve.

The caliper logs using wireline were obtained for the same interval and are plotted in Fig. 14 (third and fourth tracks). The ultrasonic calipers recorded by the new LWD OBM dual imager were very close to the ones recorded on the wireline.

The objective of recording the ultrasonic caliper log in this well was to test the capability of the new LWD OBM dual imager while drilling and while backreaming, in addition to recording the two images logs. The tool was successful in providing acceptable caliper data. Therefore, the calipers logs in both 2D and 3D can be recommended to be used for many future applications. For example, the data can be recorded to better estimate the cement volume for the upcoming cemented long string completions. Moreover, trouble zones while running the upcoming long string completions can be estimated using the picture provided by the ultrasonic caliper log in 3D.

The caliper sensor of this LWD imager tool is part of a drill collar. This means the position of the sensor is mainly controlled by its gravity, the drilling dynamic, and the wellbore deviation. When drilling in a long lateral, the tool is expected to be decentered, and therefore, have variable sensor standoff around the wellbore.

The effect that the standoff has on the measurement is a function of the mud properties and the contrast between the mud and formation properties. As the standoff increases, the effect is also increased. In enlarged wellbores, there is correspondingly more standoff at one side of the hole. The caliper sensor is designed to successfully acquire the caliper log in boreholes with a diameter of at least 9”. In a larger diameter wellbore, the drilling fluid has an increasing effect of reducing the apparent ultrasonic amplitude values[6].

Memory Images Interpretation

After the job was completed, the LWD data was dumped at the surface to retrieve the memory data for better data resolution visualization and interpretation. It took about 8 hours from the tool reaching above the rotary table to be able to deliver the complete data files for evaluation. A quick look interpretation was done to make sure that the tool is functioning properly, and is aligned with the real-time images data.

Figures 15 and 16 express the quick interpretation done to compare both resistivity and ultrasonic images taken from the memory data.

Images’ Vertical Resolution and Quality Assessment

LWD Images vis-à-vis Wireline Images

One of the main concerns while acquiring LWD imaging data in an OBM environment was always the vertical resolution when compared to wireline imaging tools. Until the recent deployment of the new generation of LWD tools, providing resistivity and ultrasonic images, the geosteering team had to rely only on the LWD density image.

Most of the time, the LWD density image could not be much help due to its poor vertical resolution. If the acquisition of real-time images were required to maximize the reservoir contact while drilling horizontal wells, the density image was only helpful in detecting only major bedding plane changes that in many cases were not enough to optimize well placements. If the task also included detection of natural fractures and other small-scale geological events, then the only available option was to also deploy wireline imaging tools after the section was drilled.

This additional acquisition of wireline logs

Fig. 15 *The resistivity image taken from the memory data.*

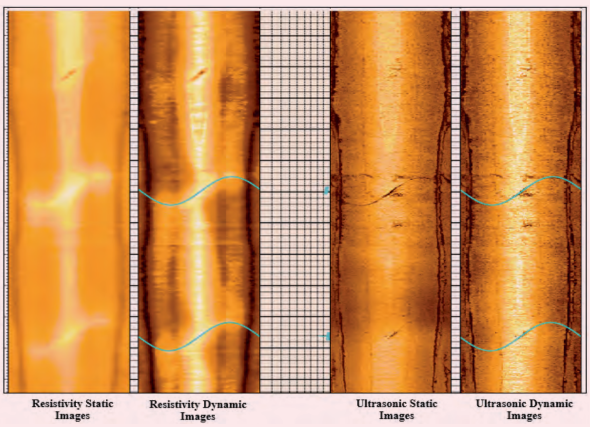

Fig. 16 *The ultrasonic image taken from the memory data.*

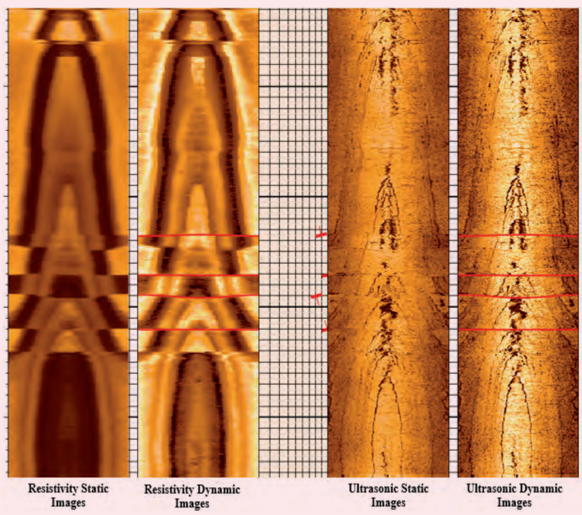

significantly increased the budget, not only of the logging program, but also of the drilling part of the project as it added additional rig time. Unfortunately, acquisition of wireline image logs in the horizontal wells does not always provide an image data with a suitable quality for the tasks they are acquired. This is due to the challenging nature of the acquisition in such an environment, e.g., hole condition, solids in mud, and so on.

The LWD oil-based resistivity and ultrasonic images acquired in this well were compared with wireline measurements and also with the LWD density images. The same comparison was conducted in two other wells (not discussed here). The results were clear; the image quality and image resolution of the LWD oil-based resistivity and ultrasonic images were excellent and permitted the users of the data to identify more geological events than with the wireline images, Figs. 17, 18, 19, and 20.

As it was described in previous sections of this article, having such high-resolution oil-based image data in real time was critical to optimize the drilling direction of this horizontal well. Several natural fractures and faults were clearly identified. Most of these events could not be observed with the wireline image logs. The value of the information with this new type of LWD imaging tool is remarkable when drilling in an oil-based environment, not only to optimize the trajectory of horizontal wells, but also as an input to optimize petrophysical evaluations and to better understand the reservoir performance.

Conclusions

The overall process summarized in this well strived to optimize the well construction operation in unconventional drilling. The engineering design and fit for purpose LWD dual imager in OBM enabled a faster delivery in completing the horizontal well. The ability to make fast decisions in real-time based on full information and borehole images has enhanced the geosteering process. The process from the pre-job stages and well engineering design toward the execution phase reflects a success story delivering such

Fig. 17 *The compressed plot over the entire curve and lateral sections of a carbonate interval. A static image with LWD (density, oil-based resistivity, and ultrasonic) and wireline (oil-based resistivity and ultrasonic) images. Note that at this compressed vertical scale dip, planes are clearly more evident on the LWD oil-based resistivity image if compared with the rest of the image logs. Also note that without the image data, the low porosity zones of this section will be considered with low flow potential, when in fact they will be the major contributors to the hydrocarbon flow due to the presence of the natural fractures (red tadpoles).*

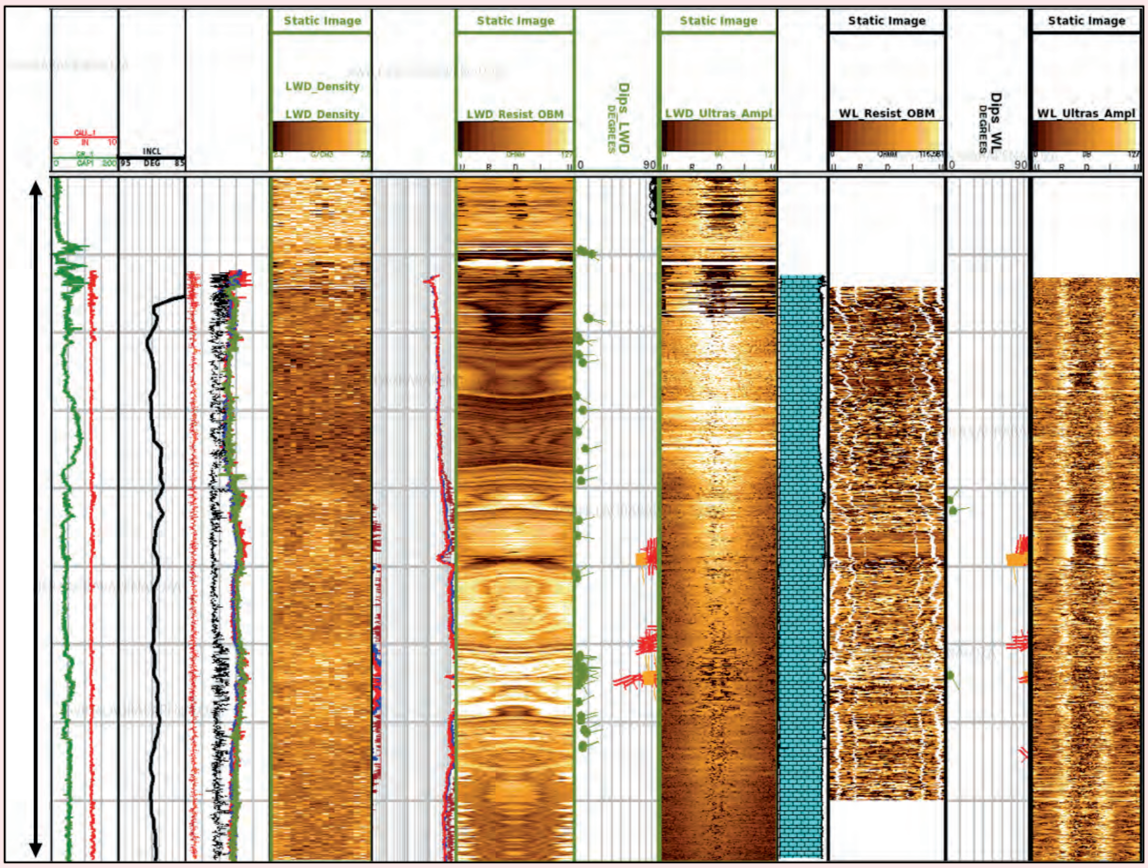

Fig. 18 (Expanded scale plot). Several bedding planes are clearly observed on the LWD OBM resistivity and ultrasonic images (note also the excellent quality of such LWD data). It is hard to observe similar bedding events on the wireline images and the LWD density image.

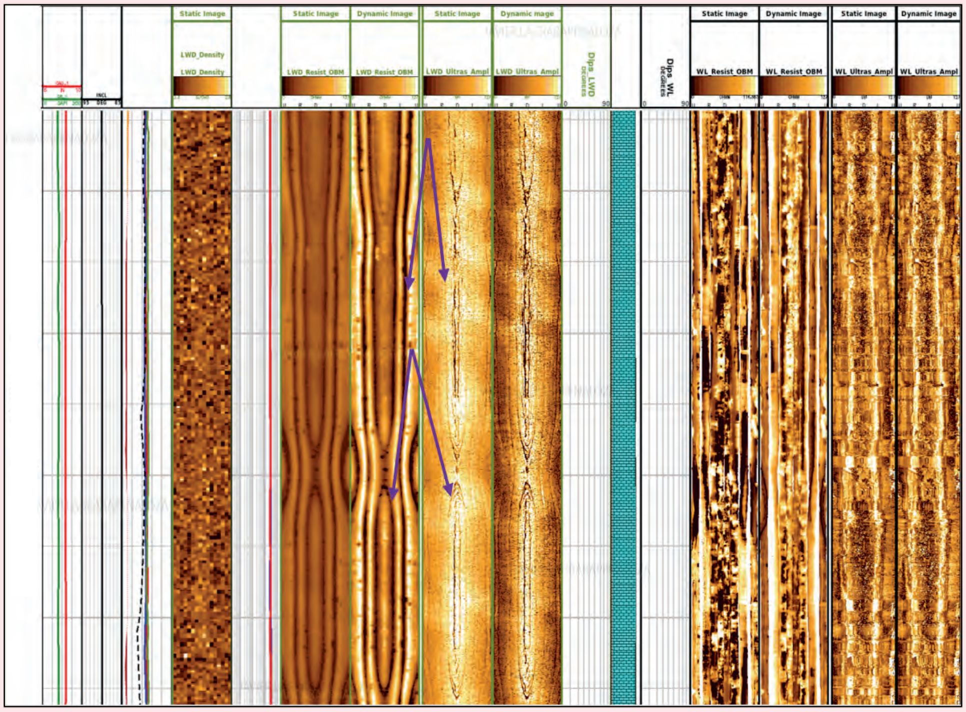

Fig. 19 (Expanded scale plot). On the LWD OBM resistivity and ultrasonic images, several micro-fault planes are clearly observed over just a short interval (orange tadpoles). Some of these events are hardly observed on the wireline images.

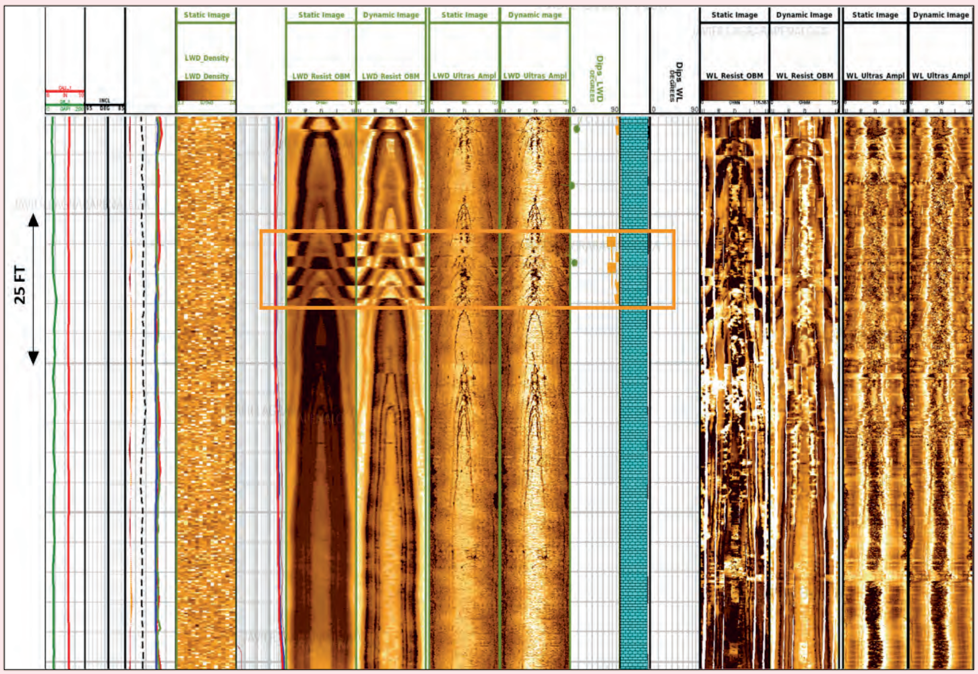

Fig. 20 *(Expanded scale plot). On the LWD OBM resistivity and ultrasonic images, several natural fractures are observed (red tadpoles). Some of these events are hardly or not observed on the wireline images.*

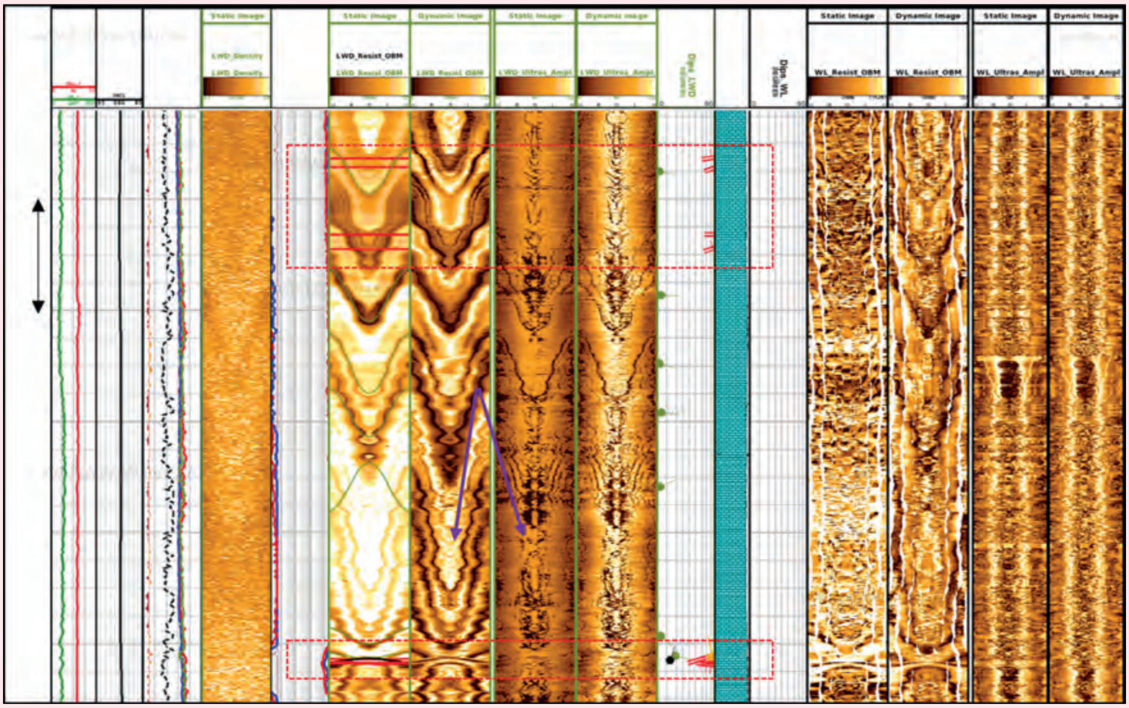

a challenging well.

The LWD oil-based (dual physics) dual imager provided resistivity and image logs that were in many sections better than the wireline resistivity and ultrasonic image logs in terms of quality and resolution. It allowed for real-time decisions to adjust the well path and thereby improve well placement.

References

1. https://www.slb.com/drilling/surface-and-downhole-logging/logging-while-drilling-services/terrasphere-high-definition-dual-imaging-while-drilling-service.

2. Haji, A., Tisdale, C., Muslem, M. and Abouzaid, A.: "Quantification and Correction of Lateral Motion Effects on NMR Logging-while-Drilling," SPE paper 203456, presented at the Abu Dhabi International Petroleum Exhibition and Conference, Abu Dhabi, UAE, November 9-12, 2020.

3. Shen, Y., Zhang, Z., Zhao, J., Chen, W., et al.: "The Origin and Mechanism of Severe Stick-Slip," SPE paper 187457, presented at the SPE Annual Technical Conference and Exhibition, San Antonio, Texas, October 9-11, 2017.

4. Laronga, R.: "Borehole Imager Provides Valuable Data in Oil-Base Muds," *Journal of Petroleum Technology*, Vol. 53, Issue 11, November 2011.

5. Bourke, L.T. and Prosser, D.J.: "An Independent Comparison of Borehole Imaging Tools and Their Geological Interpretability," paper presented at the SPWLA 51st Annual Logging Symposium, Perth, Australia, June 19-23, 2010.

6. Maeso, C.J., Legendre, E., Hori, H., Auchere, J-C., et al.: "Field Test Results of a New High-Resolution, Dual Physics, Logging-while-Drilling Imaging Tool in Oil-Base Mud," paper presented at the SPWLA 59th Annual Logging Symposium, London, U.K., June 2-6, 2018.

About the Authors

Salahaldeen S. Almasmoom

M.S. in Petroleum Engineering, University of Southern California

Salahaldeen S. Almasmoom is a Senior Drilling Engineer in Saudi Aramco's Unconventional Resource Drilling Department, designing, planning, and executing unconventional horizontal wells. He has been with the company for 10 years. Throughout his career, Salahaldeen worked as a Drilling Engineer, including in exploration and deep gas high-pressure, high temperature wells.

He is a member of the Society of Petroleum Engineers (SPE) and has contributed as an author and coauthor on several industry papers.

Salahaldeen received his B.S. degree in Petroleum Engineering from the University of Louisiana, Lafayette, Louisiana, and his M.S. degree in Petroleum Engineering from the University of Southern California, Los Angeles, CA.

Gagok I. Santoso

B.S. in Naval Architecture Engineering, Sepuluh Nopember Institute of Technology

Gagok I. Santoso is Geosteering and Reservoir Domain Champion at Schlumberger, Saudi Arabia. He has more than 21 years of experience working in Schlumberger well construction, and has held various technical and leadership positions with the company, including 15 years as a Geosteering and Reservoir Mapping Subject Matter Expert. Gagok currently provides technical support and services for Well Placement Services to Saudi Aramco.

He has worked on various projects related to drilling measurements and geosteering in Southeast Asia, China, West Africa, the Middle East, the U.S., and the North Sea.

In 1999, Gagok received his B.S. degree in Naval Architecture Engineering from the Sepuluh Nopember Institute of Technology, Surabaya, Indonesia.

Naif M. Al-Rubaie

M.S. in Petroleum Engineering, University of Texas at Austin

Naif M. Rubaie is a Lead Engineer with the Unconventional Resources Production and Facilities Development Division of Saudi Aramco's Unconventional Resources Engineering Department, where he is engaged in the planning, designing, and engineering of unconventional fields' surface facilities. Naif has 10 years of work experience at Saudi Aramco, including reservoir description and simulation, and production engineering.

Upon completion of his advanced degree, Naif joined the company's Exploration Petrophysics team and was involved in open hole and cased hole log data acquisition and analysis in exploration and unconventional wells. He has also been a team leader on the Reservoir Description and Emerging Unconventional Asset Task Force that completed a comprehensive petrophysical review of Northern, Southern, and Eastern Areas' unconventional resources.

Naif received his B.S. degree in Petroleum Engineering from the University of Leeds, Leeds, U.K., and his M.S. degree in Petroleum Engineering from the University of Texas, Austin, TX.

Javier O. Lagraba

M.S. in Petroleum Geology,
The Peoples' Friendship University of Russia

Javier O. Lagraba is a Petrophysical Technical Advisor at the Saudi Aramco Upstream Professional Development Center, overseeing the development and delivery of the petrophysical training courses and the Upstream Professional Onboarding Program. He is also the Reservoir Description and Simulation Department's Borehole Image subject matter expert working closely with the major logging service companies, testing and validating newly developed borehole imaging logging tools.

Since joining Saudi Aramco in 2009, Javier has been responsible for formation evaluation and reservoir description of carbonate and clastic gas reservoirs.

He has 24 years of experience in the oil and gas industry. Javier has previously worked as an Exploration Geologist with a Bolivian oil company, and as the Geology Domain Champion, Data Service Geology Team Leader, and Lead Petrophysicist for Schlumberger in Saudi Arabia, Malaysia, and Brazil.

He is the author and coauthor of publications for the Society of Petroleum Engineers (SPE) and the American Association of Petroleum Geologists (AAPG).

In 1994 and 1996, Javier received his B.S. and M.S. degrees, respectively, in Petroleum Geology from RUDN (The Peoples' Friendship University of Russia, Moscow).

David B. Stonestreet

B.S. in Petroleum Engineering,
University of Tulsa

David B. Stonestreet has been working as a Drilling Engineering Supervisor in Saudi Aramco's Unconventional Resource Drilling Department for the past eight years. Throughout his 35 years in the oil and gas industry, he has worked for different oil and gas operating companies with operations in Texas (onshore and offshore), New Mexico, Oman, Algeria, and Saudi Arabia, primarily supervising and managing drilling, completion, and workover operations.

In 1986, David received his B.S. degree in Petroleum Engineering from the University of Tulsa, Tulsa, OK.

Omar A. Al-Faraj

B.S. in Petroleum Engineering,
University of Tulsa

Omar A. Al-Faraj is working as a Drilling Engineering General Supervisor in Saudi Aramco's Unconventional Resource Drilling Department. He has 37 years of experience in the oil industry, spending most of his time drilling engineering and drilling operations.

Omar has led drilling teams, for both onshore and offshore exploration for the development of high-pressure, high temperature oil and gas wells, including shallow and deep-water wells in the Red Sea.

He is a senior member of the Society of Petroleum Engineers (SPE). Omar has contributed as an author and coauthor in several industry papers.

In 1985, he received his B.S. degree in Petroleum Engineering from the University of Tulsa, Tulsa, OK.

Ali R. Al-Belowi

B.S. in Petroleum Engineering,
King Saud University

Ali R. Al-Belowi joined Saudi Aramco in 1989 as a Petroleum Engineer. Currently, he is the Supervisor of the Exploration Petrophysics Unit in Saudi Aramco's Reservoir Description and Simulation Department.

In his early career, Ali spent many years with Well Testing, where he supervised the well testing operations of many exploratory wells throughout the Kingdom of Saudi Arabia. In addition, he conducted extensive and various petrophysical projects in different exploration and development areas.

Throughout his career, Ali has worked in many departments, including Drilling Engineering and Reservoir Management. Also, he has held several leadership positions in multiple organizations within Saudi Aramco.

Ali received his B.S. degree in Petroleum Engineering from King Saud University, Riyadh, Saudi Arabia.

Jamal S. Alomoush

B.S. in Earth and Environmental Sciences,
Yarmouk University

Jamal S. Alomoush is a Directional Drilling Business Development Manager at Schlumberger, supporting Saudi Aramco's Exploration and Unconventional Operations where he collaborates with drilling, petrophysics, geology, reservoir, and well placement teams to propose and deliver technical solutions that fit the needs of Saudi Aramco.

He has over 16 years of oil and gas industry experience, most of which has been based in Saudi Arabia with Schlumberger.

Jamal has also worked as a Schlumberger Surface Formation Evaluation and Drilling Optimization Engineer in various projects with Saudi Aramco.

He is an active member of the Society of Petroleum Engineers (SPE) and he has contributed as an author and coauthor on a number of industry papers.

Jamal received his B.S. degree in Earth and Environmental Sciences from Yarmouk University, Irbid, Jordan.

A Resonance-Based through Tubing Cement Evaluation Technology

Dr. Jie Li, Dr. Qinshan Yang, Jinsong Zhao, Marvin Rourke and Mohamed Larbi Zeghlache

Abstract /

Through tubing cement evaluation (TTCE) in a multistring well has been considered a cost-effective way for well integrity evaluation without removing the production tubing. Conventional acoustic cement bond logging methods are not able to operate accurately with the multistring structure due to an extremely low sensitivity and signal-to-noise ratio (SNR). Therefore, it is important to develop novel technology and an apparatus that can accurately and efficiently monitor the cement condition in the multiple pipe cased well. Applications would include use in production, injection, and storage well configurations as well as for plug and abandonment planning.

To this end, a novel TTCE technology based on a selective non-harmonic resonance (SNHR) is proposed. Unlike the traditional acoustic wave propagation method (WPM), the new tool emits continuous energy to excite the SNHR of the multistring structure, considered to be a multiple degree of the freedom Duffing system. This includes coupling of the hydraulic pressure in fluid and elastic stress-strain of solid materials. The continuous sinusoidal excitation from the SNHR tool drives the structure in a long burst mode and measures the resonance power loss due to the energy leaking through the cement layer, to represent the casing cement bond, as well as the cement formation bond condition.

The SNHR tool, therefore, has overcome the main challenge, which is the acoustic energy reflections and dissipation through multiple interfaces for existing WPMs. The SNHR tool was validated theoretically and experimentally. Results showed that the SNHR tool can reach high sensitivity (> 10%) and SNR (> 10 dB) for variable combinations of pipe sizes up to 14". This implies that the SNHR is a promising technique for evaluating cement bond integrity in the annulus of an outermost pipe string when multiple inner pipes and their associated annuli are liquid filled. In addition, the SNHR tool does not require direct coupling to the first pipe string through pads or extensions, which reduces the engineering complexity of a field worthy instrument.

Introduction

The casing cement bond is the key factor in well integrity that prevents the leakage of fluids from the well structure to the surface or to underground formations. A good cement bond is not only required for new production and storage well operations, but also is critical in plug and abandonment operations[1, 2]. Cement evaluation logs are generally used to evaluate the quality of the cement sheath behind the casing.

The traditional acoustic wave propagation methods (WPMs) emit acoustic energy to the casing annulus and record the acoustic waveforms, then the interpretation of the measurement yields an evaluation of bond between the cement and the pipe, and between the cement and the formation. To obtain a highly accurate measurement, however, the production tubing must be removed from the well, which is costly and time-consuming. It would be preferential to have a device for through tubing cement evaluation (TTCE).

The conventional cement bond logging tools based on WPM are not able to be used in TTCE due to the extremely high energy reflection (> 95%) at the inner pipe interface. Therefore, no cement bond information can be detected by the WPM-based logging tool. Although some acoustic solutions for TTCE were proposed based on conventional methodologies such as the pitch-catch[3] via analyzing a later arriving wave packet, and pulse echo[4] via analyzing multiple reflection components, their response signal from the target structure is too subtle to be reliably used in the multiple pipe well evaluation.

This confirmed that the energy of a single pulsed acoustic wave — for multiple pipe wells — will be dissipated at the inner pipe fluid interfaces, causing the received signal to be too weak to be useful in the log evaluation[5]. Currently, based on the conventional cement bond logging methods, a frequency domain analysis of the received signal was developed for TTCE[6-8]. For the frequency domain, the amplitude changes of the received signal might be observed for the change of cement bond conditions at approximately 10 kHz to 15 kHz, but the reliability of sensitivity and signal-to-noise ratio (SNR) are still uncertain.

Currently, an electromechanical impedance (EMI) based structure diagnosis technique has been utilized

Fig. 1 *The proposed SNHR tool.*

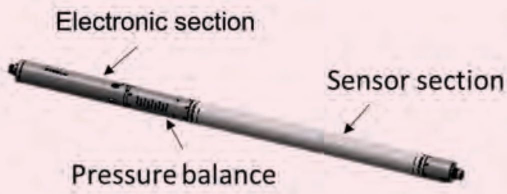

extensively in various fields, such as concrete load monitoring, crack detection in metal products, debonding detection, etc. For EMI, the lead zirconate titanate (PZT) patch is used as a transmitter and receiver simultaneously, based on the direct and converse piezoelectricity effects. When PZT patches connect to the host structure, an alternating voltage of varying frequency can be applied, and the vibrations of the PZT and the host structure are coupled.

Then, measured EMI signals can represent the impedance of the host structure and a variation can be detected in the EMI for the structural damages. The EMI method has a high sensitivity to local damages since it utilizes structure resonance frequency. In addition, the PZT patch itself is cost-effective, small, nonintrusive, and exhibits linear behavior. These characteristics make the EMI technique efficient and accurate, with the potential to provide real-time evaluation at low cost.

In this article, a TTCE technology based on a selective non-harmonic resonance (SNHR) is proposed for the first time. It is based on the impedance measurement under system resonance, to improve the sensitivity and SNR. The SNHR method utilizes EMI technology to detect the change of cement bond while the multistring system is under sympathetic vibration. Unlike traditional WPM, the new tool emits continuous energy to excite the SNHR of the multistring structure, considered to be a Duffing system with multiple degrees of freedom, which includes coupling of the hydraulic pressure in fluid, and elastic stress-strain in solid materials.

Fig. 2 *The TTCE logging system.*

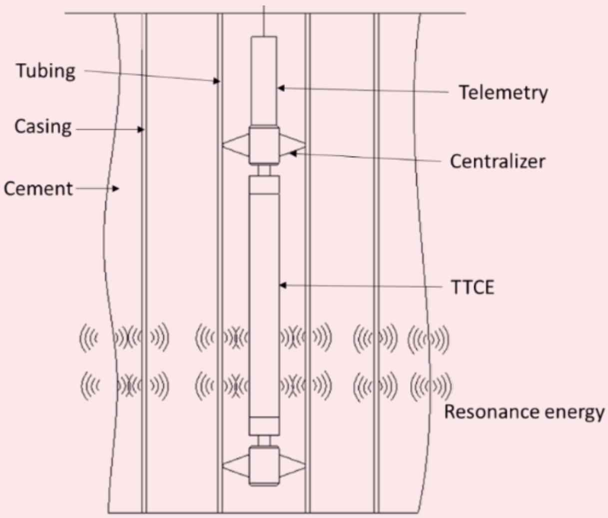

The continuous sinusoidal excitation from the SNHR tool is driving the structure in a long burst mode. The SNHR tool is measuring the resonance power loss due to the energy leak through the cement layer. This measurement is then used to represent the casing cement bond as well as the cement formation bond condition. The SNHR tool, therefore, has overcome the main challenge, which is the acoustic energy reflections and dissipation through multiple interfaces for the existing WPMs.

We first studied the feasibility of system resonance and validated the impedance-based method in downhole applications with an acoustic source and PZT-based source in the simulation. Then, the operation range, sensitivity, and SNR were validated with multiple tubing casing size combinations with the verification with experiments.

TTCE Tool Description

The proposed SNHR tool contains two modules: (1) The sensor section with PZT arrays, and (2) the electronic section with various units for power supply, excitation driver, data acquisition, data preprocessing, data communication, and tool control. The two sections are connected through the field joint, Fig. 1. For the TTCE logging operations, the complete logging system requires a surface panel, a downhole telemetry/power module, and centralizers.

During logging, the SNHR emits continued acoustic energies through a transceiver array at specific frequencies to stimulate the resonance of the entire well structure. Once the stationary resonance is achieved, TTCE starts acquiring the impedance signal, which represents the acoustic energy at the transceiver surface, which is associated with cement bond properties that indicate the cement bond condition changes due to corrosion or other defects, Fig. 2.

Simulation Validation for TTCE

To develop the SNHR tool, a double pipe well system was utilized to understand the physics and validate the performance. Figure 3a shows the double pipe well system. The system includes two pipes as tubing (inner pipe) and casing (outer pipe). The entire system was physically connected based on the solid mechanics and fluid pressure, and can transport the energy from the logging tool to all structures. To simulate the multistring well, steel pipes with 4½", 5½", 9⅝", and 14" outside diameter (OD) was used as the tubing and casing.

The cement was set to 1" thickness behind the casing, the formation was in the outset layer with a far-field boundary, and water filled in the interior and A-annulus. For the TTCE tool, the housing OD was set to 3" with a steel pipe and oil was filled inside. The casing was bonded to the formation with a cement layer in the B-annulus for good bonding and water for free pipe conditions. To validate the concept, the effect of the change of cement property on the received signal was studied first; the cement density was varied from 100% of the original value as a good bond to 70% as a bad cement bond. Table 1 summarizes the material density of each interface used for the study.

Simulations were conducted for validating the physics and feasibility of the SNHR tool. To enhance the SNR and sensitivity, the resonance principle of the well system was applied. To stimulate the resonance of the entire well structure, a low frequency acoustic wave with normal incidence was continuously generated to continuously supplement the energy that dissipated at the pipe fluid interfaces. The low frequency provides a better depth penetration and avoids pipe plate modes. The normal sound incidence with continuous wave will excite the global resonances, including the tubing, casing, and the cement[9].

The simulation included the solid mechanics applied to the logging tool, pipes, cement, and formation, and the acoustic pressure physics were applied in the fluid domains such as the interior and A-annulus. Meanwhile, the acoustic and solid mechanics were coupled in each boundary.

A mathematical pressure source was first used to understand the phenomenon when the well system is under resonance vibration. For the acoustic source, the logging tool domain was considered based on acoustic pressure and can be expressed as:

$$\nabla \cdot \left[-\frac{1}{\rho_0}\left(\nabla p(x,t)\right)\right] - \frac{\omega^2 p(x,t)}{\rho_0 c^2} = Q \tag{1}$$

where Q is (s^{-2}) is the acoustic source.

Then, a transducer source was used to verify the feasibility and possibility of impedance measurement for the TTCE. For the transducer source, the PZT ceramic was used, generating a mechanical strain under an applied electrical field as the inverse piezoelectric effect. These EM behaviors of the isotropic PZT were expressed by linearized constitutive equations as:

$$\begin{cases} T = c_E S - e^t E \\ D = eS + \varepsilon_S E \end{cases} \tag{2A}$$

$$\begin{cases} S = s_E T - d^t E \\ D = dT + \varepsilon_T E \end{cases} \tag{2B}$$

where T is the stress vector (Pa), S is the strain vector (mm^{-1}), E is the electric field intensity vector ($V\ m^{-1}$), D is the electric flux density vector ($C\ m^{-2}$), c_E is the elastic coefficient (Pa) at constant electric field strength, e_t is the transposed dielectric permittivity matrix ($C\ m^{-2}$), e is the dielectric permittivity ($C\ m^{-2}$), ε_s is the dielectric permittivity matrix ($F\ m^{-1}$) at constant mechanical strain, s_E is the elastic compliance ($m^2\ N^{-1}$) in a constant electric field, d_t is the transposed piezoelectric strain constant matrix ($m\ V^{-1}$), d is the piezoelectric strain constant ($m\ V^{-1}$), and ε_T is the dielectric permittivity matrix ($F\ m^{-1}$) at constant mechanical stress.

The vibration/pressure generated in the piezoelectric transducer/pressure source was then transmitted to the interior and transport to the formation. The sound waves in the water domain by means of the Helmholtz equation for sound pressure was calculated as:

$$\nabla \cdot \left[-\frac{1}{\rho_f}\left(\nabla p(x,t)\right)\right] - \frac{\omega^2 p(x,t)}{\rho_f c^2} = 0 \tag{3}$$

Here, the pressure is a harmonic quantity, $p(x,t)$

Fig. 3 (a) An illustration of a double pipe well system, (b) the double pipe well system simulation setup top view, and (c) the side view.

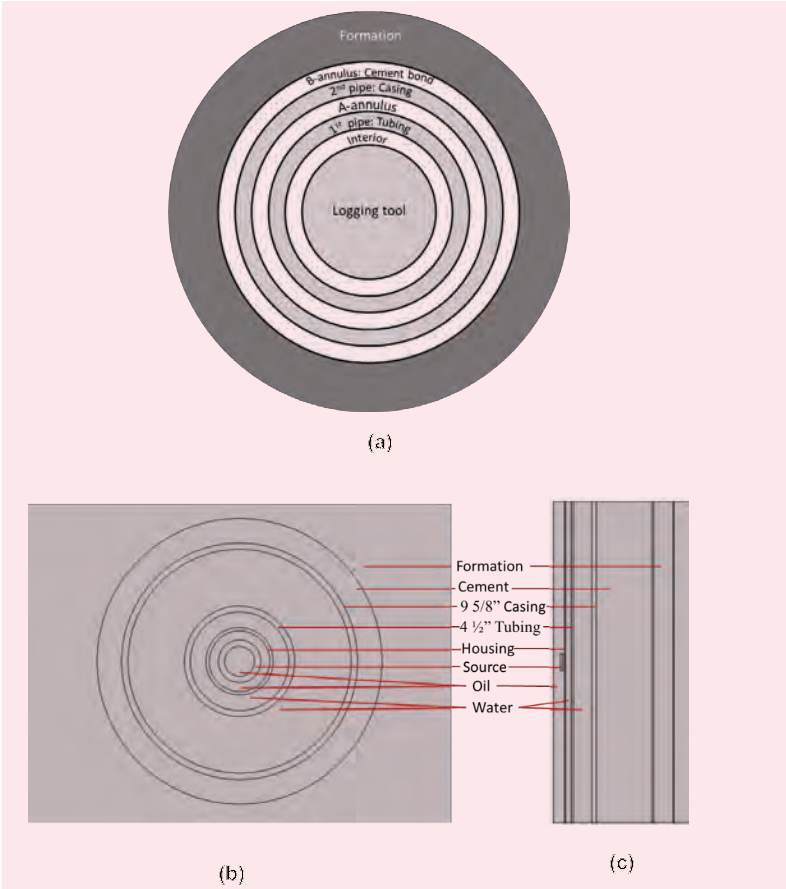

Table 1 *Material density.*

	Steel Pipe	Cement	Formation	Water	Oil
Density (kg m^3)	7,500	2,300	2,600	1,000	900

$= p(x,0)e^{i}w^{t}$, and p is the pressure (N m^{-2}), ρ_f is the density of fluid (kg m^{-3}), ω is the angular frequency (rad s^{-1}), and c is the speed of sound (m s^{-1}).

The linear elastic behavior is governed by Newton's Second Law:

$$-\rho_m \omega^2 x = \nabla \cdot S + F_V e^{i\varphi} \quad (4)$$

where ρ_m is the solid material density (kg m^{-3}), x is the particle displacement (m), F_V is the force per volume (N m^{-3}), and $e^{i}\varphi$ represents the alternating current (AC).

The boundary condition sets the boundary load, F_A (force/unit area), on the solid fluid interface as equal to the acoustic pressure:

$$F_A = p(x,t) \quad (5)$$

While on the fluid side, the normal acceleration experienced by the fluid is set equal to the normal acceleration of the solid as:

$$\frac{1}{\rho_f}\left(\nabla p(x,t)\right) = \ddot{x} \quad (6)$$

A sinusoidal input voltage (V) is applied to the PZT and the output current (I) is measured. The impedance, Z, at a specific driving frequency is defined as the ratio of V to I. A 1D analytical model of the EMI, Fig. 4, demonstrated that the EMI of the PZT structure is directly affected by the mechanical impedance of the host as:

$$Z = \frac{V}{I} = \frac{1}{i\omega C_a\left(1-k^2\left(\frac{Z_a}{Z_s-Z_a}\right)\right)} = \frac{1}{i\omega C_a(1-k^2)} + \frac{Z_s-Z_a}{i\omega C_a k^2 Z_a} \quad (7A)$$

$$Z_a = \frac{k_a(1+\eta_a i)}{\omega} \quad (7B)$$

$$Z_s = \left[M_s\omega - \frac{k_s(1+\eta_s i)}{\omega} i\right] \quad (7C)$$

where C_a is the zero-load capacitance of the PZT, k^2 is the EM coupling coefficient of the PZT and Z_a is the mechanical impedance of the PZT, Z_S is the mechanical impedance of the host structure, and i is an imaginary unit; K_a and η_a are the static stiffness and mechanical loss factor of the excitation PZT, respectively; K_S, η_S, and M_S are the static stiffness, mechanical loss factor, and mass of the structure, respectively.

Further, the multi-degree of freedom (MDOF) method was applied in the double pipe well system, Fig. 4. The double pipe well system is considered as a linear elastic system and it will contain the mass and stiffness for the housing, tubing, casing, cement, and formation[10].

The vibration equation without damping can be expressed as:

$$[M]\{\ddot{x}\} + [K]\{x\} = \{f\} \quad (8)$$

where $[M]$ is the mass matrix and $[K]$ is the stiffness matrix that containing materials properties, and $\{f\}$ is the force matrix, $\ddot{x}$ is the acceleration, and x is the displacement.

To consider the effect of the structure on the frequency, the eigenfrequency can be obtained by solving the following eigenvalue problem:

$$(\mathrm{K} - M\omega^2)\phi = 0 \quad (9)$$

where the ω denotes the eigenfrequency of the system, and ϕ is the mode shape.

Then, the relationship between resonance frequency, structure's stiffness, and mass can be obtained via solving Eqn. 8. At each mode shape, the frequency will be expressed as:

$$\omega = \sqrt{\frac{K}{M}} \quad (10)$$

Based on Eqn. 10, it should be noticed that when the cement bond changes from a good bond to a bad bond, i.e., the density changes from 100% to a lower value, the mass of the cement structure is reduced. Therefore, the resonance frequency of a good bond could shift from a higher frequency to a lower frequency. This MDOF method might be able to provide an accurate and efficient method to predict the resonance frequency that cement bonds have, as a maximum sensitivity under different well structures.

Simulation with Acoustic Source

Figures 5, 6, and 7 shows the pressure source's results for 4½" tubing with 5½" casing, for 4½" tubing with

Fig. 4 *A 1D analytical model of the EMI as an equivalent MDOF method structure for the double pipe well system.*

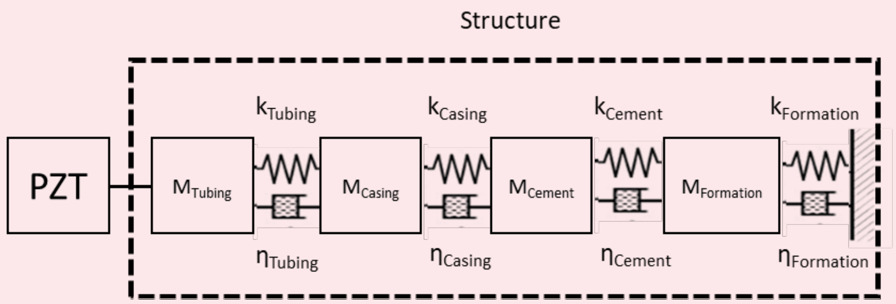

Fig. 5 *The 4½" tubing with a 5½" casing combination, (a) acoustic pressure response as a function of frequency for a good cement bond to a bad cement bond, and mode shape (b) at 15 kHz, and (c) at 20 kHz.*

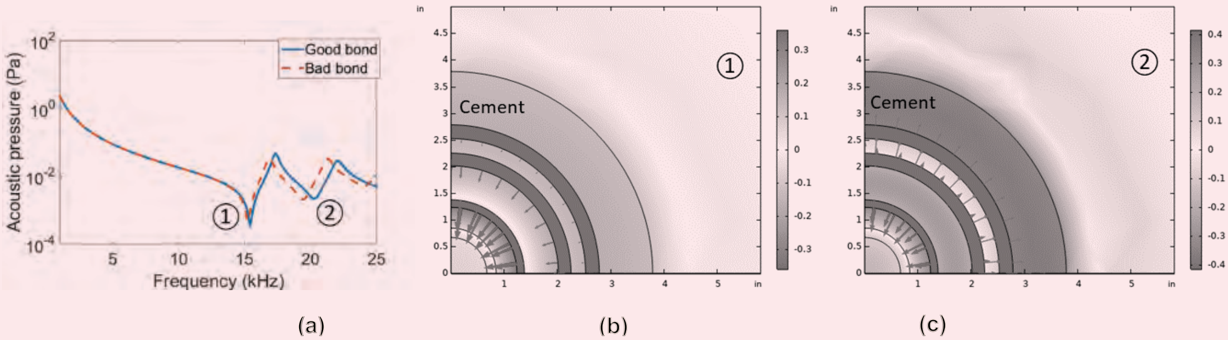

Fig. 6 *The 4½" tubing with a 9⅝" casing combination, (a) acoustic pressure response as a function of frequency for a good cement bond to a bad cement bond, and mode shape (b) at 10 kHz, (c) at 15 kHz, and (d) at 20 kHz.*

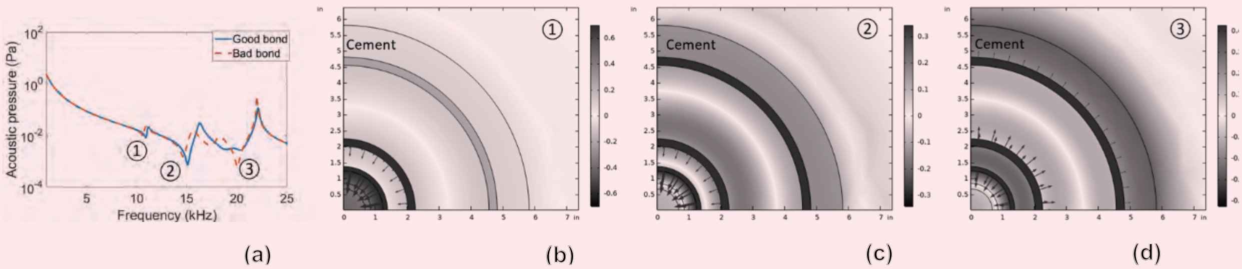

Fig. 7 *The 9⅝" tubing with a 14" casing combination, (a) acoustic pressure response as a function of frequency for a good cement bond to a bad cement bond, and mode shape (b) at 6 kHz, (c) at 10 Hz, (d) at 16 kHz, and (e) at 22 kHz.*

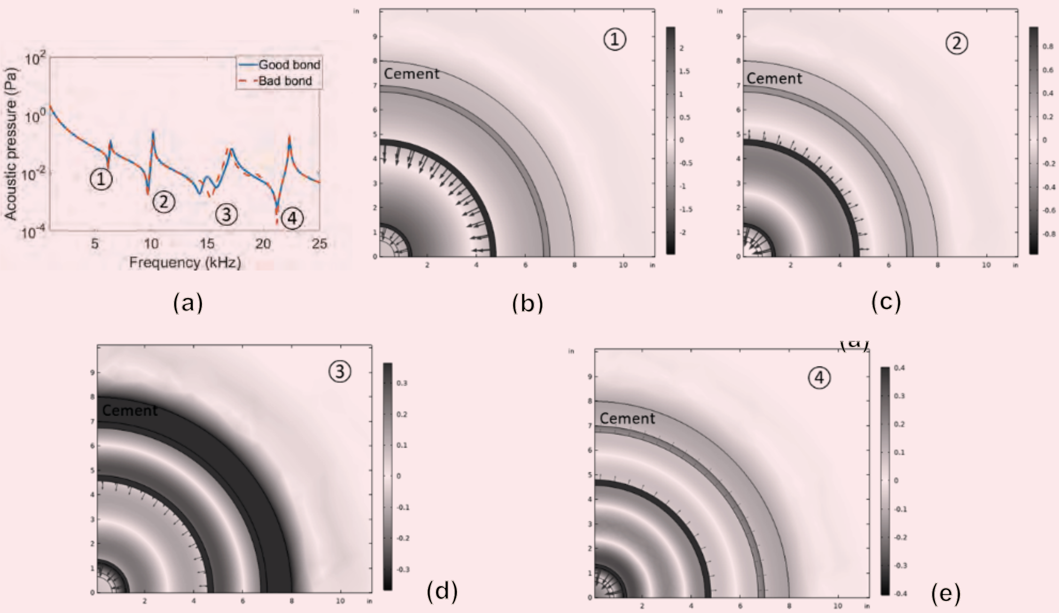

9⅝", casing and 9⅝" tubing with 14" casing, respectively. The acoustic pressure on the source's surface was recorded as a function of excitation frequency from 1 kHz to 25 kHz and cement density from a good bond to the bad bond condition. The sensitivity was then calculated based on the peak value at each resonance frequency.

For the case of the 4½" tubing with a 5½" casing, Fig. 5a, there were two resonance peaks at 15 kHz and 20 kHz. The pressure changed significantly in the range of 15 kHz to 25 kHz. The maximum change (50%) was observed at approximately 20 kHz, and other resonance frequencies also showing smaller changes (22% at 15 kHz).

The mode shape and pressure distribution are plotted in Figs. 5b and 5c for the 15 kHz and 20 kHz peaks, respectively. The deeper color identifies the higher pressure level, which indicates a more concentrated energy in that area. For the arrow representing the displacement of the pipes, a longer arrow means more displacement amplitude.

Comparing Figs. 5b and 5c, the color in the casing cement area at 20 kHz (0.4 Pa) was much deeper than at 15 kHz (0.1 Pa), while the displacement of the casing cement boundary was also almost 10 times higher than the arrow at the other two resonance frequencies.

Similarly, for the case of the 4½" tubing with a 9⅝" casing, Fig. 6a, there were three resonance peaks at 10 kHz, 15 kHz, and 20 kHz. The acoustic pressure changed significantly in the range of 15 kHz to 22 kHz, and the maximum change (78%) occurred at approximately 20 kHz. The other two resonance frequencies also show smaller changes (1.4% at 10 kHz and 54% at 15 kHz) due to the change of cement density. The mode shape and pressure distribution are plotted in Figs. 6b to 6d for 10 kHz, 15 kHz, and 20 kHz, respectively. Comparing Figs. 6b to 6d, the color in the casing cement area at 20 kHz (0.8 Pa) is much deeper than at 10 kHz and 15 kHz (0.4 Pa to 0.6 Pa).

In addition, for the case of the 9⅝" tubing with a 14" casing, there are four resonance peaks at 6 kHz, 10 kHz, 16 kHz, and 22 kHz. The acoustic pressure changed significantly in the range of 13 kHz to 18 kHz, and a maximum change (72%) occurred at approximately 16 kHz. The mode shape and pressure distribution are plotted in Figs. 7b to 7e for 6 kHz, 10 kHz, 16 kHz, and 22 kHz, respectively. The deepest color and maximum displacement of the cement layer are also observed for 16 kHz.

Those observations indicated that: (1) the entire system, including the housing, tubing, casing, and cement are simultaneously vibrating based on the mode shape at all resonance frequencies, but the relative displacement are different based on different mode shape, (2) the energy/pressure on the source surface at a specific frequency is significantly affected by the change of cement property, and (3) at a certain resonance frequency, the casing cement boundary has the highest displacement and energy concentration; and the frequency will change, depending on the tubing casing size combinations.

In Figs. 6a and 7a, it is observed that the resonance frequency peak for the good bond and the bad bond resonance frequency peak will shift at approximately 2 kHz, and the peaks shift at approximately 5 kHz at different tubing casing size combinations.

Simulation with PZT Transducer Source

To generate the continued acoustic wave in the TTCE, a cylindrical PZT transducer was used. In the simulation, the PZT source was also used to validate the possibility of measurement of the impedance signal, due to cement bond change, and is replaced in the source domain, as previously seen in Fig. 3c. The cylindrical transducer was designed to have the resonance radial model, which will continuously generate the normal incidence wave to excite the resonance model of tubing, casing, and cement. Due to the piezoelectric effect, the electrical states in the PZT crystalline will change when the force/pressure on the PZT is changed, leading to a change in the PZT impedance[11, 12].

Figure 8 shows two test cases with 4½" tubing with a 5½" casing combination and 4½" tubing with a 9⅝"

Fig. 8 Simulation results for impedance change due to B-annulus change: (a) for the 4½" tubing with a 5½" casing, and (b) for the 4½" tubing with a 9⅝" casing.

(a)

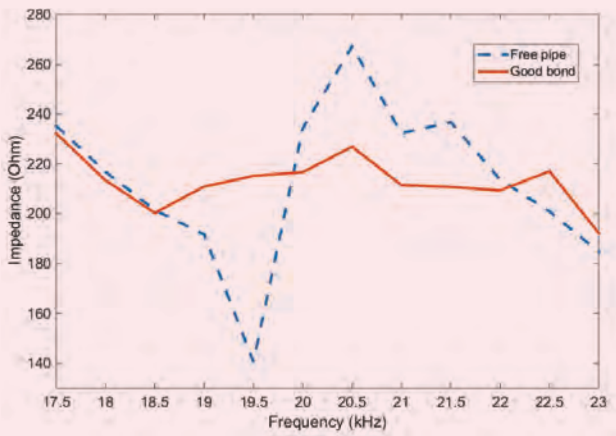

(b)

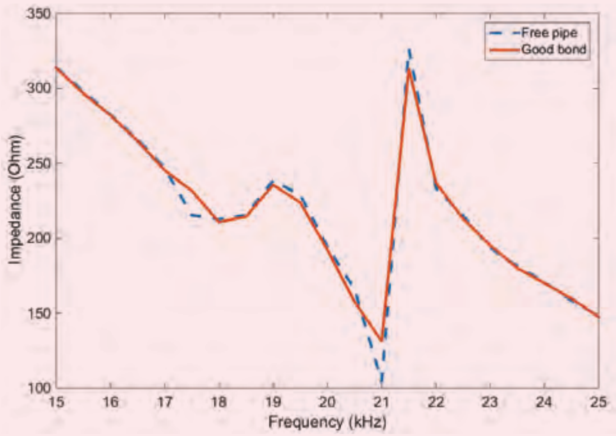

Fig. 9 *Pressure and displacement distribution for the 4½" tubing with a 9⅝" casing for (a) free pipe, and (b) good bond.*

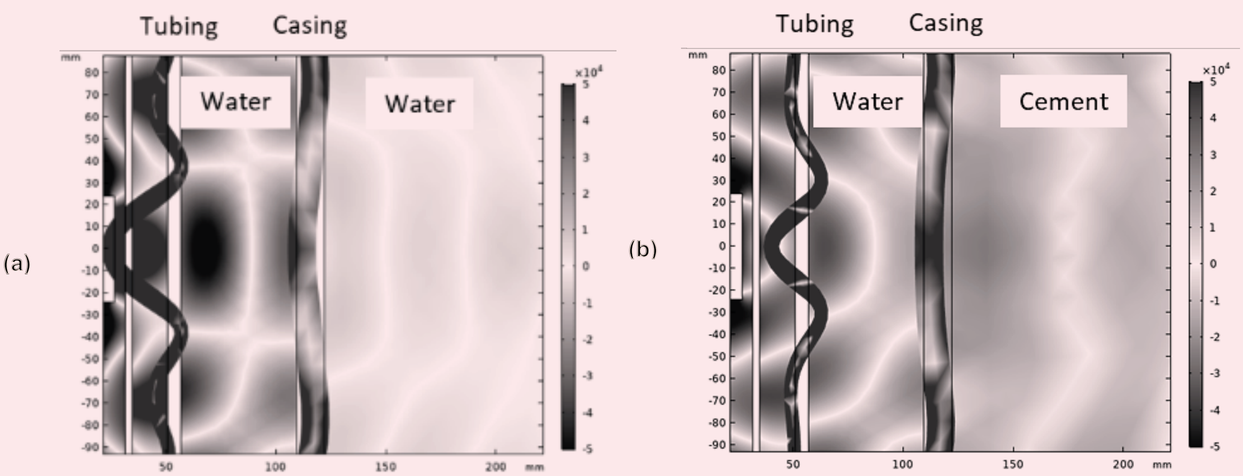

casing combination. It is observed that the most sensitivity is at 19.5 kHz for the 4½” tubing with a 5½” casing combination with 34% sensitivity, and at 21 kHz for the 4½” tubing with a 9⅝” casing with 20% sensitivity.

Figure 9 shows the pressure and displacement distribution for these two cases as a free pipe with water and a good bond with cement for the 4½” tubing with a 9⅝” casing combination. Comparing the B-annulus conditions, it is observed that the energy distributed in cement is much more than the energy in the water, and there is more energy located around the interior and the A-annulus for the free pipe case. Based on the simulation results, Figs. 8 and 9, it can be concluded that: (1) a significant change on the impedance for the good bond condition and free pipe condition is observed at the resonance frequency, and (2) the good bond condition has a higher impedance than the free pipe condition based on the PZT mechanism[9].

It is reasonable that the energy/acoustic wave is easier to transport to the formation through the cement bond, Fig. 9b, with less reflection and then the energy in the well system is less comparing to the free pipe condition, Fig. 9a.

Experiment Verification for SNHR Tool

Figure 10a shows the lab-scale double pipe well system that was established and the SNHR tool is validated. Two conditions for the B-annulus were applied for the good cement and the free pipe, and the two tubing casing combinations were tested for the 4½” tubing with a 5½” casing and the 4½” tubing with a 9⅝” casing. For the free pipe condition, Fig. 10b, the tubing and casing were immersed in water; for the good bond condition, Fig. 10c, the cement was bonded to the casing, and water was filled between the tubing, casing, and interior. The SNHR tool was inserted in the tubing and measured the signal in the middle of the system to avoid side effects from the top and

Fig. 10 *(a) Experiment setup for the double pipe system, (b) free pipe condition, and (c) good bond condition.*

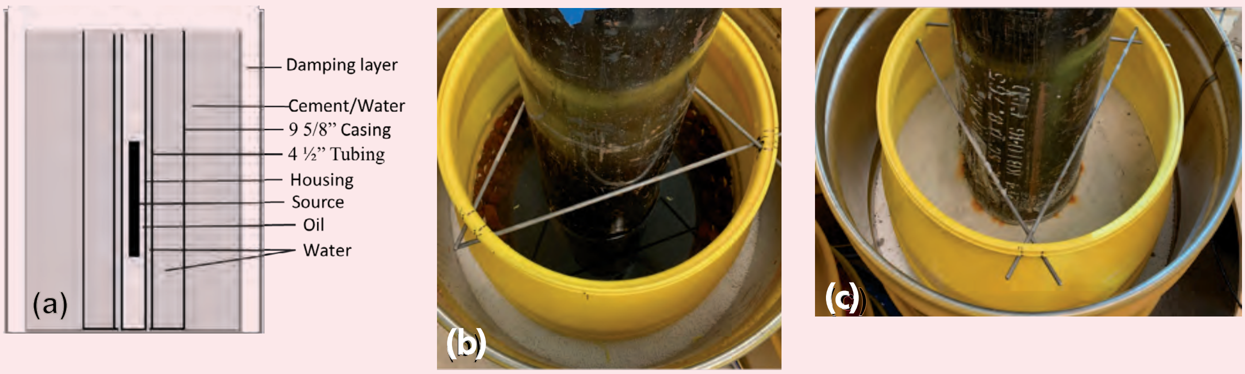

Fig. 11 *Experiment results for impedance change due to B-annulus change: (a) the 4½" tubing with a 5½" casing, and (b) for the 4½" tubing with a 9⅝" casing.*

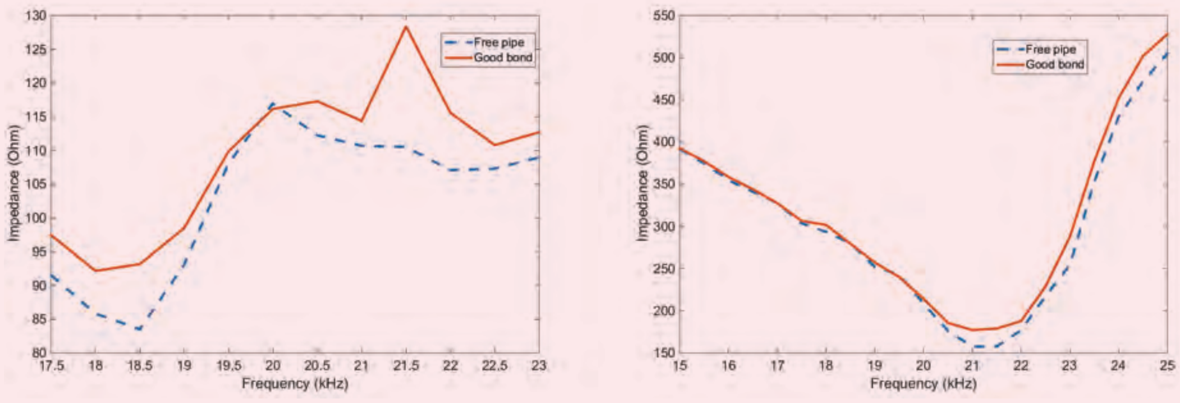

(a) (b)

bottom. The cylindrical PZT transducer was used for generating the continued acoustic wave in the radial model while measuring the signal when the entire system was under a desired resonance model.

The experiment results are shown in Figs. 11a and 11b. For the 4½" tubing with a 5½" casing, the resonance frequency is about 18.5 kHz with a sensitivity of approximately 7%, while the SNR is approximately 16 dB by considering the noise from background, equipment, and variation of the measurements. For the 4½" tubing with a 9⅝" casing, the resonance frequency is about 21 kHz with a sensitivity of approximately 12%, while the SNR is also approximately 16 dB.

This observation also agrees well with simulations in term of resonance frequency, and the trend of impedance for free pipe and good bond. The small difference between the experiment and simulation such as frequency, amplitude, and sensitivity, might be caused by the variation of material property and geometry.

Conclusions

This article proposed a new logging tool and method based on EMI to evaluate the cement bond condition in a multiple pipe environment. The concept was validated via simulation and experiments with a range of tubing and casing size combinations in a double pipe system. The impedance changes corresponding to cement bond condition were studied. It has been observed that:

- The impedance can characterize the change of the B-annulus cement bond condition with high sensitivity (> 7%) and SNR (> 16 dB), for the 5½" through 9⅝" or larger casings.
- The resonant frequency will shift when the tubing and casing sizes change and can be predicted based on the assumption of elastic linearity.
- A well bonded condition will yield impedance measurably higher than a free pipe.

This method could provide a feasible approach to evaluating cement bonds in the presence of multiple uncemented inner strings. This will significantly reduce the cost of a cement bond evaluation since the inner strings will not require removal prior to logging.

References

1. Vrålstad, T., Saasen, A., Fjær, E., Øia, T., et al.: "Plug and Abandonment of Offshore Wells: Ensuring Long-Term Well Integrity and Cost-Efficiency," *Journal of Petroleum Science and Engineering*, Vol. 173, February 2019, pp. 478-491.

2. Gowida, A.H., Ahmad, Z., Elkatatny, S. and Mahmoud, M.: "Cement Evaluation Challenges," SPE paper 192360, presented at the SPE Kingdom of Saudi Arabia Annual Technical Symposium and Exhibition, Dammam, Saudi Arabia, April 23-26, 2018.

3. Viggen, E.M., Johansen, T.F. and Merciu, I-A.: "Simulation and Modeling of Ultrasonic Pitch-Catch through Tubing Logging," *Geophysics*, Vol. 81, Issue 4, May 2016, pp. D369-D379.

4. Viggen, E.M., Johansen, T.F. and Merciu, I-A.: "Analysis of Outer-Casing Echoes in Simulations of Ultrasonic Pulse Echo through Tubing Logging." *Geophysics*, Vol. 81, Issue 6, November 2016, pp. D679-D685.

5. Sinha, B.K. and Zeroug, S.: "Geophysical Prospecting Using Sonics and Ultrasonics," in *Wiley Encyclopedia of Electrical and Electronics Engineering*, Webster, J.G. (ed.), John Wiley & Sons Inc., May 2001.

6. Zhang, J., Mahbod, P., Shafer, R., Mueller, D., et al.: "Multi-String Isolation Logging — A Cost-Effective Solution for P&A," SPE paper 195607, presented at the SPE Norway One Day Seminar, Bergen, Norway, May 14, 2019.

7. Wang, H., Fehler, M. and Fournier, A.: "Assessing Leak Paths in the Cement Sheath of a Cased Borehole by Analysis of Monopole Wavefield Modes," *Communications in Computational Physics*, Vol. 28, Issue 1, January 2020, pp. 424-441.

8. Liu, Y., D'Angelo, R.M., Sinha, B.K. and Zeroug, S.:

"Theoretical and Experimental Investigations of Acoustic Waves in Embedded Fluid-Solid Multi-String Structures," *Applied Physics Letters*, Vol. 110, Issue 10, March 2017.

9. Zhao, J., Yang, Q., Zhao, J. and Rourke, M.: "Acoustic Method of through Tubing Cement Bond Evaluation Based on Mie Resonances," paper presented at the SEG/AAPG/EAGE/SPE Research and Development Petroleum Conference and Exhibition, Abu Dhabi, UAE, May 9-10, 2018.

10. Spicci, L. and Cati, M.: "Ultrasound Piezo-Disk Transducer Model for Material Parameter Optimization," paper presented at the Comsol Conference, Paris, France, November 17, 2010.

11. Liang, C., Sun, F.P. and Rogers, C.A.: "Coupled Electromechanical Analysis of Adaptive Material Systems — Determination of the Actuator Power Consumption and System Energy Transfer," *Journal of Intelligent Material Systems and Structures*, Vol. 5, Issue 1, January 1994, pp. 12-20.

12. Huynh, T-C. and Kim, J-T.: "Impedance-Based Cable Force Monitoring in Tendon Anchorage Using Portable PZT Interface Technique," *Mathematical Problems in Engineering*, Vol. 2014, March 2014.

About the Authors

Dr. Jie Li

Ph.D. in Mechanical Engineering, Missouri University of Science and Technology

Dr. Jie Li is currently a Research Scientist at GOWell International, focused on next generation well integrity evaluation and well intervention, etc. He joined GOWell in 2018 as a Scientist, working on acoustic logging technologies.

Jie is the author of over 20 publications and patents.

In 2018, he received his Ph.D. degree in Mechanical Engineering from the Missouri University of Science and Technology, Rolla, MO.

Dr. QinShan Yang

Ph.D. in Signal Processing, Smart Antenna, and Array Acoustic Physics, Chinese Academy of Science

Dr. QinShan Yang is a Senior Advisor at GOWell International. He has more than 18 years of experience in the oil and gas industry. QinShan has worked in various positions for Schlumberger, CNPC, UT Austin, and now at GOWell. Currently, he is the Leader and Advisor in the field of well integrity, acoustic/electromagnetic tool physics, and DSA/DTS projects.

QinShan has published more than 20 technical papers and holds 12 patents. He is an active member of the Society of Petrophysicists and Well Log Analysts (SPWLA), the Society of Petroleum Engineers (SPE), and the Society of Exploration Geophysicists (SEG), and involved in various volunteering activities.

QinShan received his Ph.D. degree in Signal Processing, Smart Antenna, and Array Acoustic Physics from the Chinese Academy of Science, Beijing, China, and conducted his postdoctoral study on Petrophyics at the University of Texas, Austin, Texas.

Jinsong Zhao

MBA in Marketing, University of Antwerp

Jinsong Zhao is a Senior Research and Development (R&D) professional at GOWell International. He has 20 years of experience in the oil and gas industry, which includes work at Baker Hughes and Halliburton.

Jinsong's interests include technology innovation, systems engineering, R&D methodology, and competition strategy for developing new downhole logging tools for logging-while-drilling, open hole, and cased hole applications.

He has 22 granted U.S. patents and seven pending in the areas of sensor design, measurement system, and DSP algorithm.

Jinsong received his MBA in Marketing from the University of Antwerp, Antwerp, Belgium, and an M.S. degree in VLSI from Mississippi State University, Starkville, MI.

Marvin Rourke

B.S. in Cybernetics and Control Engineering, University of Reading

Marvin Rourke is currently the Technology Vice President at GOWell International, where he support the global customer basis and leads their technology development programs.

Marvin has over 30 years of experience in the wireline business where he started life as a Field Engineer with Gearhart Industries in the 1980s.

Marvin has authored and coauthored multiple Society of Petroleum Engineers (SPE) and Society of Petrophysicists and Well Log Analysts (SPWLA) papers over the years with a recent focus on well integrity applications.

In 1988, he received his B.S. degree in Cybernetics and Control Engineering from the University of Reading, Reading, U.K.

Mohamed Larbi Zeghlache

M.S. in Reservoir Engineering and Field Development, French Petroleum Institute

Mohamed Larbi Zeghlache is a Senior Researcher and the well integrity logging subject matter expert working with the Production Technology Team of Saudi Aramco's Exploration and Petroleum Engineering Center – Advanced Research Center (EXPEC ARC). He previously led the well integrity logging team in the Reservoir Description and Simulation Department.

Since joining Saudi Aramco, Mohamed has been responsible for formation evaluation and well placement in Ghawar carbonates and Central Arabia clastics.

He has 19 years of experience in the oil and gas industry, and previously worked with both Schlumberger and Halliburton where he held various positions, including Wireline Field Engineer, Log Analyst, Business Development, and Technical Advisor.

Mohamed is the author of several publications and patents.

He received his M.S. degree in Reservoir Engineering and Field Development from the French Petroleum Institute (IFP), Paris, France.

Sand Consolidation by Enzyme Mediated Calcium Carbonate Precipitation

Manar M. AlAhmari, Dr. Mohammed A. Bataweel, Dr. Abdulmohsen A. AlHumam and Dr. Abdullah A. AlMajed

Abstract / Sand production from poorly consolidated reservoir formations has been a persistent problem in the petroleum industry. Sand production can cause erosion and corrosion to downhole and surface equipment, along with causing a loss of production. Several technologies are used to reduce sand production effects, and subsequently, maintain well production and safe operations.

These techniques include completion techniques, and in situ chemical consolidation methods. The enzyme induced carbonate precipitation (EICP) is a reversible and environmentally friendly technique that can be used for sand consolidation. In EICP, the urease enzyme catalyzes the hydrolysis of urea in an aqueous solution, which results in ammonia and carbonic acid production. In the presence of calcium ions, the carbonate ions precipitate as calcium carbonate ($CaCO_3$). It has been reported that urease enzyme starts losing its activity above 65 °C, and therefore, this technology can only be applied in reservoirs with temperatures up to 65 °C. This study addresses an improved EICP method where protein is added and the technique can be applicable in high temperature reservoirs.

Two EICP solutions were prepared: (1) an EICP control solution, which contains the urease enzyme, calcium chloride ($CaCl_2$), and urea, and (2) a modified EICP solution, which consists of urease enzyme, $CaCl_2$, urea, and protein. The test specimens were made by mixing sand with an EICP solution and allowed to cure at different temperatures ranging from 25 °C to 130 °C. Additionally, X-ray diffraction (XRD) analysis was performed to identify the type of $CaCO_3$ polymorph. Scanning electron microscope (SEM) imaging was carried out to visualize the morphology of the $CaCO_3$ precipitation in the sand specimens.

Specimens treated with the solution containing protein (solution 2) had a high consolidation strength. As the temperature increases, the strength of consolidation decreases in specimens treated with solution 2 and 1. Consequently, the consolidation strength of the specimens treated with solution 2, which contains protein, was considerably greater at all temperatures — up to 130 °C — than the strength of specimens treated with solution 1. Moreover, XRD analysis revealed that 70% of the $CaCO_3$ polymorph in solution 2 was calcite — which is the most stable polymorph. SEM images show that in the specimens treated with solution 2, the $CaCO_3$ precipitates at inter-particle contacts.

The impact of these results include the use of the EICP protein technique as a downhole sand consolidation method in high temperature reservoirs. Furthermore, the addition of protein in the EICP solution can lead to a reduction in the concentration of substrate and enzyme required to achieve sand consolidation, and subsequently, a reduction in undesirable ammonium chloride. These advantages enhance the potential use of the EICP protein system for sand consolidation in high temperature reservoirs.

Introduction

Sand production in oil and gas wells is only one of the challenges that faces the oil industry[1]. It can have an impact on the different stages of the well's life, starting from drilling all the way to production. The existence of this challenge has financial, operational, productivity, and safety implications that need to be considered by engineers handling these wells. Sand accumulates in surface tools, the wellbore, pipelines, tubing, and separators, which eventually results in a decrease in production[1].

As sand travels in the wellbore and surface facilities, it can scratch and erode the metal parts, thereby enhancing the corrosion. This erosion process can damage valves, pumps, chokes, separators, and pipelines[2]. Other negative impacts of sand traveling particles is jamming the subsurface safety valve, which has serious safety and environmental concerns[2]. All of these can add to the operation and maintenance cost for the surface and subsurface facilities and hardware.

Sand removed from the bottom-hole or collected at the surface is coated with hydrocarbon materials, which is considered as hazardous waste that needs to be treated before disposal[2].

The objective of this article is to assess the suitability of the enzyme assisted $CaCO_3$ precipitation to mitigate sand production from medium to high temperature reservoirs. Also, we will discuss the impact of adding a protein source for sand consolidation quality.

Formation Sand Characteristic and Classification

Sand is classified into quick sand, unconsolidated, semi-consolidated, friable, consolidated, moderate, and hard. Table 1 summarizes the formation sand characteristics and classifications based on unconfined compressive strength (UCS), hardness, core observations, and sonic travel-time. Next, we will define different formation sand types.

First, the quick sand, which is completely unconsolidated sand with no cementing material between the grains[2]. Such sand has small cohesive force and these formations are categorized by difficulty during drilling, and sand production occurs at the early stages of the well production. The other sand type is unconsolidated sand, which has some cementing agents, but is still weakly consolidated and is characterized by high porosity and permeability.

These formations are very brittle, and wells with open hole completions collapse in such formations. The friable or semi-consolidated sand, are well cemented formations with no initial sand production during the first stages of hydrocarbon production, however, sand production occurs over time[2]. For semi-consolidated formations, it is very difficult to make decision on whether or not sand control techniques should be applied. Finally, consolidated sand is sand that is well cemented and does not require sand control methods[2].

Causes of Sand Production

Sand production can be caused by several factors:

- High production rate: As the production rate increases, fluid dragging on the sand grain increases, applied stress on the formation exceeds the formation strength and sand production begins[3].
- High drawdown pressure: To increase the production rate, drawdown between the reservoir pressure and bottom-hole flowing pressure is increased. This can aggravate the sand production. The production of the hydrocarbon fluids causes frictional losses and friction forces on the grain that can exceed the formation compressive strength and result in sand production.
- Reservoir pressure depletion: The pore pressure by fluids within the reservoir will support the formation with the inherent strength of the rock. When fluids are produced and the reservoir becomes depleted, it leads to an increase in the amount of effective stress on the formation, which will dislocate or crush the formation particles, resulting in sand production[3].
- Water production: The increase in the water cut is associated with increase in sand production, due to the following mechanisms. In sandstone formations, the cohesiveness between particles is provided via surface tension by the connate water. When water is produced, the connate water will adhere to the produced water weakening the particle-to-particle bond by reducing the surface tension forces. The second mechanism is the reduction in the hydrocarbon relative permeability when saturation of water around the wellbore is increased, resulting in a higher differential required to maintain the hydrocarbon production rate. Furthermore, produced water can result in cementing material dissolution that weakens the rock or clay swelling, which can block the porous media and result in increasing the pressure gradient that destabilizes the formation. Also, an increase in water cut can aggravate the de-attachment of migratable clays[3].
- Unconsolidated formations: Sandstone cementation usually happens due to secondary geological

Table 1 *Formation sand characteristic and classifications.*

Rock Classification	UCS	Brinnel Hardness Number (kg/mm²)	Core Observation	Approximate Sonic Travel-Time (us/ft)
Quicksand	0	0	Hole slumps	> 150
Unconsolidated	< 1,000	< 2	No apparent cement between sand grains	> 145
Semi-consolidated	1,000-2,500	2-5	Easily crushed	> 130
Friable	2,500-3,500	5-10	Rub-off grains	105-130
Consolidated	3,500-7,500	10-30	Crushable with forceps	105-175
Moderate Hard	7,500-12,000	30-50	Cannot crush	65-75
Hard	12,000-20,000	50-125	Cannot crush	40-65

processes. For this reason, a deeper formation will have harder rocks when compared to younger/shallow geological sediments[2]. Unconsolidated formations with a low degree of cementations and very low cohesive forces can be dislodged easily by early hydrocarbon production[4].

Methods to Manage Sand Production

Several methods are used to control sand production from oil and gas reservoirs and these include the restriction of production rate, and both mechanical methods and chemical methods.

Production Rate Control

The critical production rate is reached by restricting the well from its optimum production to achieve maximum sand-free production. This is a trial and error method and the optimum rate needs to be reset based on reservoir pressure and water cut. According to the target production, this method may result in significant loss of well productivity and revenue[2, 3, 5].

Figure 1 shows an example of the field correlation between the flow rate and amount of sand produced[5].

Well Completions and Mechanical Methods

The mechanical means to control sand is based on eliminating sand production by using downhole tools, or increasing the surface area to lower the fluid velocity at the sand face like the frac-pack technique. The commonly used mechanical sand control methods are slotted liners, screens and gravel pack, or a combination of more than one technique. While such methods control formation sand from entering the wellbore, they lead to higher skin that reduces the production rate[1].

The slotted liner or screen function as a filter. Slotted liners are wrapped opposite to sand producing interval. The slot cuts are too small to allow sand flow into the wellbore, while still allowing the flow of formation fluids. The gravel pack is a method that uses a screen placed directly against the formation. The annulus between the formation and the screen is packed with gravel of a specific size designed to prevent the influx of formation sand into the wellbore. The frac-pack technique combines two distinct processes; productivity enhancement by hydraulic fracturing and sand control by gravel packing[6].

Figure 2 illustrates several completion techniques that are used to control sand production.

Fig. 1 *The field correlation between production rate and amount of sand produced[5].*

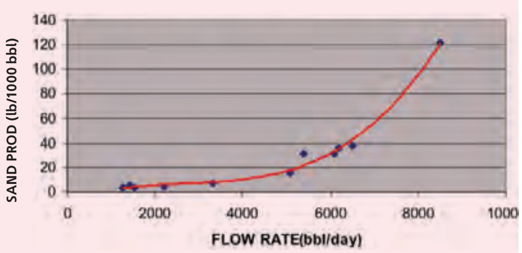

In Situ Chemical Methods

Sand control by chemical consolidation involves injecting liquid chemicals, such as plastic resins, polymers, and nanoparticles into loose formations, which bind the sand grains together, Fig. 3. The advantage of this method over other types of sand exclusion methods is that chemical consolidation can be applied in small diameter wellbores without a rig. In addition, chemical consolidation does not require the installation of any downhole tools, providing a cost-effective technique of sand control for primary and remedial completions[8].

There are several types of commercially available polymers that are used to consolidate sand, and these include epoxy, furan, and phenolic resins. Generally, the resins are in a liquid form when entering the formation, and a catalyst — also called curing agent — is needed for hardening[9]. There are two types of resin systems, internally activated and externally activated systems (overflush systems). The internally activated systems

Fig. 2 *Several sand control completion techniques used to control sand production[7].*

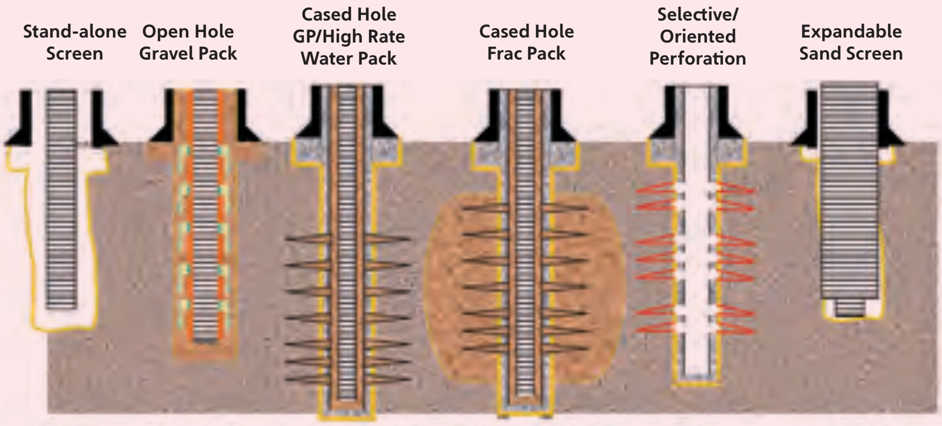

Fig. 3 *Chemicals connecting grains as sand consolidation treatments[12].*

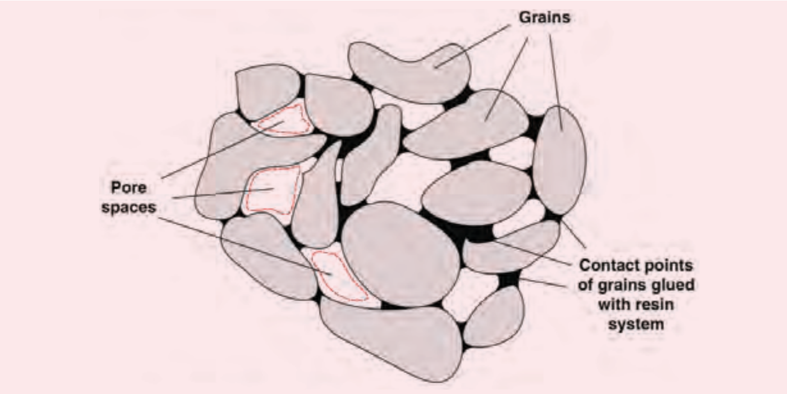

consist of a resin solution mixed with a catalyst at the surface and the hardening of the resin starts at the surface[9]. Such a system is very time-dependent and reacts rapidly in high temperature. Due to premature hardening, the success of internally activated systems is limited in very high temperature wells or in high clay formations. The externally activated systems are when the resin is first injected in the formation and then a catalyst is pumped after the resin is in place[9].

Resins, such as epoxy, furan, and phenolic resins, can have a limited temperature range and become degraded at high temperature. Therefore, other chemical consolidation systems have been developed for high temperature reservoirs. Water soluble organosaline has been used as a chemical method for sand control. Organosalines react with water molecules trapped in formation pores, reacting with the hydroxyl groups on the sand grain surface, forming a network between sand grains[10].

The zeta potential system is another method used for sand control, where it alters the surface charge on sand particles by creating an ionic attraction and induces their agglomeration[3]. Moreover, Larsen et al. (2007)[11] provided a new sand control chemical method, which involves the in situ enzyme mediated calcium carbonate ($CaCO_3$) precipitation as a cementing agent between sand grains.

Enzymatic $CaCO_3$ Precipitation

Theory

Enzymatic assisted $CaCO_3$ precipitation for grains cementation is an environmentally friendly, reversible chemical system that is proposed for sand consolidation by in situ precipitation of $CaCO_3$ between loose sand grains in the reservoir[11]. The reversibility of this solution is addressing the concern of engineers of potential plugging of the reservoir with other solutions based on resin mediated sand consolidation chemicals. If the permeability is impacted drastically by the enzymatic-based solution during the chemical placement process, acid can be injected and some of the lost permeability can be retained, since $CaCO_3$ is an acid soluble material.

Chemical Reaction

The concept is based on precipitating $CaCO_3$ in the interparticle contact between sand grains. This is achieved by having the $CaCO_3$ in the aqueous solution with enough quantities to precipitate in a controlled manner. The calcium is provided as a salt in the mixing solution and carbonate is provided by more complex chemistry to have a more delayed and controlled reaction[11].

The breakdown of urea to generate carbonate follows multiple step process, Eqns. 1 and 2. First, the urea will hydrolyze with the help of the biocatalyst enzyme (urease) to ammonia and carbonic acid, Eqn. 1. The carbonic acid is in equilibrium with hydrogen carbonate and carbonate ions, Eqn. 3. The formed carbonate will react with calcium precipitating $CaCO_3$ when the critical concentration is reached, Eqn. 4[11].

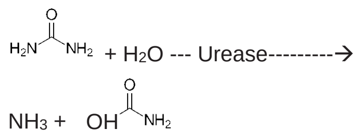

1

2

$$H_2CO_3\ (aq) ==== HCO_3^-\ (aq) + H^+\ (aq)$$
$$===== CO_3^{2-}\ (aq) + 2H^+ \quad (3)$$

$$Ca^{2+}\ (aq) + CO_3^{\ 2-}\ (aq) \rightarrow CaCO_3\ (s) \quad (4)$$

To further enhance the enzyme performance, Nemati and Vordouw (2003)[13] proposed to add protein in the form of skimmed milk as an enzyme stabilizer. The addition of protein helped in reducing the enzyme concentration by two orders of magnitude[11]. Larsen et al. (2007)[11] advocated using jack beans due to their high protein content and enzyme activity, and therefore, having a synergetic effect of both components. Larsen et al. (2007)[11] also discussed the crystallization process and factors affecting it. To control the size, size distribution and crystallization process during the precipitation, the authors studied the effect of surface charge, zeta potential, the presence of impurities, stoichiometric variation, and the addition of divalent and trivalent ions.

Experimental Procedures

Materials

Solutions were mixed from deionized (DI) water, calcium chloride ($CaCl_2$) dihydrate (($CaCl_2 \cdot 2H_2O$), > 99% purity, Sigma-Aldrich GmbH, Selzee, Germany, urea ((NH_2)2CO), > 99.5% purity, Sigma-Aldrich GmbH, Selzee, Germany, and in some cases, urease-active meal (from jack beans) (Fisher Scientific, U.K.) and/or skimmed milk powder as a protein source.

Solutions Preparation

Four different solution samples were prepared in glass test tubes to investigate the effect of enzymes and proteins on $CaCO_3$ precipitation. Solution 1 (baseline enzyme induced carbonate precipitation (EICP) solution) consisted of 1.0 M urea, 0.67 M $CaCl_2$, 3 g/L enzyme dissolved in DI water. Solution 2 (modified EICP solution) contained 1.0 M urea, 0.67 M $CaCl_2$, 3 g/L enzyme, and 4 g/L protein dissolved in DI water. Solution 3 was prepared by dissolving 1.0 M urea, 0.67 M $CaCl_2$, and 4 g/L protein in DI water, and finally, solution 4 consisted of 1.0 M urea, and 0.67 M $CaCl_2$ dissolved in DI water.

Table 2 summarizes the chemical formulations for solutions used in this study.

Test Tube Experiments for $CaCO_3$ Crystallization

The four solutions mentioned in Table 2 were prepared to study the effect of enzymes, proteins, and temperature on $CaCO_3$ crystallization. Each test tube sample was prepared by adding 64.3 ml (about 1 pore volume (PV)) of the solution in glass test tubes. Solution samples were then closed with plastic lids to minimize solution evaporation. Each test tube was allowed to cure at different temperatures (25 °C, 90 °C, 100 °C, and 140 °C) for at least 72 hours. Precipitation of each test tube was then filtered, oven-dried and subjected to scanning electron microscopy (SEM) and X-ray diffraction (XRD) analysis.

Preparation of EICP Solution for Sand Treatment

The EICP treatment solutions consisted of $CaCl_2$, urea, urease enzyme, and in some cases, protein dissolved in DI water. Two different EICP solutions were used for consolidating sand: (1) The baseline EICP solution (solution 1) composed of 1.0 M urea, 0.67 M $CaCl_2$, and 3 g/L enzyme, and (2) The modified EICP treatment solution, was composed of 1.0 M urea, 0.67 M $CaCl_2$, 3 g/L enzyme, and 4 g/L protein.

Sand Column Experiments

Specimens were prepared in glass bottles filled with sand to investigate enzymatic protein mediated $CaCO_3$ precipitation. Each test sample was prepared by thoroughly mixing 300 g of sand with 64.3 ml (about 1 PV) of the EICP solution. The sand and solution were mixed and then placed in glass bottles in three lifts. Each lift of sand was gently tamped until the solution was a few millimeters above the soil surface, indicating that the packed soil was nearly saturated.

The glass bottles were then closed with plastic lids to minimize evaporation of the solution. Each glass bottle was allowed to cure at different temperatures for at least 72 hours. After curing, the specimens were oven-dried at 40 °C for 24 hours until a constant mass was achieved.

Microstructural Analysis

For the test tube experiments, SEM imaging and energy dispersive X-ray spectroscopy (EDS) microanalysis techniques were utilized to characterize the samples. SEM samples were prepared from the four samples (solution 1, 2, 3, and 4), and were mounted onto SEM sample holders prior to inserting into the SEM analysis chamber.

As SEM-EDS spectra can only determine the elements, a complementary XRD technique was applied to determine the different types of $CaCO_3$ phases. The four samples were ground and homogenized using an agate mortar and pestle to achieve a fine size. Samples were then mounted by front pressing into the sample holder and then XRD analysis was carried out.

Results and Discussion

The Effect of Chemical Composition and Temperature on $CaCO_3$ Precipitation

The four solutions described in Table 2 were tested for $CaCO_3$ precipitations at 25 °C, 90 °C, 100 °C, and 140 °C. Results show that at 25 °C, 70 °C, and 100 °C no $CaCO_3$ precipitation was observed with solutions 3 and 4 (without enzyme). On the other hand, the addition of urease (solutions 1 and 2) induced $CaCO_3$ precipitation. Therefore, we concluded that the enzyme is required to induce urea hydrolysis and subsequent $CaCO_3$ precipitation at low and intermediate temperature conditions up to 100 °C.

SEM images show that the addition of protein to the EICP solution (solution 2) induces the formation of large $CaCO_3$ crystal aggregates compared to solution 1 (without protein) at 25 °C, 70 °C, and 100 °C, Fig. 4.

The Effect of Enzyme, Protein and Temperature on $CaCO_3$ Crystallization

The SEM images in Fig. 4 show the precipitated $CaCO_3$ by solutions 1 and 2 at temperatures of 25 °C, 70 °C, and 100 °C. Several observations can be seen from these images. First, precipitated $CaCO_3$ aggregates are

Table 2 *A summary of chemical formulations used in this study.*

Name	Chemical Formulation
Solution 1 (EICP)	1.0 M urea, 0.67 M $CaCl_2$, 3 g/L enzyme dissolved in DI water
Solution 2 (Modified EICP)	1.0 M urea, 0.67M $CaCl_2$, 3 g/L enzyme, and 4 g/L protein dissolved in DI water
Solution 3	1.0 M urea, 0.67 M $CaCl_2$, and 4 g/L protein in DI water
Solution 4	1.0 M urea, 0.67 M $CaCl_2$ dissolved in DI water

Fig. 4 *SEM backscattered electron images for solutions 1 and 2 at different temperatures: (a) Solution 1 (without protein) at 25 °C, (b) Solution 2 (with protein) at 25 °C, (c) Solution 1 (without protein) at 70 °C, (d) Solution 2 (with protein) at 70 °C, (e) Solution 1 (without protein) at 100 °C, and (f) Solution 2 (with protein) at 100 °C.*

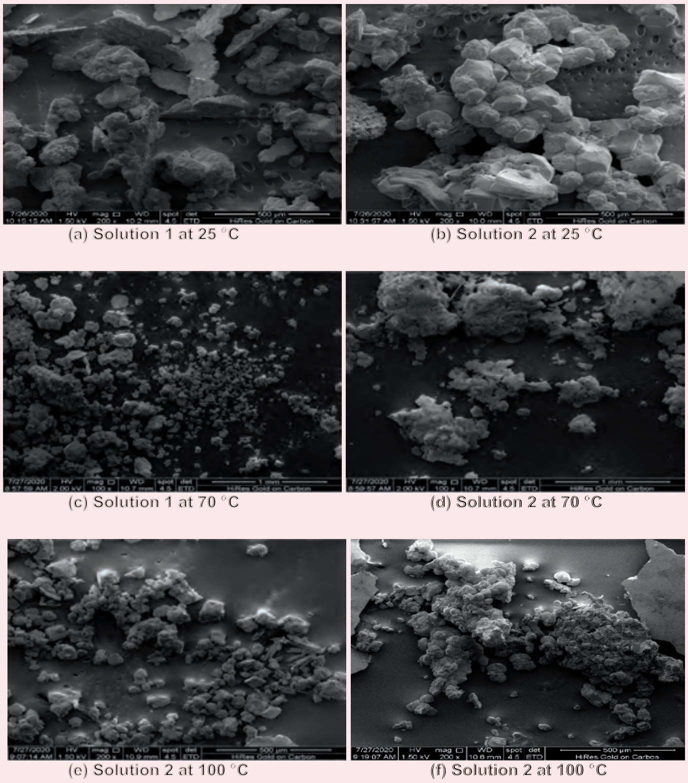

larger in the solution with enzyme and protein at all temperatures compared to solution 1. Second, $CaCO_3$ particles (crystals) are smaller in higher temperatures compared to lower temperatures. In the case of solution 2, the particles are aggregated forming larger clusters.

$CaCO_3$ Precipitation at Elevated Temperatures (140 °C)

A study has shown that urea decomposition and eventually $CaCO_3$ precipitation can only take place at high temperatures — starting at 110 °C — without the need of an enzyme catalyst[14]. We hypothesized that increasing the temperature induces urea decomposition. At 140 °C, $CaCO_3$ precipitation was observed in all four solutions.

$CaCO_3$ has different crystal polymorphs seen in nature as minerals. These include three anhydrous polymorphs: calcite, aragonite, and vaterite, of which calcite is the most common and stable. XRD analysis confirmed the precipitation of variable levels of the three $CaCO_3$ polymorphs, Table 3. The addition of urease (solutions 1 and 2) provoked the formation of calcite, while the exclusion of urease (solutions 3 and 4) induced the formation of aragonite, which is considered to be less stable compared to calcite. The addition of protein to the EICP solution showed a slight increase in the percentage of calcite formation compared to the EICP solution without protein.

Furthermore, in solution 2 (with protein) the precipitated carbonate appeared to be in the form of relatively large calcite crystal aggregates compared to the EICP solution without protein, where calcite appeared to be in the form of small crystals, Fig. 5. In addition, the SEM imaging confirms the presence of $CaCO_3$ in aragonite needle form in samples 3 and 4. From this test we conclude the following:

- The addition of urease in the formulation resulted in forming more calcite (stable) compared to more aragonite (less stable) formed when urease is removed.
- The addition of protein with the EICP solution had a slight increase in the calcite concentration's larger crystals when compared with the sample without protein.

The difference in the size of calcite crystals could be explained by the rate of the reaction. The large calcite crystals that formed when protein was added to the EICP solution could be due to the molecular interaction of protein with the active sites on the enzyme, reducing the accessibility of such sites to urea, subsequently lowering the precipitation rate[15]. Additionally, the precipitation of proteins might act as nucleation sites that favor large calcite crystal aggregation[16].

Strength of Sand Consolidation

Geotechnical researchers have been investigating the use of enzymatic $CaCO_3$ precipitation as a soil improvement technique. A study has shown that the addition of milk (as a source of protein) to the EICP solution increases the strength of sand consolidation[16], however, this method was not tested at high temperature conditions.

Table 3 *XRD analysis for the three different polymorphs of $CaCO_3$ precipitated by different solutions at 140 °C.*

Compound	Solution 1 (Baseline EICP solution) (wt%)	Solution 2 (Modified EICP solution) (wt%)	Solution 3 (wt%)	Solution 4 (wt%)
Calcite ($CaCO_3$)	62	70	34	36
Aragonite ($CaCO_3$)	18	26	55	64
Vaterite ($CaCO_3$)	12	12	11	—

Fig. 5 *SEM backscattered electron images and corresponding EDS spectrum for (a) solution 1, (b) solution 2, (c) solution 3, and (d) solution 4 at 140 °C.*

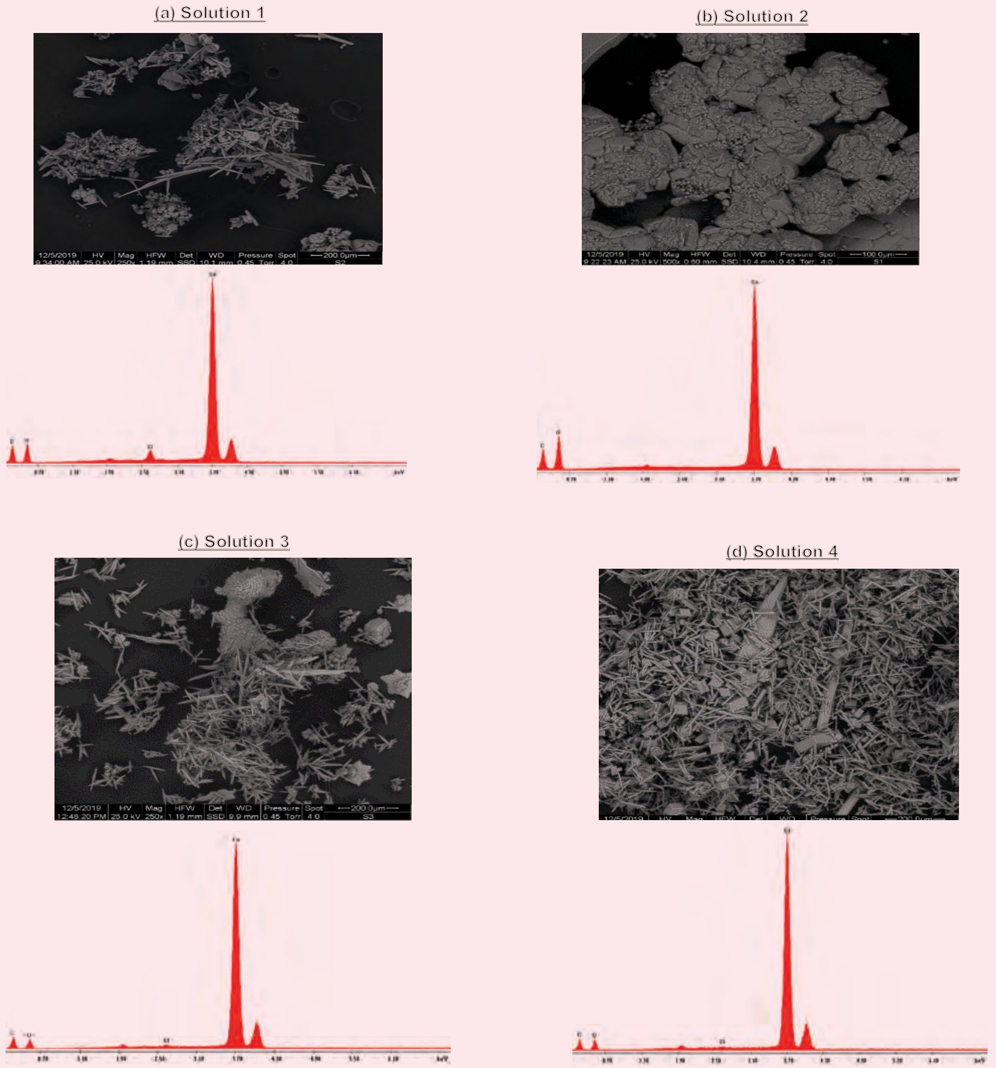

Based upon our test tube results, we hypothesized that the modified EICP solution (solution 2, with protein) can consolidate sand at high temperature conditions. In our study, it was visually apparent that sand consolidation developed in specimens treated with the modified EICP solution (solution 2, with protein), Table 4 and Fig. 6, while very weak to no consolidation developed in specimens treated using the baseline solution (solution 1, without protein), Table 4. As the temperature increases, the consolidation strength of the specimens treated with solution 2 decreases.

Subsequently, the consolidation strength was considerably greater at all temperatures (up to 130 °C) in the treated sand samples with solution 2 compared to specimens treated with solution 1. This could be due to the amount of calcite precipitation between sand particles. Therefore, the calcite level was measured in sand samples treated with solutions 1 and 2 at 25 °C, 90 °C, and 100 °C, Table 5.

The amount of calcite in the samples treated with solution 2 at 25 °C, 90 °C, and 100 °C is 1%, 0.5%, and 0.4%, respectively, Table 5. As the temperature increases, the amount of calcite precipitated between sand grains decreases. The calcite level in samples treated with solution 2 at all temperatures is higher compared to the samples treated with solution 1, Table 5.

The increase in calcite level and subsequent strength in sand samples treated with solution 2 could be due to the protein that protects the enzyme from its surrounding, and therefore, maintain its activity[11]. In addition, the $CaCO_3$ precipitation pattern is believed to be a major contributor to the increase strength of the specimens treated with solution 2 (with protein) compared to specimens treated with an EICP solution that did not contain protein.

A study has shown a difference in $CaCO_3$ precipitation

Table 4 Consolidation of sand specimens at different temperatures.

Solution	25 °C	80 °C	90 °C	100 °C	110 °C	120 °C	130 °C
Solution 1 (Baseline EICP solution, without protein)	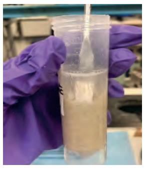	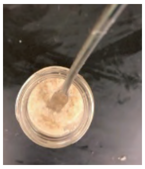	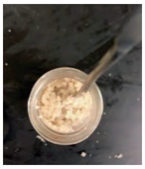	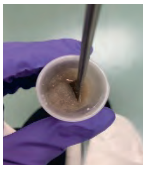		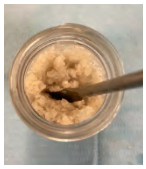	
Solution 2 (Modified EICP solution, with protein)					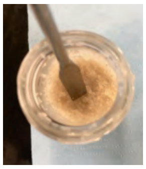		

Fig. 6 Sand specimens treated with the modified EICP solution (with protein): (a) Consolidation of sand at 70 °C, and (b) at 130 °C.

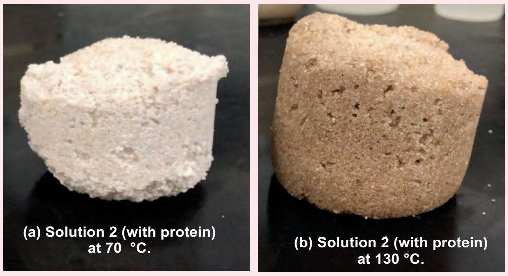

patterns between sand samples treated with solution 2 that contains protein, and samples treated with the baseline EICP solution (without protein), Fig. 7[16]. For the specimens treated with solution 2, the precipitated $CaCO_3$ appears to be in the form of large calcite crystals focused at interparticle contacts. In contrast, in the specimens treated with the baseline EICP solution, calcite crystals appeared to be small in size and on the surface of the sand grains. The results of our study suggest that the addition of protein plays a role in increasing the amount of calcite as well as changing the morphology of calcite into large crystals between sand grains[16].

Table 5 XRD semi-quantitative phase analysis.

Solution	25 °C	90 °C	100 °C
Solution 1 (Baseline EICP solution, without protein)	0.6% calcite	0.2% calcite	0.1% calcite
Solution 2 (Modified EICP solution, with protein)	1% calcite	0.5% calcite	0.4% calcite

Fig. 7 SEM images of calcite precipitated between sand grains: (a) and (b) Sand particles treated with the baseline EICP solution (without protein) showing small calcite crystals on the particle surface, and (c) and (d) Sand particles treated using the modified EICP solution (with protein) showing large calcite crystals at interparticle contacts. The solid arrows point to interparticle bonds; the dashed arrows show broken interparticle bonds[16].

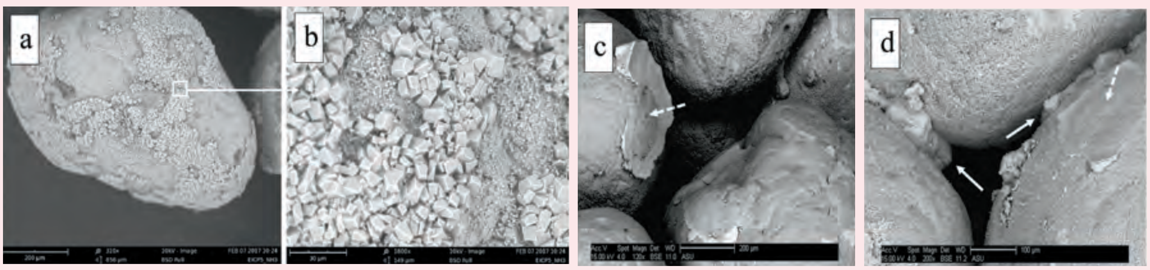

Conclusions

In this article, the concept of controlling sand production from a low to high temperature reservoir by protein mediated enzymatic $CaCO_3$ precipitation has been investigated.

1. Lab results demonstrated that the protein mediated enzymatic $CaCO_3$ precipitation could be a promising chemical technology in consolidating sand in low to high temperature reservoirs.
2. Urease enzyme is needed to precipitate $CaCO_3$ as cementing material at reservoir temperatures less than 100 °C.
3. The enzymatic $CaCO_3$ precipitation technique is environmentally friendly and reversible.
4. The addition of the enzyme urease in the formulation resulted in forming more calcite (stable) compared to more aragonite (less stable) formed when urease was removed.
5. At elevated temperatures (140 °C), urea decomposed and precipitated the $CaCO_3$ without the need of an enzyme. Consequently, use of an enzyme (urease) with protein precipitated the more stable calcite compared to aragonite when urease was not added.
6. Lab experiments showed that the addition of protein to the EICP solution induced sand consolidation at high temperatures — up to 130 °C — by inducing a higher concentration of calcite with larger crystals between sand grains. This suggests that the protein mediated enzymatic $CaCO_3$ chemical system can be applied in high temperature reservoirs.

Acknowledgments

The authors would like to express their thanks to Wajdi Buhaezae and Dr. Hameed Badairy for their technical support.

References

1. Khamehchi, E., Ameri, O. and Alizadeh, A.: "Choosing an Optimum Sand Control Method," *Egyptian Journal of Petroleum*, Vol. 24, Issue 2, June 2015, pp. 193-202.

2. Mahmud, H.B., Leong, V.H. and Lestariono, Y.: "Sand Production: A Smart Control Framework for Risk Mitigation," *Petroleum*, Vol. 6, Issue 1, March 2020, pp. 1-13.

3. Mishra, S. and Ojha, K.: "Chemical Sand Consolidation: An Overview," *Journal of Petroleum Engineering and Technology*, Vol. 5, January 2015, pp. 21-34.

4. Tao, Q., Ghassemi, A. and Birchwood, R.: "Poroelastoplastic Analysis of Factors Controlling Sand Production from a Hemispherical Cavity," paper presented at the 42nd U.S. Rock Mechanics Symposium (USRMS), San Francisco, California, June 29-July 2, 2008.

5. Abass, H.H., Nasr-El-Din, H.A. and Bataweel, M.A.: "Sand Control: Sand Characterization, Failure Mechanisms, and Completion Methods," SPE paper 77686, presented at the SPE Annual Technical Conference and Exhibition, San Antonio, Texas, September 29-October 2, 2002.

6. Weirich, J., Li, J., Abdelfattah, T. and Pedroso, C.: "Frac Packing: Best Practices and Lessons Learned from More Than 600 Operations," *SPE Drilling & Completion*, Vol. 28, Issue 2, June 2013, pp. 119-134.

7. Petroblogger.com: "Fracturing and Sand Control in an Oil Well," available at: http://www.ingenieriadepetroleo.com/fracturing-sand-control-oil-well/, 2013, accessed on August 5, 2020.

8. Osisanya, S.O.: "Practical Guidelines for Predicting Sand Production," SPE paper 136980, presented at the Nigeria Annual International Conference and Exhibition, Tinapa, Calabar, Nigeria, July 31-August 7, 2010.

9. Economides, M., Watters, L.T. and Dunn-Norman, S.: *Petroleum Well Construction*, John Wiley and Sons Ltd., 1998, 640 p.

10. Morkved, M.L., Knight, C., Bhagwan, B., Algora, A.G., et al.: "Chemical Consolidation of Sand Propped Fractures in a Chalk Reservoir Offshore Denmark with Enzymatic Calcium Carbonate Scale," IPTC paper 17456, presented at the International Petroleum Technology Conference, Doha, Qatar, January 19-22, 2014.

11. Larsen, J., Poulsen, M., Lundgaard, T. and Agerbaek, M.: "Plugging of Fractures in Chalk Reservoirs by Enzymatic Induced Calcium Carbonate Precipitation," SPE paper 108589, presented at the SPE Offshore Europe Oil and Gas Conference and Exhibition, Aberdeen, Scotland, U.K., September 4-7, 2007.

12. Matanovic, D., Cikes, M. and Moslavac, B.: *Sand Control in Well Construction and Operation*, New York: Springer Science & Business Media, 2012, 207 p.

13. Nemati, M. and Voordouw, G.: "Modification of Porous Media Permeability, Using Calcium Carbonate Produced Enzymatically in Situ," *Enzyme and Microbial Technology*, Vol. 33, Issue 5, October 2003, pp. 635-642.

14. Sahu, J.N., Mahalik, K., Patwardhan, A.V. and Meikap, B.C.: "Equilibrium and Kinetic Studies on the Hydrolysis of Urea for Ammonia Generation in a Semibatch Reactor," *Industrial and Engineering Chemistry Research*, Vol. 47, Issue 14, June 2008, pp. 4689-4696.

15. Bachmeier, K.L., Williams, A.E., Warmington, J.R. and Bang, S.S.: "Urease Activity in Microbiologically Induced Calcite Precipitation," *Journal of Biotechnology*, Vol. 93, Issue 2, February 2002, pp. 171-181.

16. Almajed, A., Tirkolaei, H.K., Kavazanjian Jr., E. and Hamdan, N.: "Enzyme Induced Biocementated Sand with High Strength at Low Carbonate Content," *Scientific Reports*, Vol. 9, Issue 1, February 2019.

About the Authors

Manar M. AlAhmari

M.S. in Biochemistry, Alfaisal University

Manar M. AlAhmari is a Petroleum Scientist in productivity enhancement working with the Production Technology Division of Saudi Aramco's Exploration and Petroleum Engineering Center – Advanced Research Center (EXPEC ARC). She joined Saudi Aramco in October 2019, and her research interests include biotechnology and biochemistry.

Manar's work includes the development of environmentally friendly biotechnological applications to resolve current challenges in vital upstream operations. She is currently working on developing different chemistries, including fracturing fluids and novel chemical methods, for sand control.

Manar is the author/coauthor of a number of scientific publications in international journals and conference proceedings. She is also the inventor/co-inventor of six patents.

Manar received her B.S. degree in Biochemistry from Cardiff University, Cardiff, Wales, U.K. She received her M.S. degree in Biochemistry from Alfaisal University, Riyadh, Saudi Arabia.

Dr. Mohammed A. Bataweel

Ph.D. in Petroleum Engineering, Texas A&M University

Dr. Mohammed A. Bataweel is a Champion for the Productivity Enhancement foucs area in the Production Technology Division of Saudi Aramco's Exploration and Petroleum Engineering Center – Advanced Research Center (EXPEC ARC). Mohammed has led his team in the development and deployment of several in-house technologies in Saudi Aramco fields. Throughout his career, he has represented his department on several field development, asset, and multidisciplinary teams.

Mohammed's research interests include formation damage due to drilling and completion fluids, investigation and mitigation of injectivity decline, conformance control, sand production prediction, special core analysis, chemical enhanced oil recovery, productivity enhancement technologies, visualization of fluid flow in porous media, and oil field chemicals.

He is an active member of the Society of Petroleum Engineers (SPE) where he has served on several conferences. Mohammed initiated and co-chaired several SPE advanced technical workshop series in the region. He has published approximately 100 technical papers in local and international conferences and refereed journals, along with a number of patents.

Mohammed received his B.S. degree in Mechanical Engineering from King Fahd University of Petroleum and Minerals (KFUPM), Dhahran, Saudi Arabia, and his M.S. degree in Petroleum Engineering from Harriot-Watt University, Edinburgh, U.K. Mohammed received his Ph.D. degree in Petroleum Engineering from Texas A&M University, College Station, TX.

Dr. Abdulmohsen A. AlHumam

Ph.D. in Petroleum Microbiology/ Biotechnology, University of Portsmouth

Dr. Abdulmohsen A. AlHumam is a Science Specialist working with the Production Technology Division of Saudi Aramco's Exploration and Petroleum Engineering Center – Advanced Research Center (EXPEC ARC). He joined Saudi Aramco in1993, and since that time, Abdulmohsen has completed several field assignments. Abdulmohsen is involved in several projects covering different aspects of applied microbiology, microbial influenced corrosion, biofilm control, drilling mud, and cement mix fluid microbial contamination.

He has published several papers in international journals, and presented several technical papers in national and international conferences.

Abdulmohsen has been granted two patents from the U.S. Patent Office. He is the first scientist to introduce a new nitrate treatment technology to control reservoir microbial souring for Saudi Aramco.

In 2009, Abdulmohsen completed his M.S. degree and Ph.D. degree program in Petroleum Microbiology/Biotechnology from the University of Portsmouth, Hampshire, U.K.

Dr. Abdullah A. AlMajed

Ph.D. in Civil, Environmental and Sustainable Engineering, Arizona State University

Dr. Abdullah A. Almajed was appointed Assistant Professor in the Department of Civil and Environmental Engineering at King Saud University (KSU) in April 2018. His research focuses on bio-geotechnical engineering and biogeochemical processes for ground improvement and remediation. Abdullah investigated the mechanical properties of enzyme-induced carbonate precipitation (EICP) treated soil under different carbonate contents and different treatments.

His expertise includes experimentation and analytical testing related to mineral precipitation using biological processes and macromolecules such as free urease enzymes and biopolymers. Abdullah is also involved in several projects related to the improvement of the mechanical properties of the soil, surficial soil stabilization, and environmental remediation.

In 2017, he received his Ph.D. degree in Civil, Environmental and Sustainable Engineering from Arizona State University, Tempe, AZ.

High-Resolution Micro-Continuum Approach to Model Matrix Fracture Interaction and Fluid Leakage

Xupeng He, Marwah M. AlSinan, Dr. Hyung T. Kwak and Dr. Hussein Hoteit

Abstract /

Understanding the fundamental mechanism of fracture matrix fluid exchange is crucial for the modeling of fractured reservoirs. Traditionally, high-resolution simulations for flow in fractures often neglect the matrix fracture leakage influence on the fracture hydraulic properties, i.e., assuming impermeable fracture walls. In this work, we develop a micro-continuum approach to capture the matrix fracture leakage interaction and its impact on the hydraulic properties of rock fractures.

Because of the multiscale nature of the fracture and matrix rocks, full physics Navier-Stokes (NS) representation everywhere in the whole domain is not feasible. We therefore employ NS equations to describe the flow in the fracture, and Darcy's law to model the flow in the surrounding porous rocks. Such hybrid modeling is achieved using the extended Darcy-Brinkman-Stokes (DBS) equation. With this approach, a unified conservation equation for flow in both media is applied by choosing appropriate parameters, e.g., porosity and permeability, for the corresponding domains. We apply an accurate mixed finite element approach to solve the extended DBS equation. Analytical solutions are used to verify the numerical method. Various sensitivity analyses are conducted to explore the leakage effects on the fracture hydraulic properties by varying surrounding matrix permeability, fracture roughness, and Reynolds number (*Re*).

Streamline profiles show the presence of backflow phenomena, where inflow and outflow are possible between the matrix and the fractures. Further, zones of stagnant (eddy) flow are observed around locations with large asperities of sharp corners under high *Re* conditions. This implies the existence of dynamic trapping mechanisms that may impact the relative permeabilities and residual saturations within the fractures. Numerical results show the significant effects of roughness and inertia on flow predictions in fractures for both impermeable and leaky wall cases. In addition, the side leakage effect can create nonuniform flow distribution in the fracture, which deviates significantly from the flow with impermeable wall conditions. This matrix fracture leakage influence on hydraulic properties of rock fractures matters especially for cases with high matrix permeability, high fracture roughness, and low *Re* values.

In summary, we present a high-resolution micro-continuum approach to explore the flow exchange behavior between the fracture and rock matrix, and further investigate the static and dynamic effects, including variable *Re*, mimicking flow near and away from the wellbore. The approach and results provide a profound insight into the fluid flow through fractures within permeable rocks and can be readily applied in field-scale reservoir simulations.

Introduction

Good knowledge of hydraulic behaviors of discrete rock fractures is crucial for modeling and further assessing various subsurface activities, such as nonaqueous phase liquids tracking, geothermal energy extraction, geological carbon dioxide sequestration, and oil recovery process in fractured reservoirs.

The Navier-Stokes (NS) equations provide the most accurate approach for analyzing the hydraulic properties of rock fractures[1, 2]. Intensive computation cost makes it infeasible for applying NS equations as a practical approach. With a sufficiently small Reynolds number (*Re*), we can approximate the NS equations by the Stokes equations. The computational burden of solving the Stokes equations is still huge, even though cheaper than the NS equations. The cubic law, describing discrete rock fractures as two smooth parallel plates with a constant distance, has been used widely in many disciplines due to its simplicity and efficiency.

Natural rock fractures, however, exhibit the characteristics of a rough surface, variable aperture, and contact areas. These features of rock fractures make the validity of the cubic law questionable[3-5]. Many researchers have proposed various modifications based on the cubic law to improve its performance. Examples include:

(1) modifying the definition of the aperture used in the cubic law, such as the arithmetic mean[5], geometric mean[6], harmonic mean[7], among others, (2) incorporating a correction factor such as the contact area[8], roughness[9], tortuosity[10], and even combined effect[11].

A comprehensive study by Konzuk and Kueper (2004)[4] shows that the cubic law using geometric means or an appropriate roughness correction factor offered reasonable flow prediction within the flow regime of a *Re* number less than 1. These models, however, show unstable performance when dealing with complex fracture cases due to the neglect of flow behavior at the local scale. As an alternative, the local cubic law also referred to as the Reynolds equation, captures the local flow behaviors by accounting for the spatial variation in the aperture field with the assumption of the cubic law being valid at each explicit location. The local cubic law, however, shows two main assumptions — a flat fracture mid-surface and parabolic velocity profile, which limit its broad applicability. Many efforts have been taken to improve its accuracy. Brown et al. (1995)[12] considered the fracture mid-surface effect by introducing a correction factor.

Mourzenko et al. (1995)[13] proposed the concept of a normal aperture and suggested the "ball" aperture, resulting in a significant improvement. Ge (1997)[14] considered the combined effect of flow tortuosity and normal aperture. Oron and Berkowitz (1998)[15] conducted a dimensionless, 2D order-of-magnitude analysis to the NS equations and found the cubic law may be valid within certain segments. Brush and Thomson (2003)[1] and Nicholl et al. (1999)[16] explored and tested various link transmissivity formulations into the Reynolds equations with the finite difference and finite volume approaches, respectively. A detailed description of these improved models could be found in the related references.

All these previous theories, including the NS, Stokes, cubic law, and even Reynolds equations, are built based on the assumption of impermeable fracture walls, i.e., neglecting the matrix fracture leakage interaction. Few studies focus on fluid flow through discrete rock fractures in the permeable rock. Basha and El-Asmar (2003)[17] derived the perturbation solution based on the 2D NS equations by considering the leakage effect. This perturbated solution is only applicable for fracture cases with simple geometry, which cannot capture the complex flow behaviors between matrix and fracture, such as backflow and eddy phenomena. Crandall et al. (2010)[18] developed a modified NS equation based on finite-volume schemes to model fluid flow through fractured porous media by adding Darcy's term. Without the treatment of choosing different parameters, i.e., porosity and permeability, in different corresponding domains, the modeling approach[18] loses some generality.

Mathematical Model

We employ a micro-continuum approach, whereby a unified equation holds for flow in both domains: fracture and matrix. By choosing the appropriate parameters in corresponding domains, the extended Darcy-Brinkman-Stokes (DBS) equations could describe fluid flow in the fracture and surrounding matrix using the NS and Darcy equations, respectively. We assume the steady-state of incompressible, Newtonian, single-phase flow, and the extended DBS could be written as:

$$\frac{1}{\phi}\left\{\nabla\bullet\left[\frac{\rho}{\phi}\bar{u}\otimes\bar{u}\right]\right\}=-\nabla p+\frac{\mu}{\phi}\nabla^2\bar{u}+\bar{f}-\mu K^{-1}\bar{u}$$
$$\nabla\bullet\bar{u}=0 \tag{1}$$

In Eqn. 1, ρ is fluid density, $\bar{u}$ is velocity vector, p is pressure, and μ is fluid viscosity; ϕ and K are porosity and permeability, respectively, which are selected based on the corresponding domains (fracture or matrix).

- In the fracture region Ω^f:

$$\begin{cases}\phi=1\\ K=\infty\end{cases}\qquad \nabla\bullet\left[\rho\bar{u}\otimes\bar{u}\right]=-\nabla p+\mu\nabla^2\bar{u}+\bar{f} \tag{2}$$

We can observe that Eqn. 1 reduces to the NS equations with the selection of parameters.

- In the matrix region Ω^p:

$$\begin{cases}\phi=\phi_M\\ K=K_M\end{cases}\qquad \mu K_M^{-1}\bar{u}+\nabla p+$$
$$\frac{1}{\phi_M}\left\{\nabla\bullet\left[\frac{\rho}{\phi_M}\bar{u}\otimes\bar{u}\right]\right\}-\frac{\mu}{\phi_M}\nabla^2\bar{u}=\bar{f} \tag{3}$$

Whereas Darcy's law is given as:

$$\mu K_M^{-1}\bar{u}+\nabla p=\bar{f} \tag{4}$$

Observe that the differences between Eqn. 3 and Eqn. 4 are these two additional terms highlighted in red. The term $\mu K_M^{-1}\bar{u}$ in Eqn. 3 would dominate many orders of magnitude for fluid flow in porous media compared to these two additional terms, which will introduce a sufficiently small perturbation to Darcy's law.

The extended DBS equations offer the following advantages compared to the coupled Darcy-NS approach. A detailed description of the coupled Darcy-NS equations could be given in Popov et al. (2009)[19]. First, it allows a unified equation to capture flows in both domains by choosing different parameters in the corresponding domain. Second, we avoid formulating specific interface conditions, resulting in significant simplification in numerical treatment. Finally, it provides an efficient framework to simulate partially filled fractures or particle suspension in the fluid, as this unified approach can capture the flow varying from a Darcy dominated flow to an NS dominated flow.

Boundary Conditions: As observed in Fig. 1, the pressure inlet and outlet values are imposed at the fracture's inlet and outlet, respectively. No-slip boundary conditions are assigned to both the top and bottom sides. The gradient of the velocity in the direction of the pressure gradient is set to zero to guarantee the fully developed flow, and to avoid the inlet effect. We use fluid of water with ρ = *1,000 kg/m*^{3} and μ = *0.001 kg/(m · s)*. Herein, we assume the matrix to be homogeneous and isotropic with constant porosity.

Mixed Finite Element Implementation

The extended DBS equations can be arranged as:

$$\mu K^{-1}\vec{u}+\nabla\bullet\left[p\vec{I}-\frac{\mu}{\phi}\nabla\vec{u}\right]+\frac{1}{\phi^2}\rho\left(\vec{u}\bullet\nabla\right)\vec{u}=\vec{f}$$
$$\nabla\bullet\vec{u}=0 \qquad (5)$$

The extended DBS equations can be formulated in a mixed variational form, where the velocity and the pressure are approximated simultaneously. Multiplying Eqn. 5 by the test function $(\vec{v},q)$, and integrating the resulting equations over the domain Ω yields:

$$\int_\Omega \mu K^{-1}\vec{u}\bullet\vec{v}dx+\int_\Omega\nabla\bullet\left[p\vec{I}-\frac{\mu}{\phi}\nabla\vec{u}\right]\bullet\vec{v}dx+$$

$$\int_\Omega\frac{1}{\phi^2}\rho\left(\vec{u}\bullet\nabla\right)\vec{u}\bullet\vec{v}dx=\int_\Omega\vec{f}\bullet\vec{v}dx$$

$$\int_\Omega\left(\nabla\bullet\vec{u}\right)qdx=0 \qquad (6)$$

Applying the integration by the parts technique, we have:

$$\int_\Omega\nabla\bullet\left[p\vec{I}-\frac{\mu}{\phi}\nabla\vec{u}\right]\bullet\vec{v}dx=-\int_\Omega\left[p\vec{I}-\frac{\mu}{\phi}\nabla\vec{u}\right]\nabla\bullet$$

$$\vec{v}dx+\int_{\partial\Omega}\left[p\vec{I}-\frac{\mu}{\phi}\nabla\vec{u}\right]\vec{v}\bullet\vec{n}ds$$

$$=-\int_\Omega p\nabla\bullet\vec{v}dx+\frac{\mu}{\phi}\int_\Omega\nabla\vec{u}:\nabla\vec{v}dx+$$

$$\int_{\partial\Omega}\left[p\vec{I}-\frac{\mu}{\phi}\nabla\vec{u}\right]\vec{v}\bullet\vec{n}ds \qquad (7)$$

Using the abstract framework, we have the problem finding $(\vec{u},p)\in W$ such that:

$$a\left(\left(\vec{u},p\right),\left(\vec{v},q\right)\right)=L\left(\left(\vec{v},q\right)\right) \qquad (8)$$

For all $(\vec{u},p)\in W$, where

$$a\left(\left(\vec{u},p\right),\left(\vec{v},q\right)\right)=\mu K^{-1}\int_\Omega\vec{u}\bullet\vec{v}dx-\int_\Omega p\nabla\bullet$$

$$\vec{v}dx+\frac{\mu}{\phi}\int_\Omega\nabla\vec{u}:\nabla\vec{v}dx+\frac{\rho}{\phi^2}\int_\Omega\left(\vec{u}\bullet\nabla\right)\vec{u}\bullet\vec{v}dx+$$

$$\int_\Omega\left(\nabla\bullet\vec{u}\right)qdx \qquad (9)$$

$$L\left(\left(\vec{v},q\right)\right)=\int_\Omega\vec{f}\bullet\vec{v}dx-\int_{\partial\Omega}\left[p\vec{I}-\frac{\mu}{\phi}\nabla\vec{u}\right]\vec{v}\bullet\vec{n}ds$$

$$=\int_\Omega\vec{f}\bullet\vec{v}dx-\int_{\partial\Omega_{inlet}}p_{inlet}\vec{n}\bullet\vec{v}ds\left(inlet\right)-$$

$$\int_{\partial\Omega_{outlet}}p_{outlet}\vec{n}\bullet\vec{v}ds\left(outlet\right) \qquad (10)$$

Fig. 1 *An illustration of the boundary conditions imposed on the fractured rock (fracture + matrix).*

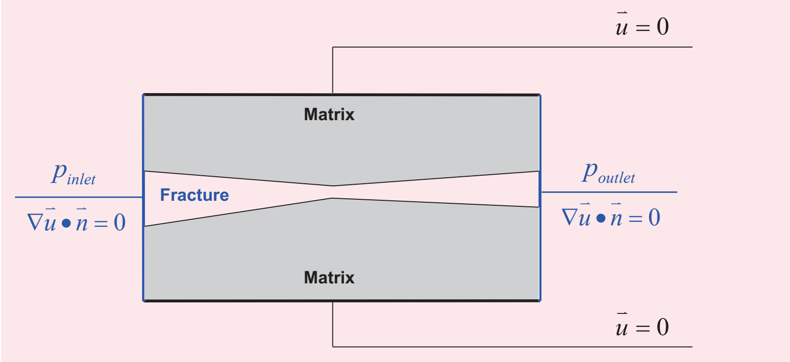

The space W should be a mixed function space: $W = V\times Q$ such that $\vec{u}\in V$ and $q\in Q$.

All the simulations in this study are run on the open-source platform called FEniCS[20]. We automate the whole process, including mesh generation, running simulations, and flow rate calculation.

Sensitivity Analysis

This section will provide high-resolution simulations to capture the matrix fracture physics and further perform various sensitivity analyses — matrix permeability, fracture roughness, and *Re* number — to explore the leakage influence on the hydraulic properties of rock fractures.

Fracture Profiles Generation

We first generate fracture profile No. 1 using software SynFrac, a synthetic fracture generator. We then perform perturbation on fracture No. 1 using the moving average technique, by which we can generate fracture profiles with different roughness, yet with the same mean aperture. Figure 2 shows the six 2D fracture profiles used in this study, showing different roughness and tortuosity. The corresponding geometric properties

Fig. 2 *Six 2D fracture profiles used in this study.*

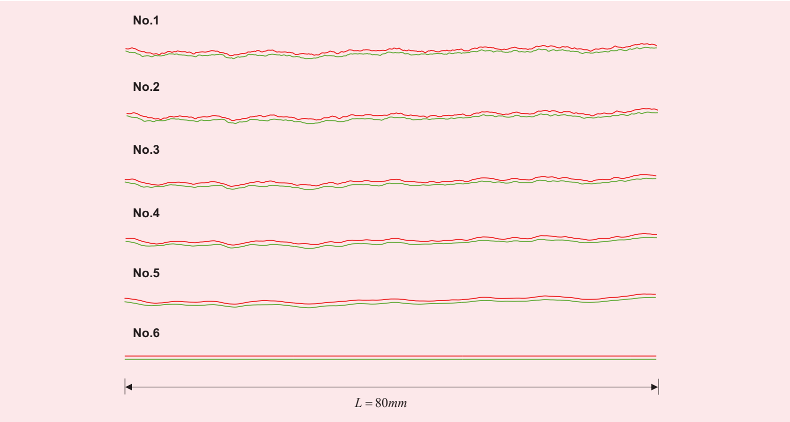

are summarized in Table 1. We should note that the fractured rock (fracture + matrix) model is constructed by embedding these 2D fracture profiles into a rectangle domain.

Impermeable Walls: Inertial and Roughness Effects

We first investigate the flow behaviors in discrete rock fractures with impermeable walls, and then extend impermeable cases to fracture cases with leaky walls. Herein, we apply the high-resolution NS equations to model fluid flow inside the discrete rock fractures. A detailed description of the numerical implementation of NS equations is given in Appendix A.

Inertial Effect: We investigate the inertial impact by varying the *Re* number on the same fracture profile. Figure 3 shows the eddy evolution (size and shape) with the increasing *Re* number in part of fracture profile No. 1. The eddy generally occurs around the locations with a local large asperity of sharp corners under high *Re* number conditions. The eddy exerts a significant influence on fluid flow through rock fractures by shrinking the effective flow channel. Given that eddies, an enclosed and separated region, show no flux interaction with the flow channel, the expansion of eddies further narrow the effective flow channel, and therefore reduce the fracture transmissivity. The inertial influence on fracture transmissivity is quantitative, Fig. 4, left, which agrees with the previous simulation observations in Fig. 3.

Roughness Effect: We investigate the roughness influence by varying the pressure values at the fracture inlet under the same *Re* number of 1. We observe in Fig. 5 that more pressure drop is required in rougher

Table 1 *The corresponding geometric properties of fracture profiles No. 1 to 6.*

No.	a_m (μm)	σ_a (μm)	*JRC*	τ
1	500	118.5	17.0	1.031
2	500	110.5	13.6	1.021
3	500	97.3	9.7	1.013
4	500	83.6	7.0	1.009
5	500	62.6	3.1	1.004
6	500	0	0.0	1.000

Note: a represents the vertical aperture field with arithmetic mean a_m, and standard deviation σ_a. *JRC* refers to the joint roughness coefficient used to quantify the fracture surface roughness τ refers to tortuosity, defined as the ratio of the flow path to the straight line distances of the fracture.

Fig. 3 *The flow streamlines in part of fracture profile No. 1, over a range of* Re *numbers from 1 to 150, showing the size and shape of eddy increases as the* Re *number increases — effective flow channel indicating a reverse trend.*

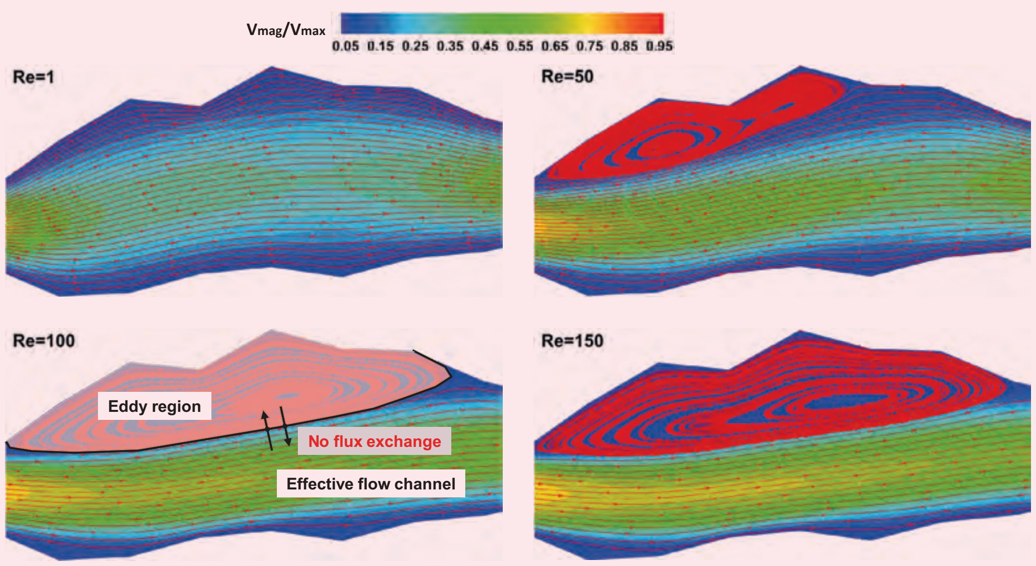

Fig. 4 *The normalized transmissivity (T/T_0) vs.* Re *number for fracture No. 1 (left); normalized transmissivity ($T/T_{JRC=0}$) vs. the JRC for fracture Nos.1 to 6 under the flow regime of* Re *= 1 (right).*

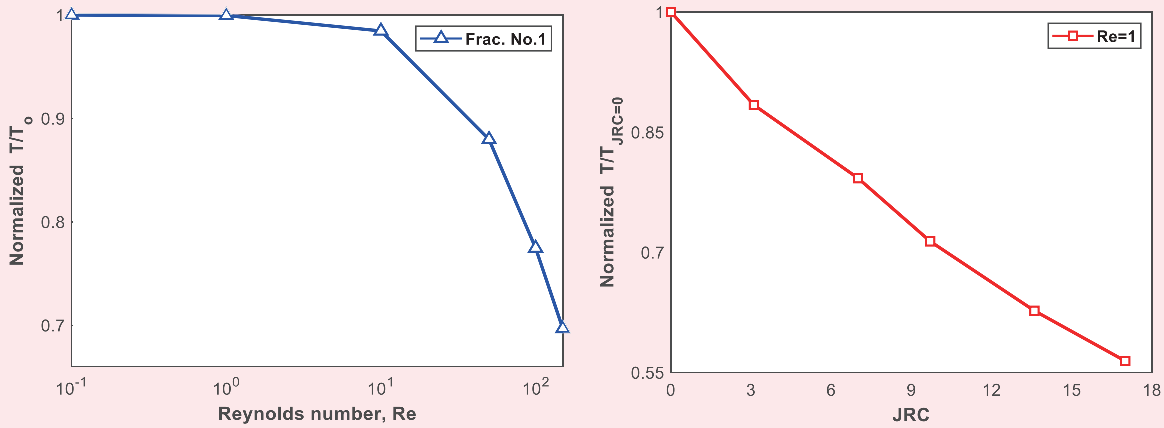

Fig. 5 *The pressure distribution for different fracture profiles under the same* Re *= 1, showing the roughness influence on the fluid flow through rock the fractures.*

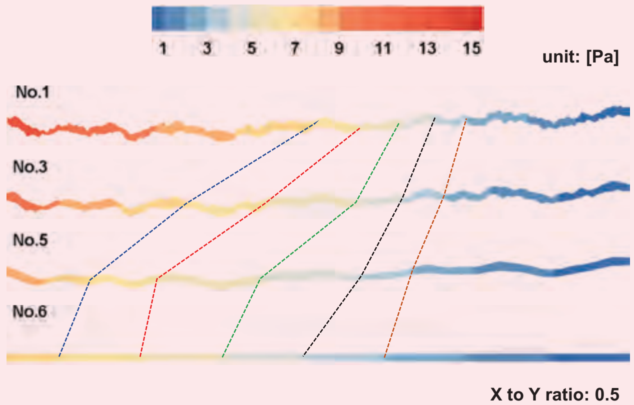

Fig. 6 *(a) Pressure distributions within fracture profile No. 1 with a matrix permeability of 50 md, and a pressure gradient of 10 Pa/m (corresponding* Re *0.05), and (b) Pressure across the lines of y = -0.016, - 0.010, -0.004, and 0.*

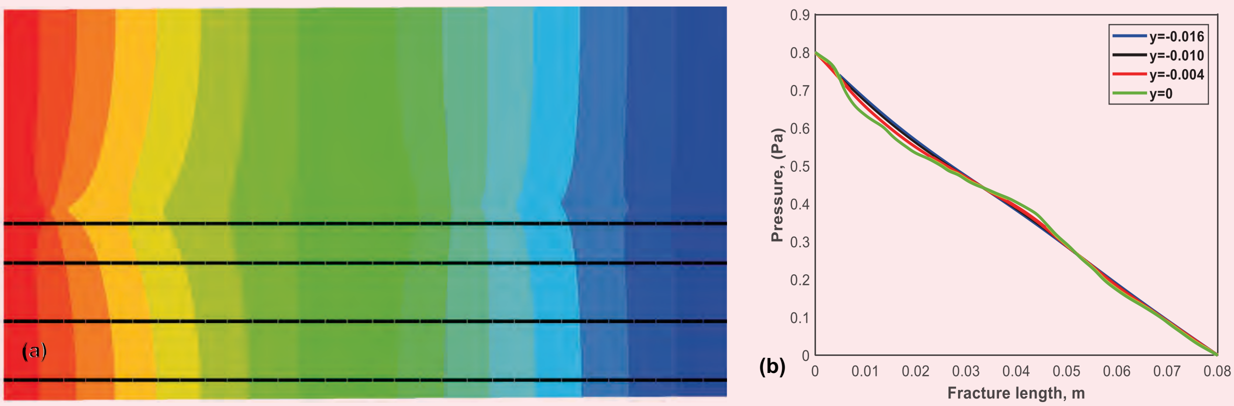

Fig. 7 *(a) The flux through fracture outlet vs. matrix permeability and fracture roughness under the pressure gradient of 10 Pa/s, and (b) The flux through fracture outlet vs. matrix permeability and pressure gradient for fracture profile 1.*

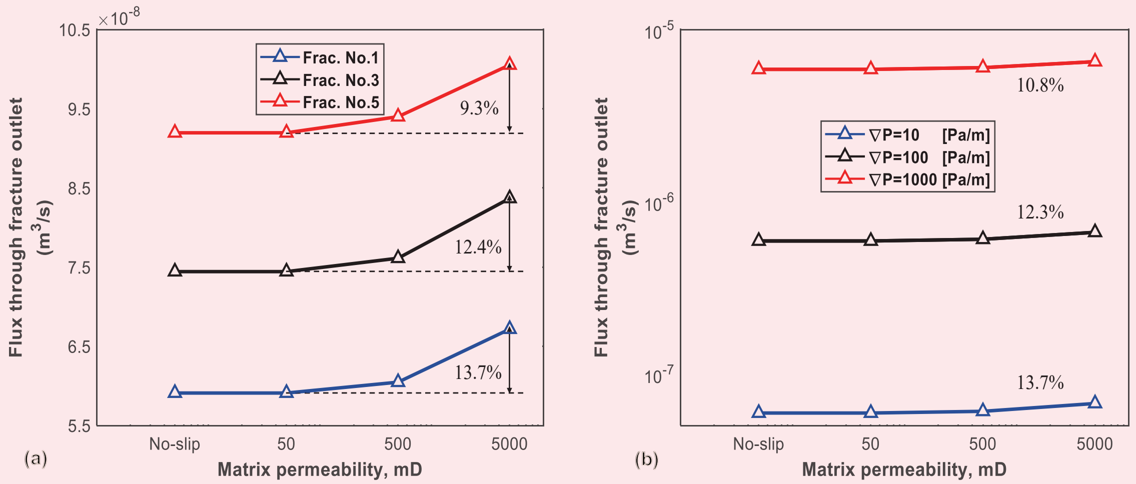

fractures than smooth fractures under the same *Re* number. As roughness introduces resistance to flow, it results in reducing the fracture hydraulic properties. We quantitatively provide the relation between normalized transmissivity and the *JRC* in Fig. 4, right, for fracture profiles Nos. 1 to 6 under *Re* = 1.

Leaky Walls: Matrix Fracture Interaction

We solved the extended DBS equations using mixed finite formulation on the FEniCS platform. We performed mesh refinement until the difference of flow solutions is within 0.1%. We then set the matrix porosity to be 0.4 for all simulations and the formation height of 40 mm.

Figure 6a shows the pressure tends that decrease linearly along the direction of the fracture length in the far fracture areas. This observation agrees with Darcy's law. The pressure exhibits a significant deviation from the essential linear trend near the fracture profile, due to the matrix fracture interaction. These conclusions are further illustrated in Fig. 6b.

We conducted the high-resolution extended DBS simulations on different fracture profiles (Nos. 1, 3, and 5) with varying matrix permeability (50 md, 500 md, and 5,000 md). We also add impermeable cases (denoted as "no-slip") to highlight the matrix fracture influence. Figure 7a shows the matrix fracture leakages' increasing impact on the flux through the fracture outlet with the increase of matrix permeability. It increases the flux 13.7% compared to flow in the fracture with impermeable walls (denoted as "no-slip") for fracture profile No. 1. The leakage influence would decrease as the fracture roughness decreases under the same matrix permeability. Figure 7b shows that the matrix fracture interaction exerts decreasing influence as the *Re* number increases for the same fracture profile due to the existence of eddies.

We then perform the simulation on fracture profile No. 1 with varying matrix permeability (50 md, 500 md, and 5,000 md) under different pressure gradients (10 Pa/m, 100 Pa/m, and 1,000 Pa/m). Impermeable cases also are included for comparison.

Figure 8 shows the velocity profiles for fracture profile No. 1 with the pressure gradient of 1,000 Pa/m and matrix permeability of 500 md, and Fig. 7b shows the streamline distribution in the exaggerated area of the white box.

Fig. 8 *(a) The velocity profiles for fracture profile No. 1 with the pressure gradient of 1,000 Pa/m and matrix permeability of 500 md, and (b) The streamline distribution in the exaggerated area of the white box.*

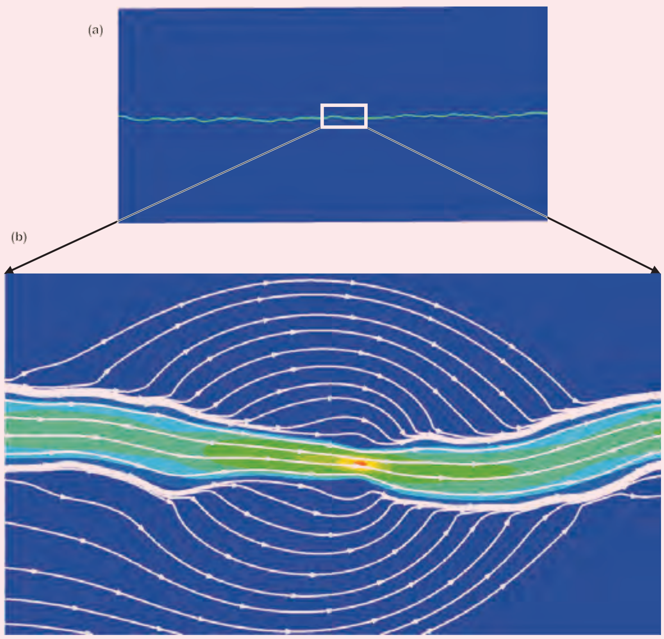

Fig. A1 An illustration of the boundary conditions imposed on the rough fracture walls.

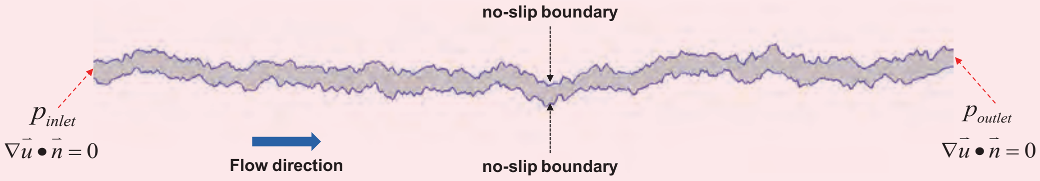

Conclusions

This work provides a high-resolution, micro-continuum approach to explore the matrix fracture interaction and further quantify the leakage influence on the hydraulic properties of rock fractures. We can summarize the main findings as:

- Fracture roughness and inertia show a significant effect on flow predictions for both fracture cases with impermeable and leaky walls.
- Eddies generally occur around locations with large asperities of sharp corners under high *Re* conditions. The existence of eddies reduces fracture hydraulic properties by narrowing the effective flow channel.
- The matrix fracture interaction makes the pressure contours showing significant fluctuation from the linear trend near the fracture profile areas.
- The matrix fracture leakage easily takes place for cases with high matrix permeability, high fracture roughness, and low *Re* values.
- The leakage phenomena takes place bidirectionally, where inflow and outflow are possible between the matrix and fracture.

Future work will focus on developing an analytical model for estimating the permeability of fractured rocks (matrix + fracture) to avoid expensive computation cost via high-resolution extended DBS equations.

Appendix A: Mixed Finite Element Formulation for NS Equations

Consider that the steady-state of incompressible, Newtonian flow with no gravity effects, and the full-physics NS equations can be given as:

$$\rho\left(\vec{u}\bullet\nabla\vec{u}\right)=-\nabla p+\mu\nabla^2\vec{u}$$
$$\nabla\bullet\vec{u}=0 \qquad \text{A1}$$

In the above equation, ρ is fluid density, $\vec{u}$ is velocity vector, p is pressure, and μ is fluid viscosity.

No-slip boundary conditions are assigned to the rough fracture walls, and pressure values are imposed at the inlet and outlet of the fracture, Fig. A1. The gradient of velocity in the direction of the pressure gradient is set to zero to guarantee the fully developed flow and to avoid the inlet effect.

The NS equations can be formulated in a mixed variational form, where the velocity and the pressure, are approximated simultaneously. Multiplying Eqn. A1 by the test function $\left(\vec{v},q\right)$ and integrating the resulting equations over the domain Ω yields:

$$\int_\Omega \rho\left(\vec{u}\bullet\nabla\vec{u}\right)\bullet\vec{v}dx=\int_\Omega\left(-\nabla p\right)\bullet\vec{v}dx+$$
$$\int_\Omega\left(\mu\nabla^2\vec{u}\right)\bullet\vec{v}dx$$
$$\int_\Omega\left(\nabla\bullet\vec{u}\right)qdx=0 \qquad \text{A2}$$

Applying the integration by parts technique, we have:

$$\int_\Omega\left(-\nabla p\right)\bullet\vec{v}dx=\int_\Omega p\nabla\bullet\vec{v}dx-\int_{\partial\Omega}p\vec{v}\bullet\vec{n}ds$$
$$\int_\Omega\left(\mu\nabla^2\vec{u}\right)\bullet\vec{v}dx=-\mu\int_\Omega\nabla\vec{u}:\nabla\vec{v}dx+\mu\int_{\partial\Omega}\nabla\vec{u}\bullet\vec{n}\vec{v}ds \qquad \text{A3}$$

Using the abstract framework, we have a problem to find $\left(\vec{u},p\right)\in W$ such that:

$$a\left(\left(\vec{u},p\right),\left(\vec{v},q\right)\right)=L\left(\left(\vec{v},q\right)\right) \qquad \text{A4}$$

For all $\left(\vec{v},q\right)\in W$, where:

$$a\left(\left(\vec{u},p\right),\left(\vec{v},q\right)\right)=\rho\int_\Omega\left(\vec{u}\bullet\nabla\vec{u}\right)\bullet\vec{v}dx-$$
$$\int_\Omega p\nabla\bullet\vec{v}dx+\mu\int_\Omega\nabla\vec{u}:\nabla\vec{v}dx+\int_\Omega\left(\nabla\bullet\vec{u}\right)qdx \qquad \text{A5}$$

$$L\left(\left(\vec{v},q\right)\right)=-\int_{\partial\Omega_N}p_{inlet}\vec{v}\bullet\vec{n}ds-\int_{\partial\Omega_N}p_{outlet}\vec{v}\bullet\vec{n}ds \qquad \text{A6}$$

The space W should be a mixed function space: $W = V\times Q$ such that $u\in V$ and $q\in Q$.

Acknowledgments

The authors would like to thank Saudi Aramco for funding this research. We would also like to thank King Abdullah University of Science and Technology (KAUST) for providing the license for MATLAB®.

References

1. Brush, D.J. and Thomson, N.R.: "Fluid Flow in Synthetic Rough Walled Fractures: Navier-Stokes, Stokes, and Local Cubic Law Simulations," *Water Resources Research*, Vol. 39, Issue 4, April 2003.

2. Zimmerman, R.W. and Yeo, I-W.: "Fluid Flow in Rock Fractures: From the Navier-Stokes Equations to the Cubic Law," chapter in *Dynamics of Fluids in Fractured*

Rock, Vol. 122, 2000, pp. 213-224.

3. Brown, S.R.: "Fluid Flow through Rock Joints: The Effect of Surface Roughness," *Journal of Geophysical Research*, Vol. 92, Issue B2, February 1987, pp. 1337-1347.

4. Konzuk, J.S. and Kueper, B.H.: "Evaluation of Cubic Law-Based Models Describing Single-Phase Flow through a Rough Walled Fracture," *Water Resources Research*, Vol. 40, Issue 2, February 2004, pp. 1-17.

5. Witherspoon, P.A., Wang, J.S.Y., Iwai, K. and Gale, J.E.: "Validity of Cubic Law for Fluid Flow in a Deformable Rock Fracture," *Water Resources Research*, Vol. 16, Issue 6, December 1980, pp. 1016-1024.

6. Renshaw, C.E.: "On the Relationship between Mechanical and Hydraulic Apertures in Rough Walled Fractures," *Journal of Geophysical Research*, Vol. 100, Issue B12, December 1995, pp. 24629-24636.

7. Unger, A.J.A. and Mase, C.W.: "Numerical Study of the Hydromechanical Behavior of Two Rough Fracture Surfaces in Contact," *Water Resources Research*, Vol. 29, Issue 7, July 1993, pp. 2101-2114.

8. Walsh, J.B.: "Effect of Pore Pressure and Confining Pressure on Fracture Permeability," *International Journal of Rock Mechanics and Mining Sciences & Geomechanics Abstracts*, Vol. 18, Issue 5, October 1981, pp. 429-435.

9. Zimmerman, R.W. and Bodvarsson, G.S.: "Hydraulic Conductivity of Rock Fractures," *Transport in Porous Media*, Vol. 23, Issue 1, January 1996, pp. 1-30.

10. Waite, M.E., Ge, S. and Spetzler, H.: "A New Conceptual Model for Fluid Flow in Discrete Fractures: An Experimental and Numerical Study," *Journal of Geophysical Research: Solid Earth*, Vol. 104, Issue B6, June 1999, pp. 13049-13059.

11. Wang, L., Cardenas, M.B., Slottke, D.T., Ketcham, R.A., et al.: "Modification of the Local Cubic Law of Fracture Flow for Weak Inertia, Tortuosity, and Roughness," *Water Resources Research*, Vol. 51, Issue 4, April 2015, pp. 2064-2080.

12. Brown, S.R., Stockman, H.W. and Reeves, S.J.: "Applicability of the Reynolds Equation for Modeling Fluid Flow between Rough Surfaces," *Geophysical Research Letters*, Vol. 22, Issue 18, September 1995, pp. 2537-2540.

13. Mourzenko, V.V., Thovert, J-F. and Adler, P.M.: "Permeability of a Single Fracture; Validity of the Reynolds Equation," *Journal de Physique II*, Vol. 5, Issue 3, March 1995, pp. 465-482.

14. Ge, S.: "A Governing Equation for Fluid Flow in Rough Fractures," *Water Resources Research*, Vol. 33, Issue 1, January 1997, pp. 53-61.

15. Oron, A.P. and Berkowitz, B.: "Flow in Rock Fractures: The Local Cubic Law Assumption Reexamined," *Water Resources Research*, Vol. 34, Issue 11, November 1998, pp. 2811-2825.

16. Nicholl, M.J., Rajaram, H., Glass, R.J. and Detwiler, R.: "Saturated Flow in a Single Fracture: Evaluation of the Reynolds Equation in Measured Aperture Fields," *Water Resources Research*, Vol. 35, Issue 11, November 1999, pp. 3361-3373.

17. Basha, H.A. and El-Asmar, W.: "The Fracture Flow Equation and its Perturbation Solution," *Water Resources Research*, Vol. 39, Issue 12, December 2003, pp. 1-15.

18. Crandall, D., Ahmadi, G. and Smith, D.H.: "Computational Modeling of Fluid Flow through a Fracture in Permeable Rock," *Transport in Porous Media*, Vol. 84, Issue 2, January 2010, pp. 493-510.

19. Popov, P., Qin, G., Bi, L., Efendiev, Y., et al.: "Multiphysics and Multiscale Methods for Modeling Fluid Flow through Naturally Fractured Carbonate Karst Reservoirs," *SPE Reservoir Evaluation & Engineering*, Vol. 12, Issue 2, April 2009, pp. 218-231.

20. Logg, A., Mardal, K-A. and Wells, G.: *Automated Solution of Differential Equations by the Finite Element Method: The FEniCS Book,* Series Vol. 84, Springer, 2012, 731 p.

About the Authors

Xupeng He

M.S. in Petroleum Engineering, King Abdullah University of Science and Technology

Xupeng He is currently a Ph.D. student at the Ali I. Al-Naimi Petroleum Engineering Research Center, King Abdullah University of Science and Technology (KAUST), Thuwal, Saudi Arabia. His research interests include modeling naturally fractured reservoirs, machine (deep) learning applications in petroleum engineering, and uncertainty quantification and optimization in subsurface flow problems.

Xupeng is the author of 11 conference papers, and two U.S. patents.

He was the recipient of the Excellent Student Cadre and the Outstanding Undergraduate Student Awards in 2014 and 2015, respectively, at Chang'an University. Also, Xupeng received a national scholarship from the Ministry of Education of the People's Republic of China in 2012 and 2013.

He received his B.S. degree in Resource Exploration Engineering (Oil and Gas) from Chang'an University, Xi'an, China, in 2015. Xupeng received his M.S. degree in Petroleum Engineering from KAUST in 2018.

Marwah M. AlSinan

M.S. in Petroleum Engineering, Imperial College

Marwah M. AlSinan joined Saudi Aramco in 2013 as a Petroleum Engineer, working with the Reservoir Engineering Technology Division in the Exploration and Petroleum Engineering Center – Advanced Research Center (EXPEC ARC).

Her research interests include multiphase flow in fractures, carbon dioxide sequestration, and applications of nuclear magnetic resonance in porous media.

In 2013, Marwah received her B.S. degree in Petroleum and Natural Gas Engineering from Pennsylvania State University, State College, PA. She received her M.S. degree in Petroleum Engineering from Imperial College, London, U.K. in 2017.

Dr. Hyung T. Kwak

Ph.D. in Physical Chemistry, Ohio State University

Dr. Hyung T. Kwak joined Saudi Aramco in April 2010 as a Petroleum Engineer with Saudi Aramco's Exploration and Petroleum Engineering Center – Advance Research Center (EXPEC ARC). He had been a member of the Pore Scale Physics focus area (2010 to 2012) and SmartWater Flooding focus area (2013 to 2014) of the Reservoir Engineering Technology Division. Currently, Hyung is a focus area champion of the Pore Scale Physics focus area. His main research focus is seeking deeper understanding of fluid-rock interaction in pore scale of the Kingdom's reservoirs.

Since joining Saudi Aramco in 2010, Hyung has been involved with various improved oil recovery and enhanced oil recovery (EOR) research projects, such as SmartWater Flooding, carbon dioxide EOR, and chemical EOR. Prior to joining Saudi Aramco, Hyung was a Research Scientist at Baker Hughes, with a main area of research related to nuclear magnetic resonance (NMR)/magnetic resonance imaging technology.

In 1996, Hyung received a B.S. degree in Chemistry from the University of Pittsburgh, Pittsburgh, PA, and in 2001, he received his Ph.D. degree in Physical Chemistry from Ohio State University, Columbus, Ohio.

Before moving into the oil and gas industry, Hyung was involved — as a postdoctoral fellow for 2 years — in a project developing the world's largest wide bore superconducting magnet NMR spectrometer, 900 MHz, at the National High Magnetic Field Laboratory.

He has more than 100 publications, including peer-reviewed articles and patents.

Dr. Hussein Hoteit

Ph.D. in Applied Mathematics, University of Rennes 1

Dr. Hussein Hoteit is an Associate Professor in Reservoir Engineering and the Program Chair of Energy Resources and Petroleum Engineering (ERPE) at King Abdullah University of Science and Technology (KAUST), Thuwal, Saudi Arabia.

Before joining KAUST, Hussein worked for ConocoPhillips and Chevron Companies for about 12 years, where he conducted projects related to chemical enhanced oil recovery (EOR), CO_2 EOR, steam flood, EM heating, to name a few.

Hussein's current research includes chemical EOR, geological CO_2 storage, improved oil recovery optimization, data-driven machine learning, and reservoir simulation development.

He has earned several Society of Petroleum Engineers (SPE) awards, including SPE Distinguished Lecturer in 2009, and served as Associate Editor for the *SPE Journal* for more than 10 years.

Hussein received his B.S. degree in Pure Mathematics and Computer Sciences from Lebanese University, Lebanon, M.S. and Ph.D. degrees in Applied Mathematics from the University of Rennes 1, Rennes, France.

Improve Oil Production from Tar Impacted Reservoirs Using In Situ Steam Generation and Ionic Liquids

Ayman R. Al-Nakhli, Hussain A. Aljeshi, Dr. Olalekan Alade and Dr. Mohamed Mahmoud

Abstract /

One of the typical production challenges is occurrence of impermeable layers of highly viscous asphaltenic oil (known as tarmat) at the oil/water contact point within a reservoir. Tar forms a physical barrier that isolates the producing zones from the aquifer or water injectors. Tar occurs as a rapid pressure decrease that can be observed in such reservoirs, increasing the number of dead wells, thereby declining productivity. Another indirect consequence of tar presence is poor sweep efficiency that leads to water cut increase by a drastic magnitude.

An innovative approach was developed to establish better sweep efficiency, transmissibility, and pressure maintenance of tar impacted areas using thermochemical treatment. The treatment consists of injecting exothermic reaction components that react downhole and generate in situ pressure and heat. The in situ reaction products provide heat- and gas-driven energy to mobilize tar, improve sweep efficiency, and maintain flooding for better pressure maintenance. Typically, downhole heat generation through chemical reaction releases substantial heat, which could be employed in various thermal stimulation operations. Nano/ionic liquids, high pH solutions, solvents, and nanometals were combined with the exothermic reaction to improve tar mobilization.

Based on lab testing, the new technology showed more recovery than conventional steam flooding. Permeable channels were created in a tar layer with sandback samples, which enhanced transmissibility, pressure support, and sweep efficiency. The effect of thermochemical treatment and ionic liquid on bitumen texture will be described. The impact of in situ generated heat on injectivity will also be presented.

This novel method will enable commercial production from tar impacted reservoirs and avoid costly steam flooding systems.

The developed novel treatment relates to in situ steam generation to maximize heat delivery efficiency of steam into the reservoir and to minimize heat losses due to underburdens and/or overburdens. The generated in situ steam and gas can be applied to recover deep oil reservoirs, which cannot be recovered with traditional steam, miscible gas, or polymer injection methods.

Introduction

Several oil reservoirs around the world include the presence of tarmats, which could impact oil production. The presence of tarmats creates a great challenge for oil operators as tarmats can limit the injectivity of wells, sweep efficiency, pressure maintenance of the reservoir, and overall oil production. When tar exists as a batch occurrence in the reservoir, it makes it very difficult for well placement, and requires effective stimulation for such reservoir to maximize oil production without significant capital cost, as for steam flooding.

A typical production challenge is the occurrence of impermeable layers of highly viscous asphaltenic oil (known as tarmat or bitumen) at the oil/water contact within a reservoir. Tar forms a physical barrier that isolates producing zones from the aquifer or water injectors that restricts the reservoir pressure support through the primary recovery stage of the reservoir[1]. As a result, a rapid pressure decrease can be observed in such reservoirs, with an increasing number of dead wells and declining productivity.

The problem of tar being present can be more complex when the tar in the field is patchy and is randomly distributed in the reservoir. Sometimes, the variation of vertical, and lateral distribution of tar within the reservoir, in addition to the presence of fractures in the field, adds more difficulties and challenges to the reservoir characterization and waterflooding planning.

Core studies demonstrated some observations about the manner of tar occurrence and its relation to lithology and pore structure. In general, there is no steady transition from oil to heavier oil to tar. Instead, oil and tar, as two separate phases, occur simultaneously in different proportions within the same reservoir[2].

The variation of depositional characteristics also makes it more difficult to understand and deal with the tarmats within the reservoir. In some cases, the tar deposition is permeable while in other cases the tar zone is impermeable. Sometimes the tar at the base of the reservoir shows a continuous increase in asphaltenes from the oil zone above the tar, and sometimes it shows a sharp, discontinuous increase in asphaltene content from the oil zone to the tarmat. Tar could also be deposited throughout the entire producing well or deposited only at the bottom part of the producing interval[3]. All of these variables must be taken into consideration when dealing with tar as they lead to another indirect consequence, which is poor sweep efficiency that causes the water cut to increase by a drastic magnitude.

Tarmats are found in many major oil fields in the world. The thickness of the tarmat varies from one place to another of the same reservoir. Sometimes, the thickness of tarmats reaches a few hundred feet; while their extent can spread several kilometers[4, 5].

Tarmat zones, which have additional bitumen or heavy oil, have an in situ viscosity of more than 10,000 centipoise (cP) and gravity below 10° API. Usually, the tarmat is found at the bottom of the oil column. Tarmats normally are carbon based. They consist of 100 to 300 atoms/molecules of sulfur, oxygen, nitrogen, hydrogen, and fractions of nickel and vanadium[3]. So, they can be found in any range from highly viscous hydrocarbon fluids to near solid materials. According to several geochemical studies presented by various researchers, tarmats can be formed as a result of different processes; such as water washing, natural deasphalting, biodegradation, and gravity segregation, which makes grade changes in the composition and distinction in depth. It is very important to know that field experience shows that some tarmats may become mobile depending on reservoir conditions, and the tar viscosity when moderate differential pressure is applied[4].

In the literature, several studies and experiments have been conducted to study the treatment and mobilization of tar to improve the reservoir recovery or to recover oil from the tarmat layer itself. This includes the effect of cold water injection, hot water injection, and using solvents[3]. In their study of tar mobilization utilizing non-thermal methods, Sarbar and Alqam (1995)[6], showed that injection of 1 wt% sodium hydroxide in water displayed an optimum effect on mobilizing both soluble and insoluble tar material from the core samples, and significantly enhanced the permeability.

Acidizing core samples, which contain large quantities of tar material, did not improve the permeability as this caused the migration of some tar material, which was released by the dissolution of the rock matrix. This then acted as a pore blocking material, since tar is not soluble in injected acid solution[6].

Concept

In this study, an innovative approach was developed to establish better sweep efficiency and transmissibility, and improve pressure maintenance of tar impacted reservoirs, using thermochemical fluids. The treatment consists of injecting exothermic reaction components that react downhole to generate in situ pressure and heat. Solvents, nanomaterial, and ionic liquids were used to improve tar disintegration.

The in situ reaction products provide gas drive energy to mobilize tar, improve sweep efficiency, and maintain flooding for better pressure maintenance, Fig. 1. Typically, downhole heat generation through chemical reaction releases substantial heat, which could be employed in various thermal stimulation operations. Nano/ionic liquids, high pH solutions, solvents, and nanometals were combined with the exothermic reaction to improve tar mobilization.

Based on lab testing, the new technology showed more recovery than conventional steam flooding. Permeable channels were created in a tar layer with sandback samples, which enhanced transmissibility, pressure support, and sweep efficiency. The effect of thermochemical treatment and ionic liquid on bitumen texture will be described. The impact of in situ generated heat on injectivity will also be presented.

This novel method will enable commercial production

Fig. 1 *An illustration of the conceptual design of thermochemical fluid injection for heavy oil production.*

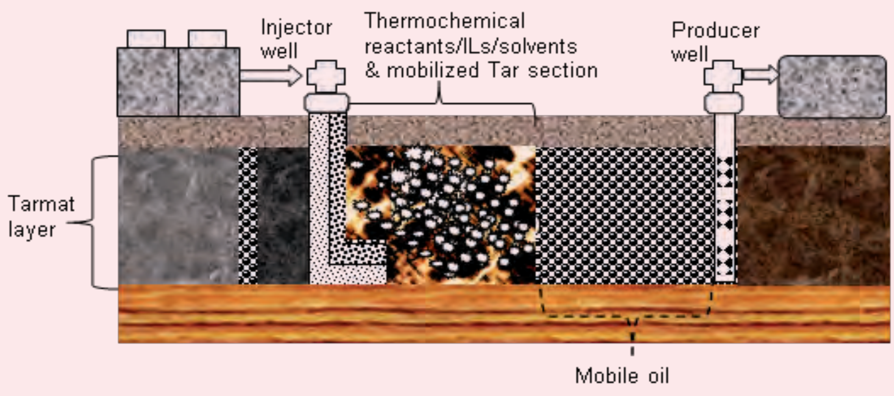

Fig. 2 The typical range of enhanced oil recovery technology applications[7].

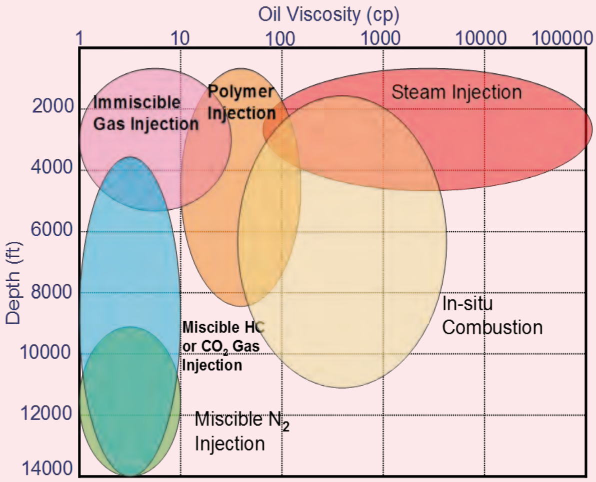

Fig. 3 Autoclave systems rated up to 10,000 psi.

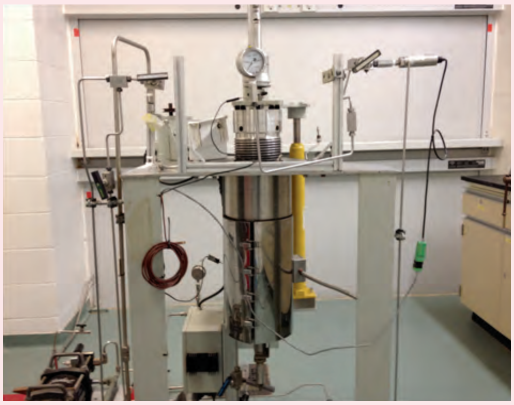

Fig. 4 The exothermic reaction in the autoclave system.

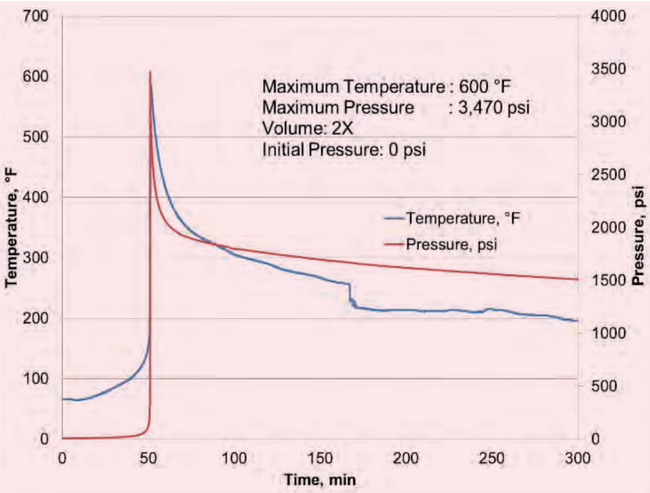

from tar impacted reservoirs, and avoid costly steam flooding systems. The developed novel treatment relates to in situ steam generation to maximize heat delivery efficiency of steam into the reservoir and to minimize heat losses due to underburdens and/or overburdens and nonproducing areas. The generated in situ steam and gas can be applied to recover deep oil reservoirs, which cannot be recovered with traditional steam injection methods.

Results and Discussion

The presence of patchy tar in a reservoir interrupts oil production, sweep efficiency, and pressure maintenance, leaving a significant amount of unproduced oil. Figure 2 shows the typical range of enhanced oil recovery technology applications. There is no existing technology that is suitable for tar impacted and deep reservoirs, except in situ combustion; however, this is not very attractive from a safety point of view. A novel thermochemical fluid treatment recipe was developed to treat such reservoirs. The new treatment generates in situ heat and gas drive to improve waterflooding in tar impacted reservoirs.

The main advantage of the new system is that it is independent of the reservoir depth. Heat and gas will be generated in situ, so no heat will be lost in the overburden, as is the case with steam flooding. The exothermic reaction can be spotted near the wellbore or deep into the reservoir to treat the tar presence and improve waterflooding.

A high-pressure, high temperature reactor (an autoclave system), in an explosion proof room, was used to conduct laboratory testing of the exothermic reactions, Fig. 3. Thermochemical fluid was placed in the reactor and activated. Once the reaction took place, the reactor temperature increased from 75 °F to 600 °F, while the pressure increased from zero to 3,470 psi, Fig. 4.

Tar Viscosity with Thermochemical Fluid

Table 1 lists the properties of a semi-solid tar sample that was used in this study, along with the saturations, resin, and armoatics fractions. An Anton-Paar viscometer, Fig. 5, was used to measure the viscosity of the sample, along with the thermochemical fluid reaction. The sample was placed in a high-pressure cell, rated up to 5,000 psi and 500 °F. Thermochemical reagents were added to the cell, and viscosity was measured at different temperatures while the reaction was taking place. The cell temperature increased from room temperature to 220 °F, while the tar viscosity was reduced from 5,800 cP to 700 cP, Fig. 6.

As this reaction is reversible, solvents were also used along with thermochemical reagents to dissolve the organic content and maintain low viscosity of the treated tar, which will minimize any impact on production lines and downstream facilities upon production. When solvents were used along with thermochemical reagents, viscosity dropped to 5 cP.

Flooding Tar with Steam vs. Thermochemical Fluid

The main objective of this study was to create permeable channels through the tar layer, which will improve

Table 1 Properties of tar, saturations, resin, and aromatics fractions.

Pour point (°C)	10
Flash point (°C)	71
Sulfur content (%wt)	3.25
Carbon content (%)	81.8
Hydrogen content (%)	11.8
Nitrogen content (%)	0.25
Saturations, resin and aromatics	
Saturates (%wt/wt)	32.77
C_7 soluble asphaltene (%wt/wt)	25.8
Resin (%wt/wt)	9.06
Aromatics (%wt/wt)	32.37

water injection in tar impacted reservoirs, maintain pressure maintenance, and improve sweep efficiency, and overall enhance light oil production. A coreflood system, Fig. 7, was used to treat the tar sample with thermochemical fluid and compare the results with the effect of flooding with supersteam quality. Thermochemical fluid was injected at 212 °F, as a typical reservoir temperature. Steam was injected at 392 °F. Post-treatment, tar samples were analyzed using a scanning electron microscope (SEM).

Figure 8 shows the original tar sample (B_0), post-steam flooding (B_1), and post-thermochemical fluid treatment (B_2). The original tar sample image does not show any cavity nor suspended water droplets. With steam flooding, suspended water droplets are noticeable; however, with no created channels through the tar sample. The results showed that channels where created through a tar sample, when thermochemical fluid treatment was used. Suspended water droplets were also noticed post-thermochemical fluid treatment.

Gas Chromatography (GC) and Thermal Decomposition

Pretreatment samples of tar, post-treatment with steam and with thermochemical fluid, were sent for thermal gravimetric analyzer (TGA) analysis and gas chromatography (GC) analysis. During the TGA testing, the samples were exposed to elevated temperatures to measure weight loss, due to thermal decomposition, at a fixed heating rate and a gas injection rate of 30 °C/min and 50 ml/min, respectively.

TGA analysis showed a remarkable difference when the tar sample was treated with thermochemicals (B_2) compared to the original sample and steam treated sample (B_0 and B_1, respectively), which followed closely similar trends. Figure 9 shows the TGA and the differential TGA (DTGA) results with regard to the sample weight. The TGA results, which is the weight loss

Fig. 5 The Anton Paar viscometer used in the test.

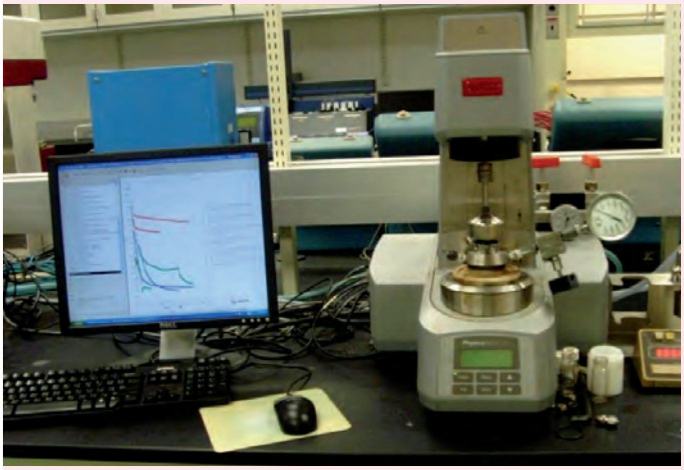

Fig. 6 The tar viscosity during thermochemical reaction.

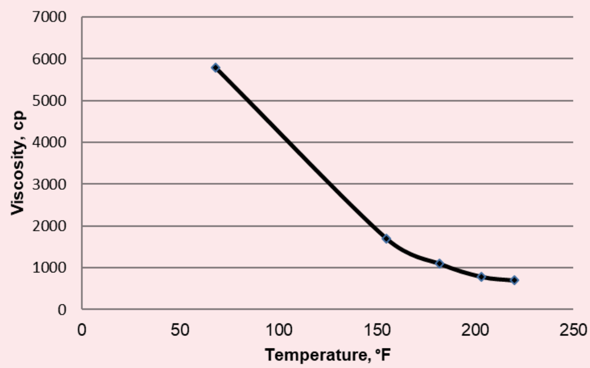

Fig. 7 *The coreflood system, with tar, and thermochemical fluids.*

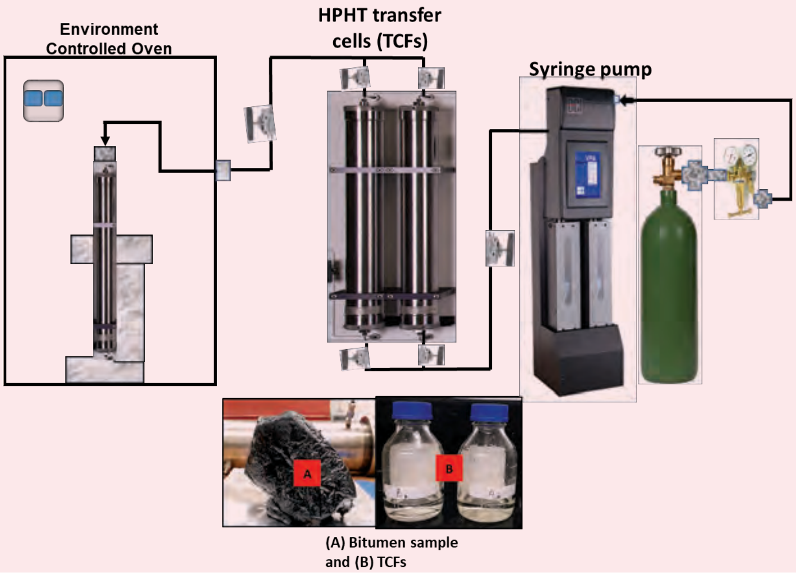

Fig. 8 *The SEM-EDX images of the original tar sample (B_0), post-steam treated sample (B_1), and the post-thermochemical fluid treated sample (B_2).*

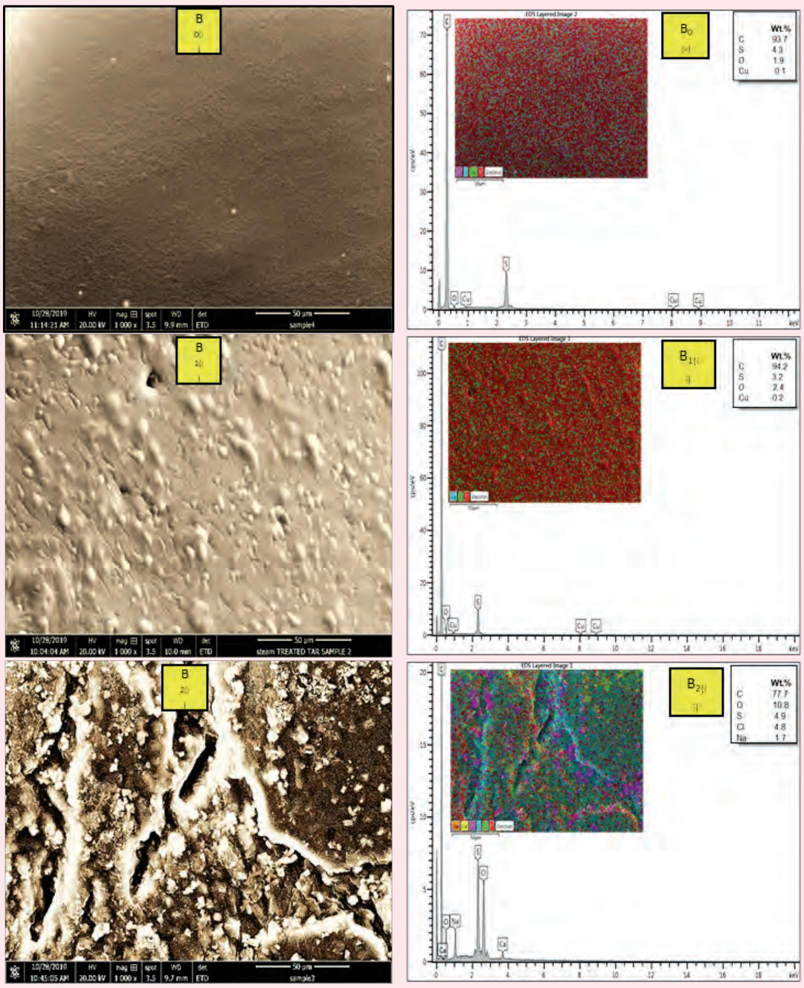

Fig. 9 *The TGA and DTGA of tar sample (B_0), steam treated (B_1), and thermochemical treated (B_2).*

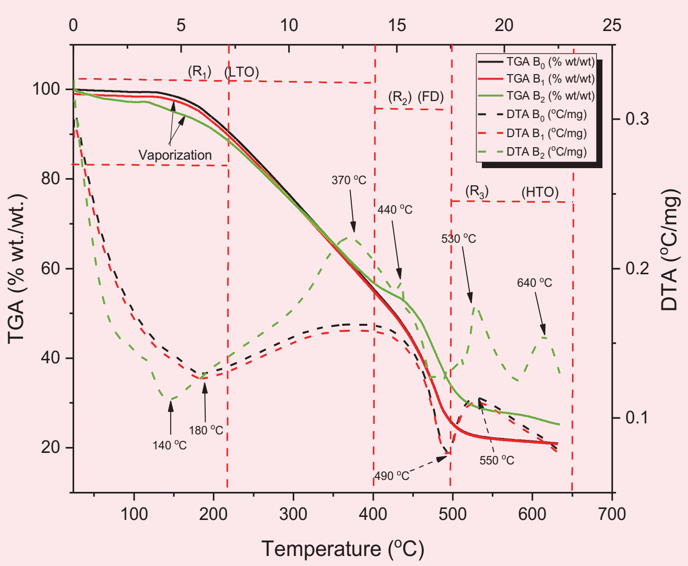

vs. temperature, are shown as solid lines. The DTGA, which is the change of weight loss vs. temperature, is shown as dashed lines.

There were three exothermic reaction peaks at elevated temperatures of 370 °C, 530 °C, and 640 °C, with the thermochemical fluid treated tar sample. These peaks were absent in the original tar and stream treated sample. This could suggest some hydrocarbon cracking took place during thermochemical fluid flooding. So, the created channels were due to cracking rather than mechanical displacement. Therefore, higher combustion activity was observed in the thermochemical fluid treated sample.

The GC analysis showed a significant shift of hydrocarbon

Fig. 11 *Molecular dynamic model of tar thermochemical fluid interface.*

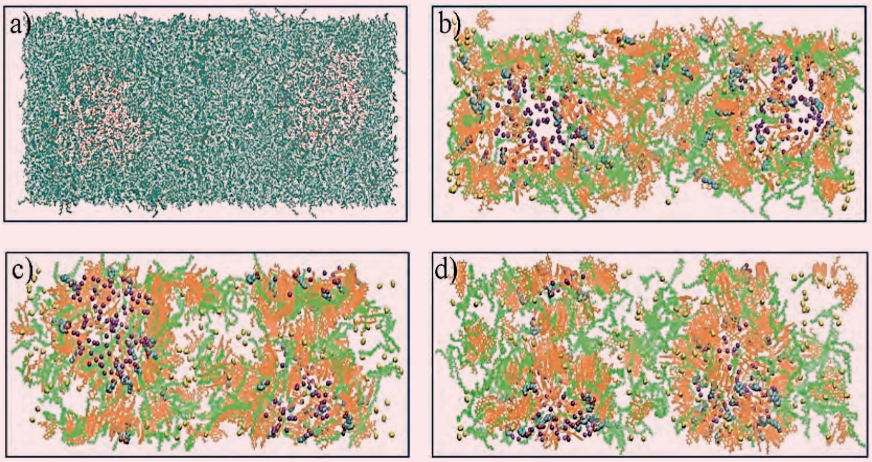

Fig. 10 *The GC analysis of the hydrocarbon fractions of the bitumen sample (a) before, and (b) after thermochemical fluid pretreatment.*

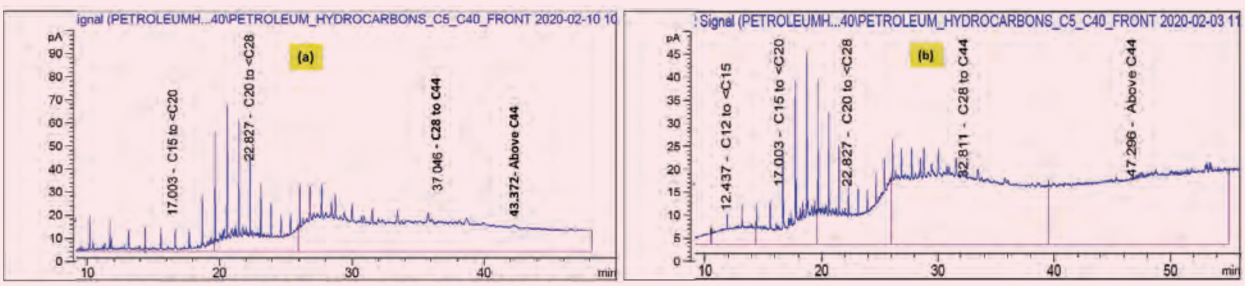

cuts toward light components; 12% of the sample was converted from C-12 to C-15, which were not existing in the original sample, nor in the steam treated sample, Fig. 10. This could support the idea of thermal cracking of hydrocarbon during thermochemical fluid treatment. A larger content of heavy cuts was also observed in the post-thermochemical fluid treatment.

Molecular Dynamic Simulation of Tar Thermochemical Fluid Interfacial Interaction

Figure 11 shows the model, which was built with two droplets of thermochemical fluid solution (red), surrounded by tar (green). The simulations were conducted at 300 K and 373 K. The objective of this simulation is to investigate fluid interface and interactions between thermochemical fluid and tar. The effect of heat generated by thermochemical fluid on molecular interactions and tar texture was investigated.

The simulation results revealed that polar molecules of the tar (asphaltene) prefer to interact with the aqueous phase of thermochemical fluid and create stable microemulsion. The created microemulsion breaks the tar matrix and increases its mobility. Generated heat by thermochemical fluid reaction helped to distribute the emulsion in the tar sample. So, a more homogenous sample containing microemulsion is created, Figs. 12a and 12b.

Heat generation by thermochemical fluid helped the aqueous phase to penetrate into the tar matrix; therefore, it broke the complex structure and interaction of heavy hydrocarbon components. Moreover, it was also observed that generated heat resulted in more homogenous distribution of saturates and aromatic components. Generated nitrogen gas by thermochemical fluid also resulted in disturbance of tight interactions of the large molecules of the tar matrix; therefore, it enhanced mobility. So, as a result of treating tar with thermochemical fluid, viscosity was reduced due to large molecule segregation, and mobility was increased due to homogenous microemulsion creation[8].

Thermochemical Fluid vs. Steam for Heavy Oil Recovery

A coreflood system, Fig. 13, was used to study steam

Fig. 12 *A 2D density map of water at 300 K and 373 K (a), and asphaltene at 300 K and 373 K (b).*

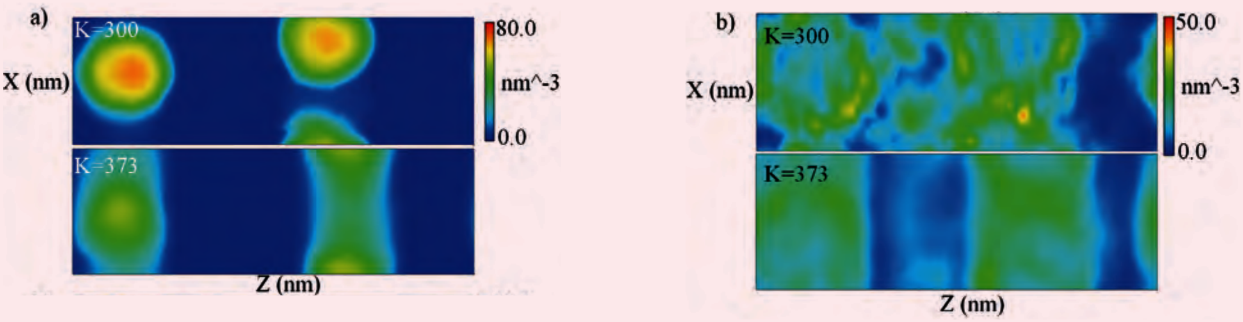

Fig. 13 *Setup for the steam and thermochemical fluid flooding experiments.*

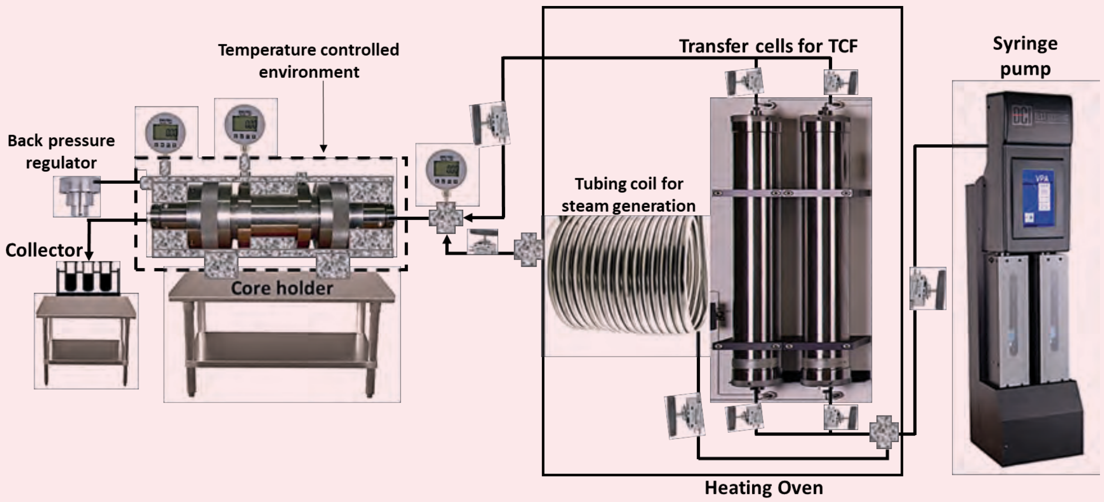

Fig. 14 *Recovery performance from steam vs. thermochemical fluid injection.*

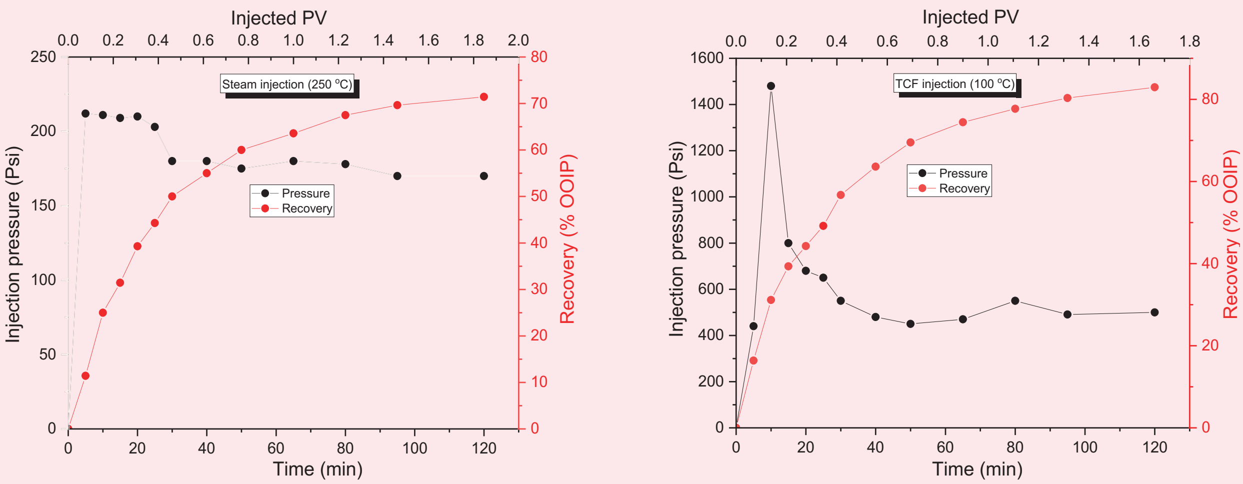

flooding vs. thermochemical flooding for heavy oil recovery. Brea sandstone cores with equal porosity (20) and permeability (120 mD) were used for this study. Cores was initially saturated with heavy oil by injecting the oil at 0.25 ml/min at 160 °F. Then, steam was generated in the oven and injected to the core holder at 480 °F, which gives 98% steam quality.

Oil recovery was measured with time, Fig. 14. The results showed that supersteam quality at 480 °F recovered up to 71% after the injection of 1.75 pore volumes (PV). The inlet pressure increased up to 212 psi during injection. During the thermochemical fluid flooding, on the heavy oil saturated core, the oven temperature was set at 212 °F, as a typical reservoir temperature. The results showed that thermochemical fluid recovered up to 83%, with a total of 1.67 PV of the fluid injected, Fig. 14. In situ generated pressure, due to exothermic reaction and nitrogen gas generation, reached up to 1,480 psi. The generated pressure also confirmed the activation of the reaction in situ.

First Field Application

Prior to going to the field, a treatment recipe was tested on the bench for QA/QC. The asphaltene sample was placed above the water layer in a graduated cylinder, at a room temperature of 70 °F, Fig. 15a. The asphaltene sample was collected from refinery vacuum gasoil. Then, thermochemical fluid was poured on the sample. Upon the activation of the thermochemical reaction using an activator, the thermochemical fluid is defused inside the asphaltene layer and resulted in reduced viscosity, Figs. 15b and 15c. The overall fluid temperature increased up to 195 °F, due to the thermochemical reaction.

Fig. 15 *Lab testing of thermochemical fluid treatment with asphaltene.*

(a) Tar layer above water

(b) Start of thermochemical reaction

(c) Reaction completed and tar dissolved

Fig. 16 Field treatment using an in situ steam generating system.

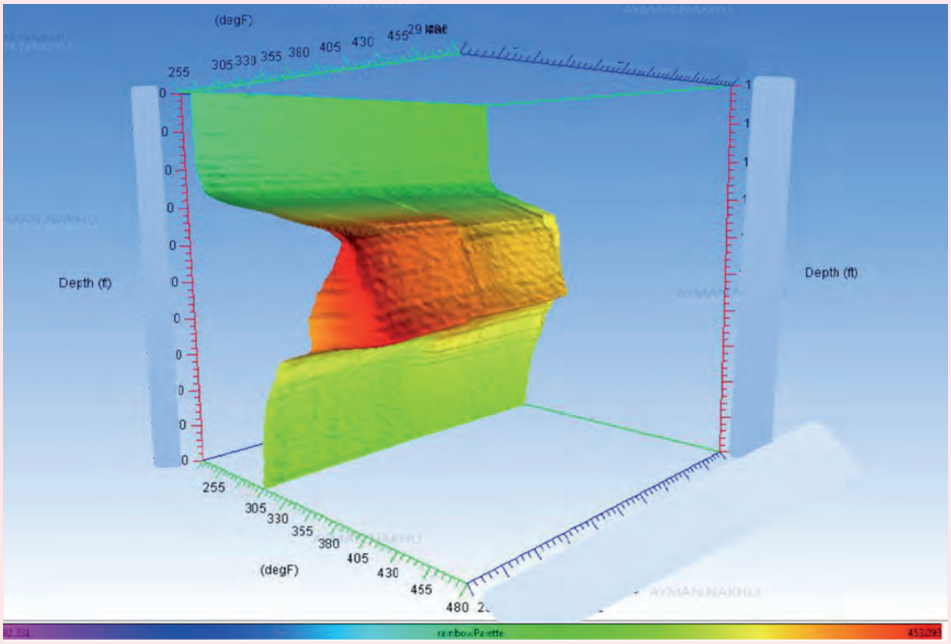

Fig. 17 Well treatment data during thermochemical fluid injection.

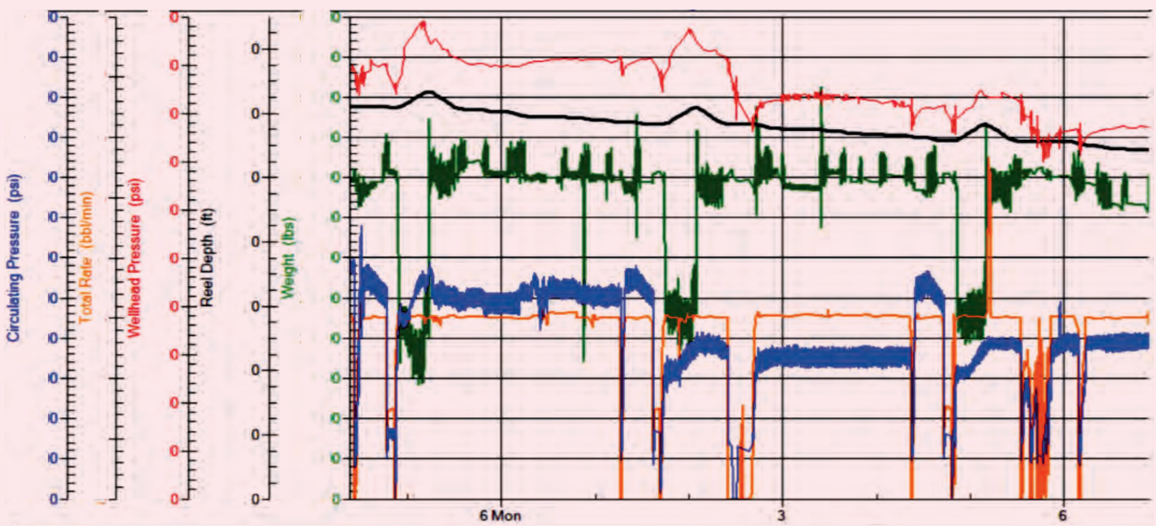

The treatment recipe was extensively tested in the lab to ensure compatibility with reservoir brine, pressure, and temperature. The job was designed to be conducted without flowing back to avoid any tar precipitation in the downstream flow lines. The selected well is a horizontal water injector in batch tar reservoirs. The recipe was designed to use in situ to generate heat to improve the water injectivity of the well.

The well's pretreatment injectivity was measured. Then, the in situ steam generation system was pumped in stages until the whole interval was treated. Active coiled tubing was used during the treatment to show in situ heat generation to control the pumping rate, reaction time, and heat flooding, Fig. 16. Controlling the flooding rate was very helpful to avoid exposing downhole completion to an elevated temperature while squeezing the generated exothermic reaction deep into the reservoir. Generated heat was measured up to 480 °F at the reservoir interval.

During the thermochemical fluid pumping, the wellhead pressure significantly decreased, Fig. 17. After completing the job, operators rigged down, and connected the well to the injection line. The treatment increased the well injectivity by as much as sixfolds of the original injectivity. The system was more cost-effective compared to the capital cost of steam flooding.

Conclusions

1. Flooding a tar sample with thermochemical fluid showed that channels where created through the sample. No channels occurred once the sample was flooded with supersteam quality.
2. Created channels through the tar layer will help with improving sweep efficiency, pressure maintenance, and oil production from tar impacted layers.
3. A field trial test of thermochemical fluid treatment in a tar impacted area showed a successful stimulation with a sixfold increase in well injectivity.
4. Treating tar with the newly developed exothermic reaction recipe showed that homogenous microemulsion is created in the tar texture.
5. Generated byproduct slots due to the exothermic reaction increased the interaction of asphaltene molecules and brine, which therefore promoted microemulsion.
6. Diffusion of nitrogen gas resulted from the exothermic reaction, although tar matrix softens its texture and leads to disturbing the tight interaction between the tar matrix components. The localized nitrogen gas generation helped to dissolve the tar matrix.
7. As a result of treating tar with thermochemical fluid, viscosity was reduced due to segregation of large molecules, and mobility was increased due to homogenous microemulsion creation.
8. A novel thermochemical stimulation treatment was developed to enhance oil recovery from tar impacted reservoirs.
9. The new technology eliminates the need for costly capital cost of installing the steam flooding system.
10. The developed thermochemical fluid stimulation treatment generates in situ steam, gas, and solvents, while providing localized heat and flooding capability for the impacted intervals. Generating heat in situ eliminates heat loss in the overburden and underburden.
11. The measured heat generated in situ was up to 480 °F, which is equivalent to 99% steam quality.
12. TGA and GC analysis of tar samples in the study suggested cracking of heavy oil cuts due to thermochemical treatment, which needs further investigation.
13. Coreflood test of saturated Berea cores with heavy oil showed that thermochemical treatment had higher recovery by 12%, compared to steam quality of 98%.

References

1. Abu-Khamsin, S.A., Ayub, M., Al-Marhoun, M.A. and Menouar, H.: "Waterflooding in a Tarmat Reservoir Laboratory Model," *Journal of Petroleum Science and Engineering*, Vol. 9, Issue 3, June 1993, pp. 251-261.
2. Benedek, L., Ali, R., AlGhamdi, H. and Alhuthali, A.H.: "Tar Area Development in a Giant Carbonate Field in Saudi Arabia," SPE paper 172236, presented at the SPE Saudi Arabia Section Technical Symposium and Exhibition, al-Khobar, Saudi Arabia, April 21-24, 2014.
3. Mullins, O.C., Di Primio, R., Uchytil, S., Zuo, J.Y., et al.: "Bitumen and Tar Deposition and Tar Mat Formation Accounted for by Multiple Charging, Trap Filling and Fluid Geodynamics," SPE paper 181544, presented at the SPE Annual Technical Conference and Exhibition, Dubai, UAE, Spetember 26-28, 2016.
4. Almansour, A., Al-Bazzaz, W., Saraswathy, G., Sun, Y., et al.: "Investigation of the Physical and Chemical Genesis of Deep Tar-Mat Oil and Its Recovery Potential under Different Temperatures," SPE paper 170059, presented at the SPE Heavy Oil Conference-Canada, Alberta, Canada, June 10-12, 2014.
5. Okasha, T.M., Menouar, H.K. and Abu-Khamsin, S.A.: "Oil Recovery from Tarmat Reservoirs Using Hot Water and Solvent Flooding," *Journal of Canadian Petroleum Technology*, Vol. 37, Issue 4, April 1998, pp. 33-40.
6. Sarbar, M. and Alqam, M.: "Tar Mobilization Studies for a Carbonate Reservoir in Saudi Arabia," paper presented at the UNITAR International Conference on Heavy Crude and Tar Sands on Fueling for a Clean and Safe Environment, Houston, Texas, February 12-17, 1995.
7. Bizley, D.: "Repsol: Using EOR Methods to Unlock Offshore Oil," *Oil Field Technology*, July 2015.
8. Alade, O.S., Hamdy, M., Mahmoud, M., Al-Shehri, D.A., et al.: "Experimental and Numerical Analysis of Using Thermochemical Injection for Preheating to Improve in Situ Combustion of Bitumen," *Fuel*, Vol. 275, September 2020.

About the Authors

Ayman R. Al-Nakhli

M.S. in Entrepreneurship for New Business Development, Open University Malaysia

Ayman R. Al-Nakhli is a Petroleum Scientist in Saudi Aramco's Exploration and Petroleum Engineering Center – Advanced Research Center (EXPEC ARC), where he leads the research program on thermochemicals and develops technologies related to conventional and unconventional reservoirs such as pulse fracturing, stimulation, diverting agents, and heavy oil.

Ayman has developed and field deployed several novel technologies, with four of them being commercialized with international service companies. He received the World Oil Award for Best Production Chemical in 2015.

Ayman has filed more than 20 patents, published 35 journal papers, and 40 conference papers.

He received his B.S. degree in Industrial Chemistry from King Fahd University of Petroleum and Minerals (KFUPM), Dhahran, Saudi Arabia, and an M.S. degree in Entrepreneurship for New Business Development from Open University Malaysia, Bahrain.

Hussain A. Aljeshi

M.S. in Petroleum Engineering, Texas A&M University

Hussain A. Aljeshi is a Petroleum Engineer working with the Advanced Technical Services Division of Saudi Aramco's Exploration and Petroleum Engineering Center – Advanced Research Center (EXPEC ARC). He joined Saudi Aramco in 2002 as a Petrophysicist working in the Reservoir Description Division. Hussain has been involved in acoustic logging studies, and gained extensive knowledge throughout his career, including experience as a Drilling and Production Engineer.

Currently, Hussain is a member of the Special Core Analysis Team in the Petrophysical Studies Unit.

In 2002, he received his B.S. degree in Petroleum Engineering from King Fahd University of Petroleum and Minerals (KFUPM), Dhahran, Saudi Arabia, and in 2011, Hussain received his M.S. degree in Petroleum Engineering from Texas A&M University, College Station, TX.

Dr. Olalekan Alade

Ph.D. in Earth Resources Engineering, Kyushu University

Dr. Olalekan Alade joined the Department of Petroleum Engineering, College of Petroleum and Geosciences, King Fahd University of Petroleum and Minerals, (KFUPM), Dhahran, Saudi Arabia, in May 2018, as a Postdoctoral Fellow. He currently works as a Research Engineer at the Center for Integrative Petroleum Research (CIPR) of the College.

Olalekan's research interest spans the application of principles of chemical and petroleum engineering, including fluid dynamics, transport phenomenon, thermodynamics, and reaction engineering in solving various problems in the aspects of petroleum recovery, flow, and transportation.

In 2017, he received his Ph.D. degree in Earth Resources Engineering from Kyushu University, Fukuoka, Japan, with a specialty in heavy oil resources production and safety engineering.

Dr. Mohamed Mahmoud

Ph.D. in Petroleum Engineering, Texas A&M University

Dr. Mohamed Mahmoud is a Professor working in the Department of Petroleum Engineering at King Fahd University of Petroleum and Minerals (KFUPM), Dhahran, Saudi Arabia. His areas of research include carbonate and sandstone stimulation, formation damage, and rock petrophysics and geomechanics.

Mohamed has authored or coauthored several journal and conference papers, in addition to more than 80 U.S. patents.

He received both his B.S. degree and M.S. degree in Petroleum Engineering from Suez Canal University, Ismailia, Egypt. Mohamed received his Ph.D. degree in Petroleum Engineering from Texas A&M University, College Station, TX, in 2011.

Notes

Have an article you would like to publish? Here are our guidelines.

These guidelines are designed to simplify and help standardize submissions. They need not be followed rigorously. If you have any questions, please call us.

Length

Average of 2,500-4,000 words, plus illustrations/photos and captions. Maximum length should be 5,000 words. Articles in excess will be shortened.

What to send

Send text in Microsoft Word format via email. Illustrations/photos should be clear and sharp. Editable files are requested for graphs, i.e., editable in Excel.

Procedure

Notification of acceptance is usually within three weeks after the submission deadline. The article will be edited for style and clarity and returned to the author for review. All articles are subject to the company's normal review. No paper can be published without a signature at the manager level or above.

Format

No single article need include all of the following parts. The type of article and subject covered will determine which parts to include.

Working Title
Lorem Ipsum here.

Abstract
Usually 150-300 words to summarize the main points.

Introduction
Different from the abstract in that it sets the stage for the content of the article, rather than telling the reader what it is about.

Main body
May incorporate subtitles, artwork, photos, etc.

Conclusion/Summary
Assessment of results or restatement of points in introduction.

Endnotes/References/Bibliography
Use only when essential. Use author/date citation method in the main body. Numbered footnotes or endnotes will be converted. Include complete publication information. Standard is *The Associated Press Stylebook*, 52nd ed. and *Wesbter's New World College Dictionary*, 5th ed.

Acknowledgments
Use to thank those who helped make the article possible.

Illustration/Tables/Photos and explanatory text

If the files are large, these can be submitted separately, due to email size limits. Initial submission may include copies of originals; however, publication will require the originals. When possible, submit original images. Color is preferable.

File Format

Illustration files with .EPS extensions work best. Other acceptable extensions are .TIFF/.JPEG/.PICT.

Permission(s) to reprint, if appropriate

Previously published articles are acceptable but can be published only with written permission from the copyright holder.

Author(s)/Contibutor(s)

Please include a brief biographical statement.

Submission/Acceptance Procedures

Papers are submitted on a competitive basis and are evaluated by an editorial review board comprised of various department managers and subject matter experts. Following initial selection, authors whose papers have been accepted for publication will be notified by email.

Papers submitted for a particular issue but not accepted for that issue may be carried forward as submissions for subsequent issues, unless the author specifically requests in writing that there be no further consideration.

Submit articles to:

Editor
The Saudi Aramco Journal of Technology
C-3D, Room AN-1080
North Admin Building #175
Dhahran 31311, Saudi Arabia
Tel: +966-013-876-0498
Email: *william.bradshaw.1@aramco.com.sa*

Submission deadlines

Issue	Paper submission deadline	Release date
Summer 2022	February 1, 2022	June 30, 2022
Fall 2022	May 10, 2022	September 30, 2022
Winter 2022	August 4, 2022	December 30, 2022
Spring 2023	November 7, 2023	March 31, 2023

There is more.

Study of Preformed Particle Gel Blocking Performance in Fractured Carbonate Reservoirs

Dongqing Cao, Dr. Ayman M. Almohsin, Dr. Ming Han and Dr. Bader G. Alharbi

Abstract / The blocking capacity of a preformed particle gel (PPG) in fractures is critical for a water shutoff application in fractured reservoirs. This work studies the PPG blocking behavior by a series of coreflooding tests in fractured carbonate cores. The effects of PPG strengths, PPG pack density, and particle/fracture size ratio were systematically investigated.

Enhanced Regained Permeability and Fluid Flow Back from Tight Sandstone and Carbonate Oil Reservoirs with Unique Flow Back Chemistry

Dr. Rajesh K. Saini, Brady Crane, Nicole R. Shimek, Dr. Weiran Wang and Brent Cooper

Abstract / Large amounts of aqueous-based fluids used in hydraulic fracturing of tight formations is not fully recovered immediately after the treatment, resulting in increased water saturation, water blockage, clay swelling, reduced relative permeability, and long-lasting formation damage that impedes production. To enhance flow back fluid recovery, nanoemulsion-based flow back aids were developed for oil-bearing sandstone and carbonate formations.

Population Balance Mechanistic Simulation of CO_2 Foam Flooding

Dr. Muhammad M. Almajid, Dr. Zuhair A. Al-Yousef, and Othman S. Swaie

Abstract / Mechanistic modeling of the non-Newtonian carbon dioxide (CO_2) foam flow in porous media is a challenging task that is computationally expensive due to abrupt gas mobility changes. The objective of this article is to present a local equilibrium CO_2 foam mechanistic model, which could alleviate some of the computational cost, and its implementation in the MATLAB reservoir simulation tool (MRST). Interweaving the local equilibrium foam model into MRST enables users' quick prototyping and testing of new ideas and/or mechanistic expressions.

The Measurement of Tortuosity of Porous Media Using Imaging, Electrical Measurements, and Pulsed Field Gradient NMR

Dr. Hyung T. Kwak, Mahmoud Elsayed, Dr. Ammar El-Husseiny and Dr. Mohamed A. Mahmoud

Abstract / Tortuosity, in general, characterizes the geometric complexity of porous media. It is considered as one of the key factors in characterizing the heterogeneous structure of porous media and has significant implications for macroscopic transport flow properties. There are four widely used definitions of tortuosity that are relevant to different fields from hydrology to chemical and petroleum engineering, which are: geometric, hydraulic, electrical, and diffusional.

To read these articles and others, go to www.saudiaramco.com/jot

Aramco
Journal
of Technology

Liked this issue?
Sign up. It’s free.

To begin receiving the *Aramco Journal of Technology* please complete this form, scan and send by email to ***william.bradshaw.1@aramco.com.***

Got questions?

Just give us a call at +966-013-876-0498 and we’ll be happy to help!

Scan the QR code to go straight to your email and attach the form!

Subscription Form

Name
Title
Organization
Address
City
State/Province
Postal code
Country
Email address
Phone number
Number of copies

www.saudiaramco.com/jot